

Sensitivity of a Compressor Repeating-Stage to Geometry Variation

by

Jérôme LAVAINNE

Diplôme d'ingénieur, Ecole Centrale Paris, Paris, FRANCE (2001)

Submitted to the Department of Aeronautics and Astronautics
in partial fulfillment of the requirements for the degree of

Master of Science in Aeronautics and Astronautics

at the

MASSACHUSETTS INSTITUTE OF TECHNOLOGY

September 2003

© Jérôme LAVAINNE, MMIII. All rights reserved.

The author hereby grants to MIT permission to reproduce and distribute publicly paper and electronic copies of this thesis document in whole or in part.

Author
Department of Aeronautics and Astronautics
August 15, 2003

Certified by.....
David L. Darmofal
Associate Professor of Aeronautics and Astronautics
Thesis Supervisor

Accepted by.....
Edward M. Greitzer
H N Slater Professor of Aeronautics and Astronautics
Chair, Committee on Graduate Students

Sensitivity of a Compressor Repeating-Stage to Geometry Variation

by

Jérôme LAVAINNE

Submitted to the Department of Aeronautics and Astronautics
on August 15, 2003, in partial fulfillment of the
requirements for the degree of
Master of Science in Aeronautics and Astronautics

Abstract

Deterministic and probabilistic sensitivity analyses of an embedded compressor stage performance to blade geometric variations are performed. The performance calculations were conducted with a three-dimensional (3-D) Reynolds Average Navier-Stokes solver and also a meanline analysis which included a model for end-wall flow blockage and losses.

The 3-D simulations showed that the end-wall boundary layers at the casing increased in size across the rotor and decreased across the stator. A quantitative method to include this phenomenon is developed for the meanline analysis. The deterministic sensitivity analysis using the 3-D simulation showed a high sensitivity of stage performance to rotor tip clearance. The probabilistic study, based on a response surface developed from the 3-D simulations, showed the mean stage efficiency was a half point below the nominal efficiency. Further, the major part (75%) of the observed performance variability was attributable to rotor tip clearance variability. The deterministic sensitivity analysis using the meanline simulation showed a weaker dependence on rotor tip clearance, with rotor leading edge angle being most important and rotor tip clearance second in terms of performance sensitivities. For the probabilistic analysis (also performed using a response surface), a performance mean shift similar to the 3-D simulations was observed with the key drivers being the rotor leading edge angle and rotor tip clearance. The difference in sensitivity between the two models was found to be a direct result of the inability of the meanline analysis to accurately capture the variation in end-wall boundary layer within the stage. It is suggested that capturing this effect in a manner that allows probabilistic simulations is a fruitful topic for future work in the robust design methodology for compressors.

Thesis Supervisor: David L. Darmofal

Title: Associate Professor of Aeronautics and Astronautics

Acknowledgments

First, I would like to thank my advisor Professor David L. Darmofal as well as Professor Edward M. Greitzer for their constant help and guidance throughout the course of this work. I am indebted to them for proposing me this research assistantship. I am also grateful to Victor Garzon for his help and his tutoring, especially when I started my research. Special thanks also go to David Smith who spent a lot of time, too much time I would say, fixing my computer and making Fine NUMECA work in parallel. Jonathan Marlier, from NUMECA USA deserves a special thanks as well for being available and very responsive when I was struggling with Fine. I am also very grateful to SNECMA engineers Anthony Laude, David Monteiro-Fernandes and Armel Touyeras for their help, especially during my multiple stays at SNECMA. The suggestions of Dr. M. V. Casey concerning the repeating stage computations are also appreciated. Finally, the last person that directly contributed to this thesis and that I warmly thank is my friend Garrett Barter for spending a week-end correcting my poor grammar in order to have a first draft that would survive the red pen...

I must say that my experience at MIT and in Boston was very instructive and not always that happy, starting with the tragedy of September 11th, 2001 that affected all of us. I did not feel at ease in this climate of terror and in the bellicose climate that followed until recently. I was also very sad not to be able to attend my only brother Frédéric's wedding on September 15th, 2001... Life at MIT has not been really what I had expected when I first arrived and I did not think that I would stay that long. But anyway, I learned to face these difficulties and finally overcame them since I am writing this acknowledgement... But I would not have been able to be successful and I would not have spent very good moments if I had not been surrounded by many friends and lab mates... First the ACDL lab, especially during the second year, have been full of people that made the many hours spent in front of my computer screen, in my small cubicle, more bearable. Thanks to James, Marc, Mike, Ricardo, Sean, Todd, Victor especially for keeping the ratio of English speakers over French speakers over one... Special thanks go to Vivian, Curran, Garrett for the chats and parties we had together. I also have benefited greatly from belonging to the "French Speakers Connection" that helped me feel a bit at home when I was homesick. An enormous thanks goes to Guillaume for the chats we had last year, Yann for his support, Hector for his nice Spanish accent, David for his nice Canadian accent as well... and his nice sets when playing beach-volleyball, Matthieu for

his support, always helping me to relax when I was stressed. Special thanks go also to my tennis partners Kuangshin, Lars, and Sébastien who helped me enjoy the MIT tennis courts... Thanks also to Radiohead for supporting me with his excellent music when I was working all day long, I have so many songs in my head now.

A very sincere and warm thanks goes to Mariu, without whom I would not have enjoyed that much the last six month of my stay. I only wish that we had met earlier. I am so grateful for all the patience you had listening to me, supporting me, sometimes waiting for me until 11pm for dinner after a very long day of work... I thank you for all the moments we spent together and that made me see Boston under a better light. I look forward to spending many other similar moments in the future with you...

Finally, I cannot finish before giving enormous thanks to my family that was always there when I needed them. To my parents for being always connected on the net and giving me hellos every day, to my brother Frédéric for being so supportive and understanding, to my sister-in-law Gwenaëlle for giving me a nephew (or a niece) in a month, to my uncle and taunt for chatting with me from time to time, I would like to say : *Merci infiniment pour votre soutien; sans vous tous, je n'aurai jamais réussi.*

The work reported in this thesis was initiated by Dr. Christian Mari of SNECMA Moteurs, whose interest in the project is very much appreciated. We are also pleased to recognize the efforts of M. Rene Carillo in fostering the collaboration between SNECMA and MIT.

The research was supported by a grant from SNECMA Moteurs, and this support is gratefully acknowledged.

Contents

- 1 Introduction 21**
 - 1.1 Background and Motivations 21
 - 1.2 Specific Thesis Objectives 22
 - 1.3 Overall Modeling Approach 23
 - 1.4 Thesis Contributions 24
 - 1.5 Thesis Organization 25

- 2 Sensitivity Analysis using 3-D Simulation 27**
 - 2.1 Introduction 27
 - 2.2 The 3-D Simulations on CREATE 28
 - 2.2.1 The CREATE Compressor 28
 - 2.2.2 Brief Description of the 3-D Solver (FINE/TURBO) 28
 - 2.3 Description of the Deterministic Sensitivity Analysis 31
 - 2.4 Maximum Pressure Rise Correlation from GE 33
 - 2.5 Results of the Deterministic Sensitivity Analysis 35
 - 2.6 Probabilistic Sensitivity Analysis 39
 - 2.6.1 Introduction to Probabilistic Sensitivity Analysis 39
 - 2.6.2 Response Surface Method 40
 - 2.6.3 Input Distributions 40
 - 2.6.4 Monte-Carlo Analysis Results with all Geometry Noises 41
 - 2.6.5 Effect of Individual Geometric Noises on Mean Performance and Variability . 44

3	Flow Models for End-wall Effects	49
3.1	Introduction	49
3.2	GE End-wall Correlations	50
3.3	Effect of End-wall Flow Blockage on the Freestream Flow : The AVDR	51
3.3.1	Blockage Results from the 3-D Calculations	51
3.3.2	Comparison of blockage behavior at hub and tip	54
3.3.3	Effect of End-wall Flow Blockage on Freestream Flow Quantities	54
3.4	The End-wall Blockage Model of Horlock [8]	60
3.5	An Empirically Based Meanline Model for the Third Stage	61
3.5.1	Constant δ_{hub}^* and δ_{tip}^* at the Inlet	61
3.5.2	No Variation in δ_{hub}^*	62
3.5.3	Calculation of $\Delta(\delta_{tip}^*)$ across the rotor from Horlock's model [8]	62
3.5.4	Repeating stage value of δ_{tip}^* after the stator	64
3.5.5	Calculation of the stage performance	67
4	Meanline Sensitivity Analysis	69
4.1	Introduction	69
4.2	Results of the Deterministic Sensitivity Analysis using the Meanline Model	69
4.3	Results of Probabilistic Sensitivity Analysis	72
4.3.1	All Geometric Parameters have Variability	72
4.3.2	Effect of Individual Geometric Noises on Mean Performance and Variability	72
4.4	Comparison of 3-D and Meanline Models	83
4.4.1	Deterministic Comparison of the 3-D and Meanline Models	83
4.4.2	Probabilistic Comparison of the 3-D and Meanline Models	84
5	Summary and Conclusions	89
5.1	Thesis Summary	89
5.2	Recommendations for Future Work	90
A	Meanline Analysis without endwalls on CREATE Compressor Using MISES	93
A.1	Introduction	93
A.2	Creating the Geometry for MISES	94

A.2.1	The Meanline Analysis	94
A.2.2	The m' θ Coordinates	94
A.2.3	The XinXout.CREATE and interstream.CREATE files	96
A.3	Inlet and first row initialization	97
A.3.1	Velocity	98
A.3.2	Wheel Rotation Speed	99
A.3.3	Temperature	99
A.3.4	Pressure	99
A.3.5	Reynolds Number	100
A.3.6	The output file out.xxx	100
A.4	Row to Row Information Transmission	101
A.4.1	The interblade.f File	101
A.4.2	From Rotor to Stator	101
A.4.3	From Stator to Rotor	103
A.5	Detailed First Row Process for Running MISES on Compressor	105
A.6	Running the run_comp Interface	109
B	The GE Correlations	111
B.1	The C_h at stall	111
B.2	The Displacement Thickness Correlation	111
C	Implementation of the Correlations with Mises	117
D	How To Run NUMECA Fine Turbo on CREATE Compressor	121
D.1	Introduction	121
D.2	The meshing of the grid using IGG/Autogrid	121
D.2.1	The first cell distance to wall y_{wall}	121
D.2.2	The tip clearance grid	123

List of Figures

2-1	The CREATE Compressor. The dot line is the meanline.	28
2-2	Compressor map and row loss for different grid levels. The three levels of grid are compared with SNECMA throughflow results for the CREATE compressor.	30
2-3	Example of $2\text{-}\sigma$ deformations applied to the third stator	32
2-4	The π/\dot{m} graphic method in the compressor map	33
2-5	The diffuser/stage geometry parameters	34
2-6	Illustration of change in operating line pressure ratio due to increase in blade thickness	38
2-7	Illustration of increased stalling pressure rise margin due to erroneous estimation of C_{hmax} sensitivity	38
2-8	Illustration of the three probabilistic metrics used.	39
2-9	Input clearance distribution using the created CDF	41
2-10	Output distributions from the Monte-Carlo analysis using the response surface based on 3-D simulations.	42
2-11	Output CDF's from the Monte-Carlo analysis using the response surface based on 3-D simulation.	43
2-12	Rank of the five geometric parameter that most impact the performances. The X-axis gives the parameter whose uncertainty is set to zero. R is for rotor, S for stator, C for clearance, LE for leading edge, TE for trailing edge, M for maximum, A for angle, T for thickness, and CH for chord.	48
3-1	Two-step procedure to obtain the stage characteristic, from [15]	52

3-2	Evolution of the blockage at hub and tip for (a) CREATE compressor at operating point, nominal geometry (b) CREATE compressor at $\pi/\pi_{nominal} = 1.044$, nominal geometry (c) STAGE3 at at peak efficiency, nominal geometry (d) STAGE3 at $\pi/\pi_{nominal} = 0.96$, tip and hub clearances multiplied by two	53
3-3	Isoline of rotor $C_{p_o} = \frac{P_o - P_{o_{in}}}{P_{o_{in}} - P_{in}}$ at 10% chord (a), 30% (b), 60% (c), 80% (d) and just after the trailing edge (e). PS is for pressure side and SS for suction side	55
3-4	Isoline of stator $C_{p_o} = \frac{P_o - P_{o_{in}}}{P_{o_{in}} - P_{in}}$ at 10% chord (a), 30% (b), 60% (c), 80% (d) and just after the trailing edge (e). PS is for pressure side and SS for suction side	56
3-5	Σ -contour on a stream-surface across a blade passage	57
3-6	Variation of δ^* at the inlet of the third stage for (a) all the 3-D calculations conducted and (b) only the calculations used for the sensitivity analysis. Points at the bottom of the figure are δ_{hub}^* and points at the top are δ_{tip}^*	63
3-7	Variation of δ^* across the third stage for all the 3-D calculations conducted. The first location on the X-axis from the left is the inlet of the stage. In the middle is the mixing plane between rotor and stator and on the right is the exit of the stator.	64
3-8	$\Delta(\delta_{tip}^*)_{rotor}$ as a function of $\left(\frac{\Delta P}{\frac{1}{2}\rho V_x^2}\right)_{rotor} \epsilon_{tip}$ for (a) all the 3-D calculations conducted and (b) only the calculations used for the sensitivity analysis. The quantities are normalized by the inlet passage height h_{inlet} . The dashed line represents Horlock's model.	65
3-9	Ratio of $\delta_{tip_{3D}}^*$ and $\delta_{tip_{GE}}^*$ at exit as a function of mass Flow. The red line represents the nominal geometry speedline, the green line the double clearance speedline. . . .	66
4-1	Output distributions from the Monte-Carlo analysis using the response surface based on the meanline simulation	73
4-2	Output CDF's from the Monte-Carlo analysis using the response surface based on the meanline simulation	74
4-3	Ranking of the five geometric parameters that most impact the pressure ratio and efficiency distributions. The X-axis gives the parameter which variability is set to zero. R is for rotor, S for stator, C for clearance, LE for leading edge, TE for trailing edge, M for maximum, A for angle, T for thickness and CH for chord.	78

4-4	Ranking of the five geometric parameter that most impact the stalling pressure rise margin distribution. The X-axis gives the parameter which variability is set to zero. R is for rotor, S for stator, C for clearance, LE for leading edge, TE for trailing edge, M for maximum, A for angle, T for thickness and CH for chord	79
4-5	The margin standard deviation reduction.	82
4-6	Prediction of efficiency for 3-D and meanline models. The value are normalized by the 3-D efficiency at nominal geometry on the operating point	83
4-7	Output distribution from the Monte-Carlo analysis on the response surface from the meanline sensitivity analysis	85
4-8	Ranking of the five geometric parameter that most impact the standard deviation error. The X-axis gives the parameter which uncertainty is set to zero. R is for rotor, S for stator, LE for leading edge, TE for trailing edge, M for maximum, A for angle, T for thickness, CH for chord	88
A-1	The Meanline Analysis	95
A-2	The Streamline coordinates $m' \theta$	96
A-3	Flowchart : First Stage Process	106
A-4	Flowchart : Detailed First Row Geometry File Generation Process	107
A-5	Flowchart : Detailed First Row Process	108
A-6	Directory and Files Tree Pattern	110
B-1	Correlation of stalling effective static-pressure-rise coefficients	111
B-2	Effect of tip clearance on stalling pressure rise coefficient	112
B-3	Effect of Reynolds number on stalling pressure rise coefficient	113
B-4	Effect of axial spacing on stalling pressure rise coefficient	113
B-5	Sum of hub anf tip endwall axial velocity displacement thickness, from [10]	114
B-6	Sum of hub anf tip endwall tangential-force thickness, from [10]	115
B-7	Effect of axial spacing on endwall displacement thickness, from [10]	115
C-1	Flowchart : Detailed Process of a Single Meanline Run using Correlations and Mises	119

List of Tables

2.1 Results of the sensitivity analysis of the 3rd stage with the 3-D simulation. Figures in parenthesis are rankings of the ten most important noises. The first column is the varying blade geometry parameter. The second column indicates the row on which the geometry variations have been applied : R3 for rotor and S3 for stator. The third column gives the quantitative value of the deformation. The last three columns are the results of the sensitivity analysis relative to the nominal geometry for total pressure ratio ($\Delta PR = \frac{\Delta P_o}{P_{o_{in}}}$), isentropic efficiency (η) and stalling pressure rise margin (Mg). 36

2.2 Mean shift of the Monte-Carlo analysis results on the response surface of the 3-D simulations. Figures in parenthesis ranks the five most important noises. 45

2.3 Standard deviation of the Monte-Carlo analysis results on the response surface of the 3-D simulations. Figures in parenthesis ranks the five most important noises. 46

2.4 Fifth percentile of the Monte-Carlo analysis results on the response surface of the 3-D simulations. Figures in parenthesis ranks the five most important noises. 47

3.1 The Three AVDR Variation Cases 58

3.2 AVDR Variation Effects on Freestream Quantities 59

4.1	Results of the sensitivity analysis of the 3 rd stage with the meanline simulation. Figures in parenthesis are rankings of the ten most important noises. The first column is the varying blade geometry parameter. The second column indicates the row on which the geometry variations have been applied: R3 for rotor and S3 for stator. The third column gives the quantitative value of the deformation. The last three columns are the results of the sensitivity analysis relative to the nominal geometry for total pressure ratio ($\Delta PR = \frac{\Delta P}{P_{oin}}$), isentropic efficiency (η) and stalling pressure rise margin (Mg).	71
4.2	Mean shift of the Monte-Carlo analysis on the response surface of the meanline simulation. Figures in parenthesis rank the five most important geometric noises.	75
4.3	Standard deviation of the Monte-Carlo analysis on the response surface of the meanline simulation. The Figures in parenthesis rank the five most important geometric noises.	76
4.4	Fifth percentile value of the Monte-Carlo analysis on the response surface of the meanline simulation. Figures in parenthesis are ranking the five most important geometric noises.	77
4.5	Mean shift of the Monte-Carlo analysis on the response surface of the meanline model error.	86
4.6	Standard deviation of the Monte-Carlo analysis on the response surface of the meanline model error.	87

Nomenclature

Roman

a	Speed of sound
A	Area of the passage
$\bar{A}00$	Mises dimensional reference speed for the compressor = $\bar{a}_{o_{inlet}}$
A_{geom}	Area of the geometrical passage
b	Mises Streamtube thickness
C_f	Friction coefficient
C_h	Enthalpy-equivalent static pressure rise
$C_{h_{max}}$	Maximum enthalpy-equivalent static pressure rise reachable by a stage (at stall)
c_p	Specific heats
C_p	Total pressure coefficient $C_p = \frac{P_o - P_{o_{in}}}{P_{o_{in}} - P_{in}}$
F_x	Axial force on the blade per unit length
f_x	Local axial force on the blade in the deficit region per unit length
g	Cascade staggered spacing
g_2	Trailing edge cascade staggered spacing
H	Boundary layer shape factor
h	Enthalpy
K	Empirical constant for calculation of a ν as a function of ϵ

L	Arc length of the airfoil
L_{ref}	Mises reference length = radius of shroud = 259.1mm
\dot{m}	Mass flow
M	Mach number
m', θ	Mises local streamwise and circumferential coordinates
Mg	Stalling pressure rise margin
P	Pressure, when no subscripts static
\mathcal{P}	Power
R	Reaction of the stage
r	Radius
RA	Ratio of consecutive rows reference speeds for row to row dimensional quantity transmission at mixing plane
Re	Reynolds number
S	Empirical constant for Sutherland law
s	Blade spacing
T	Temperature, when no subscripts static
\mathcal{T}	Torque
U	Blade Speed
u_τ	Friction velocity
V	Magnitude of velocity
V_x	Axial velocity
$X - Z$	Mises coordinates, X for radius, Z for axial

XYZ	3D coordinates, X for pitch, Y for radius, Z for axial
y_{wall}	First cell distance to the wall (3D grid generation)
Y_1^+	Reynolds number based on wall variables at the first node (3D grid generation)
Δz	Axial gap between row

Greek

β	Flow angle
δ	Boundary layer thickness
δ^*	Boundary layer displacement thickness
ϵ	Tip clearance
η	Isentropic efficiency
γ	Ratio of specific heats c_p/c_v
μ	Dynamic viscosity
ν	Tangential force thickness
Ω	Wheel speed (rad/s)
ω	Non dimensionalized loss parameter
π	Absolute pressure ratio
ρ	Density
σ	Standard deviation
θ	Momentum thickness

Subscripts

$()_1$	At inlet
$()_2$	At outlet

$()_R$	Rotor
$()_S$	Stator
$()_x$	Axial quantity
$()_o$	Stagnation quantity
$()_a$	Mises absolute quantity : fluid is brought to rest $r=0$ with isentropic process
$()_{abs}$	Mises absolute-frame quantity
$()_{hub}$	At hub
$()_{tip}$	At tip

Superscripts

$()'$	Relative frame quantity
$(-)$	Dimensional quantity in Mises
(\sim)	Freestream quantity

Acronym

2-D	Two-Dimensional
3-D	Three-Dimensional
AVDR	Axial Velocity Density Ratio
CDF	Cumulative Density Function
CFD	Computational Fluid Dynamics
GE	General Electric
MISES	Multiple blade Interacting Streamtube Euler Solver
PDF	Probability Density Function

Chapter 1

Introduction

1.1 Background and Motivations

Variability in gas turbine engine performance due to manufacture and in service wear is a key factor in the competitiveness of engine manufacturers. Aircraft engines are subject to a number of competing requirements and current designs often result in engines with small failure margins. Therefore, manufacturing variations can lead to significant performance variations or even catastrophic failures. A need exists for (1) air breathing engines which perform with greater reliability and efficiency despite variability in component geometry, and (2) next generation design tools to develop these robust engines. We therefore wish to develop advanced tools for assessing and managing aerothermal performance degradation due to manufacturing variation.

The assessment of variability in the analysis and design of gas turbine engine components has been a concern to manufacturers and government agencies alike for more than two decades [12]. The quantification of variability is most rigorously addressed using probabilistic framework. However, the application of probabilistic techniques has been limited primarily to structural considerations such as component life prediction and stochastic effects in material properties [1, 17, 14]. There has been much less research aimed at assessing the impact of geometry variations on component performance in a probabilistic manner. For the design of compressors, Greitzer and Wisler [6] propose that as performance gains are reaching diminishing returns, design practices must begin to address the 'ilities' such as manufacturability, operability, reliability, etc. This thesis is a step in this direction and is focused on a probabilistic description of the response of a multistage axial

compressor to geometric variation.

The thesis builds on the work of Garzon [5], who created a probabilistic aerothermal design tool for compressor airfoils using Monte Carlo analysis and gradient-based optimization methods. Garzon was able to design single blade rows subject to geometric noise, and make trade-offs between best mean performance and performance variability. He showed that with realistic geometric noise, the mean efficiency of a compressor was 1% lower than the nominal. However, his work was purely two-dimensional and did not account for three-dimensional (3-D) effects, such as end-wall flow losses and blockage. In particular, tip clearance variations, which are known to be a major cause of changes in efficiency and in stall margin, were not studied. The present work is a step toward creating an effective methodology to design compressors for robust aerothermal performance including end-wall flow losses and blockage.

Probabilistic computations typically involve thousands of simulations. A major barrier to the development of a probabilistic aerothermal analysis for compressors is thus the large computational cost associated with 3-D computational fluid dynamics (CFD) models. A possible solution to this problem is the use of a fast, reduced-order aerothermal model for compressors including end-wall effects. Such a model could be used early in the compressor design, when robustness should be considered.

In this thesis, compressor performance sensitivities to blade geometric variation are determined using both 3-D CFD and reduced-order models. A comparison between the two models is made to determine the suitability of the reduced-order model. Surrogates of the two models are created using response surfaces to determine the probabilistic impact of manufacturing noise on compressor performance. The compressor used as the subject for the project is a Snecma Moteurs three-stage compressor CREATE, which is representative of the middle or rear stages of an HP compressor.

1.2 Specific Thesis Objectives

The specific goals of this thesis are :

- Quantify in a deterministic manner the sensitivity of stage performance, specifically overall total pressure ratio, efficiency, and stalling pressure rise margin, to blade geometry variation using a 3-D CFD model.

- Quantify in a deterministic manner the sensitivity of stage performance to blade geometry variation using a reduced-order model that accounts for end-wall effects.
- Determine the geometric noises that most impact the mean, variability and tails of the stage performance distributions.
- Compare the reduced-order and 3-D models and determine the main blade geometric noises that lead to differences in the model predictions.

1.3 Overall Modeling Approach

The reduced-order model we have developed for compressor stage analysis is based on coupling a meanline analysis with end-wall correlations. This basic approach is common practice during preliminary stages of compressor design [10, 11, 15]. For the meanline analysis, we have used the quasi-3-D solver MISES developed by Drela [4]. In contrast to the previous meanline-based approach which used correlations to establish airfoil performance, MISES is a coupled Euler-boundary layer method capable of modeling subsonic-to-supersonic flows including transition and small-scale separation.

We adopted the end-wall correlation developed at GE by Smith [15], and Smith and Koch [10], based on the repeating-stage approximation. This method uses experimental data from multistage compressors. The flow is separated into freestream and end-wall regions. The end-wall boundary layer displacement thicknesses are related to the compressor mass flow and overall efficiency; the latter involves an assumed blade force deficit in the end-wall region represented by a tangential-force thickness. A further assumption is that at stall the end-wall boundary layers grow to a limiting value which depends on tip clearance. The stall point, in turn is found through another set of correlations for peak pressure rise [11] as function of its geometry and Reynolds number. Using the correlations in [15] and [10], it is possible to quantify the end-wall displacement thickness and efficiency of the compressor. More details are given in Sections 2.4 and 3.2.

A limitation of the GE correlation due to the behavior of the end-wall flow blockage within the stage was identified during the analysis of the 3-D CFD simulations. Specifically, the 3-D calculations showed a considerable increase in blockage across the rotor and a decrease across the stator. The resulting contraction (or expansion) of the passage due to growth (decrease) of the

end-wall flow blockage has a significant impact on the flow angle, velocity, static pressure rise in the freestream region. A paper by J.H. Horlock [8] provides insight into this end-wall flow blockage behavior. Using experimental data from Smith [15], Cumpsty [3] and Howard [9], Horlock demonstrates that the repetition occurs not only after the stators of the repeating stages but also after the rotors (though the profiles at the exit of stators and rotors are different from each other). Using the same argument as Smith about the variation in blade force through a repeating stage, Horlock shows that the rise in displacement thickness at the wall is proportional to the pressure rise of the row and the clearance of the blade of the row. In our reduced-order model, we combine the repeating-stage correlations of GE with Horlock’s model of row end-wall behavior.

1.4 Thesis Contributions

The following is a summary of the main contributions of the thesis.

- Creation of a meanline simulation for repeating stages that accounts for end-wall flow losses and blockage. The difference of blockage behavior across the rotor and the stator was included quantitatively in the meanline model. This end-wall flow blockage variation is shown to be critical in estimating stage performance.
- Deterministic assessment of stage performance sensitivity to blade geometric deformation using both 3-D simulations and the meanline model. The performance metrics used for this assessment were pressure ratio, efficiency and stalling pressure rise margin. A large sensitivity of stage performance to rotor tip clearance was found. After the effect of rotor tip clearance, rotor leading edge parameters were found to be important.
- Development of a simple and useful method to probabilistically assess the impact of blade geometric noise on stage performance using deterministic sensitivities. A quadratic response surface of the stage performance was built and a probabilistic analysis was conducted. The mean stage efficiency was found to be a half point lower than the nominal (deterministic) efficiency. Furthermore, 5% of the compressors are estimated to have efficiency at least four points below nominal. The main driver of performance uncertainty was found to be rotor tip clearance in both models.

- Development of a probabilistic method to compare the 3-D and meanline models. The main source of uncertainty between the two models was found to be rotor tip clearance variability.

1.5 Thesis Organization

Chapter 2 presents and discusses the results of the 3-D deterministic and probabilistic sensitivity analyses. Chapter 3 presents the meanline-based model including end-wall effects. Finally, Chapter 4 presents the results of the deterministic and probabilistic sensitivity analyses using the meanline simulation. This chapter also studies the difference between the meanline and the 3-D results.

Chapter 2

Sensitivity Analysis using 3-D Simulation

2.1 Introduction

This chapter presents an analysis of the sensitivity of the third stage performance of the CRE-ATE compressor to geometry variations. The method used to conduct the analysis is described, including the boundary conditions and the geometric blade deformations. A deterministic sensitivity analysis is first conducted. This shows that stage performance is much more affected by the rotor tip clearance variation than by any of the blade geometry variations included. It is also observed that the rotor geometry variations impact stage performance more than the stator geometry variations. The probabilistic impact on stage performance of the different geometry variations is also analyzed. A response surface is constructed from the 3-D simulations, and used in a Monte Carlo analysis. The results imply that the stage performance standard deviation can be as much as two points in efficiency and that this uncertainty is mainly driven by the rotor tip clearance variability.

2.2 The 3-D Simulations on CREATE

2.2.1 The CREATE Compressor

The compressor used for the sensitivity analysis is a SNECMA Moteurs experimental compressor named CREATE whose flow path is sketched in Figure 2-1. The three stages are representative of the middle or rear stages of a high pressure compressor. The inlet conditions to the first stage and the exit static pressure at the design point were supplied by SNECMA.

Calculations on the entire three-stage compressor were first conducted to assess the suitability of the 3-D simulation for this investigation. The 3-D solver was then used on the third stage for the sensitivity analysis.

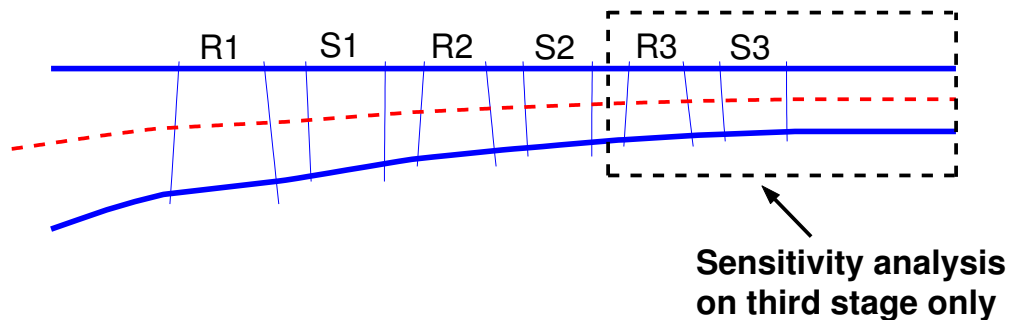


Figure 2-1: The CREATE Compressor. The dot line is the meanline.

2.2.2 Brief Description of the 3-D Solver (FINE/TURBO)

FINE/TURBO is a software environment for CFD written by the company NUMECA. It contains a flow solver **EURANUS** (**EUR**ocean **AER**odynamic **NUM**erical **SIM**ulator), a grid generator **IGG** and a postprocess tool **CFVIEW**. The solver EURANUS is a multipurpose code for 2-D and 3-D internal and external flows using a structured mesh [19]. EURANUS solves the time-dependent Reynolds-Averaged Navier-Stokes (RANS) equations for incompressible and compressible flows. Turbulence can be modelled by an algebraic Baldwin-Lomax model or by two-equation $k - \epsilon$ models.

A multiblock approach was used to generate the compressor grid, generating meshes for each row and stacking the meshes using mixing planes. For each row, the mesh was separated in different

blocks such as inlet, outlet, blade and tip clearance. The finest mesh used contained 3.5 millions of points for the entire compressor. The number of cells from hub to tip was about 60 for all of the rows. Tip and hub clearance meshes were generated with 17 points in the spanwise direction for the nominal clearance (for further details see Section D.2.2).

A study of the effect of the choice the first cell distance to wall y_{wall} and of the impact of the different turbulence models on accuracy, stability, and time cost of the 3-D simulation was conducted. The purpose of this study was to find the adequate mesh and turbulence model combinations to run a sensitivity analysis with sufficient accuracy without too much time expenditure. The Baldwin-Lomax turbulence model was chosen for running the sensitivity analysis. Section D.2 gives the reasons for this choice.

EURANUS can be run on different grid levels to accelerate the convergence (a multigrid approach). A study was conducted to decide which level of grid should be used to run the sensitivity analysis. A particular attention was paid to resolution of the flow in the clearance regions since the impact of clearance variation was to be studied. A compressor map and row losses are presented in Figure 2-2. Investigation of the flow solution for the medium mesh showed that the clearance regions were not accurately resolved. Although the fine mesh results may still be far from the asymptotic solution, the fine mesh speedline is approaching the SNECMA throughflow results. Since further mesh refinement was not possible due to computer memory limitations, the sensitivity analysis was conducted on the current fine mesh.

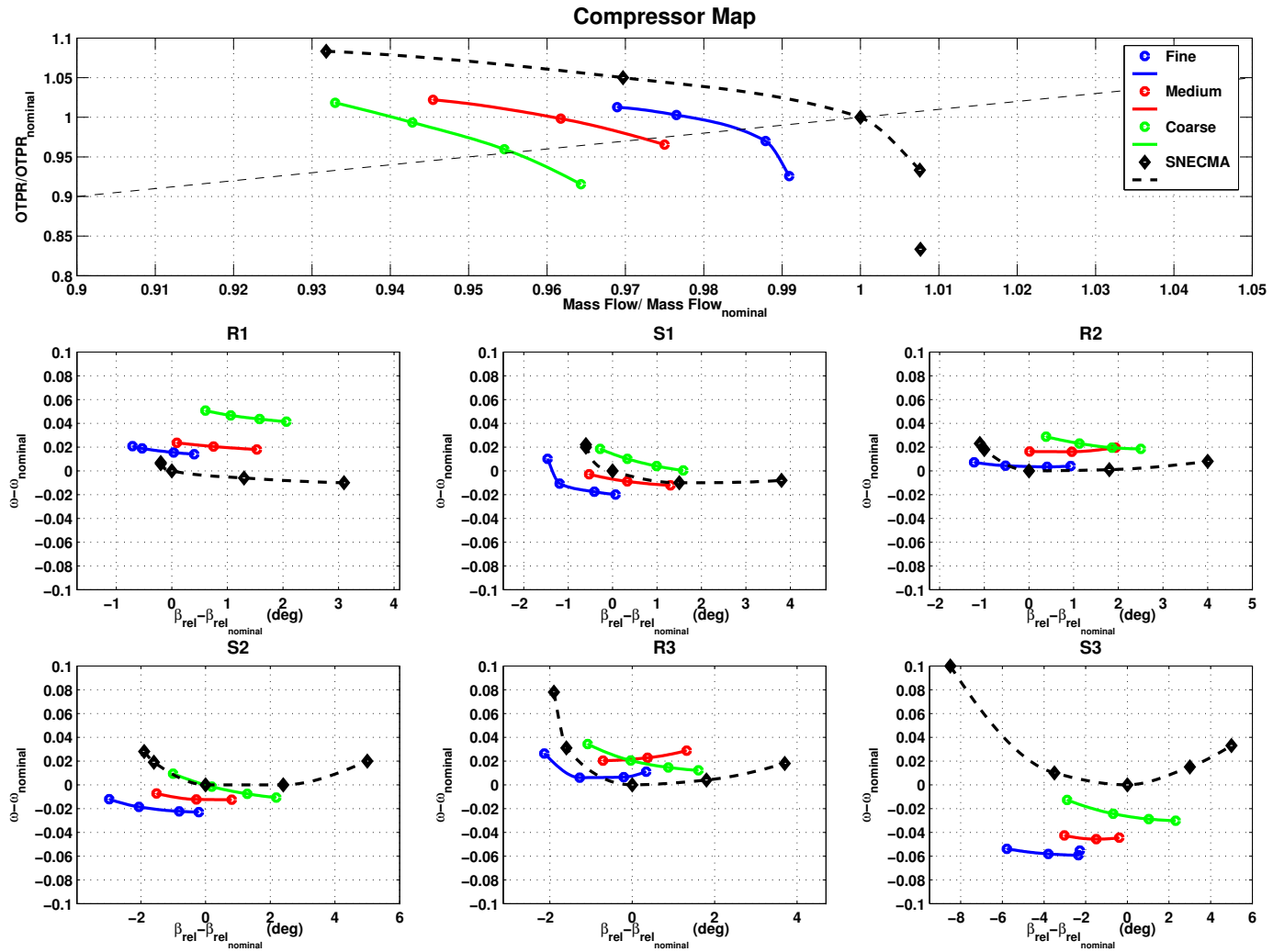


Figure 2-2: Compressor map and row loss for different grid levels. The three levels of grid are compared with SNECMA throughflow results for the CREATE compressor.

2.3 Description of the Deterministic Sensitivity Analysis

The geometric variations for the third stage were based on manufacturing tolerances provided by SNECMA Moteurs. These values are assumed to represent 5% and 95% population values (2σ interval). Variations in the following 14 geometric parameters were considered :

1. Tip clearance : $\text{Nominal} \times 2, \text{Nominal} \div 2$
2. Hub clearance : $\text{Nominal} \times 2, \text{Nominal} \div 2$
3. Rotor chord : $\pm 1.45\%$ of chord
4. Stator chord : $\pm 1.56\%$ of chord
5. Rotor leading edge camber angle : $\pm 2.7^\circ$
6. Stator leading edge camber angle : $\pm 2.7^\circ$
7. Rotor trailing edge camber angle : $\pm 2.7^\circ$
8. Stator trailing edge camber angle : $\pm 2.7^\circ$
9. Rotor leading edge thickness : $\pm 0.73\%$ of chord
10. Stator leading edge thickness : $\pm 0.78\%$ of chord
11. Rotor trailing edge thickness : $\pm 0.73\%$ of chord
12. Stator trailing edge thickness : $\pm 0.78\%$ of chord
13. Rotor maximum thickness : $\pm 0.73\%$ of chord
14. Stator maximum thickness : $\pm 0.78\%$ of chord

Except for the clearances, the geometric noise variability is centered about the design intent. Examples of these deformations at the meanline section of the third stage stator are presented in Figure 2-3.

The design of the sensitivity analysis only considered a single factor at a time. The drawback of this approach is that cross-effects of the geometry deformations are not accounted for. The reason for limiting the study to single factors is the cost of the 3-D simulations, each of which require approximately two days to complete (in order to estimate all interaction effects, 2^{14} simulations would be required).

The inlet conditions of the third stage are taken from a 3-D calculation of the entire three-stage compressor, with nominal geometry, at the operating point defined by SNECMA. From this

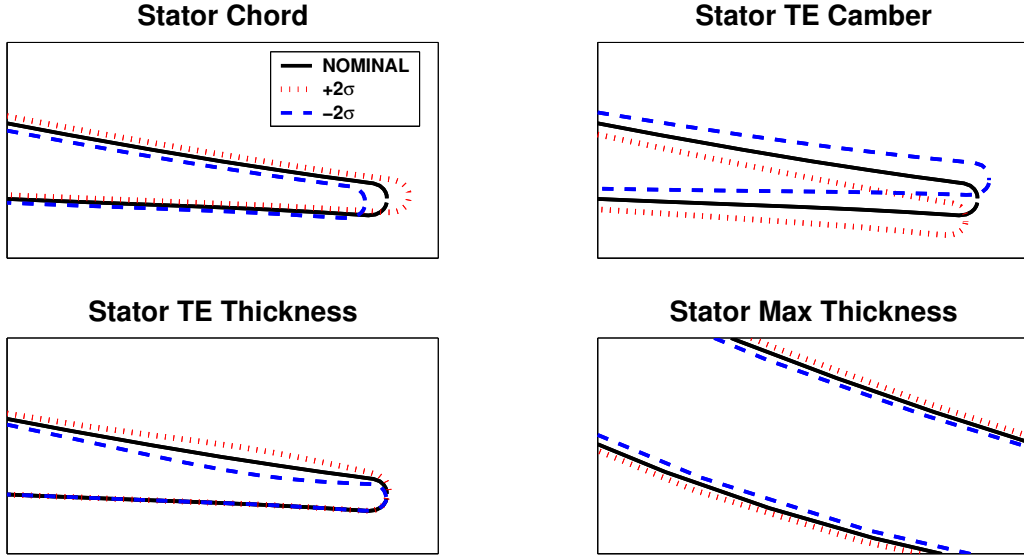


Figure 2-3: Example of 2- σ deformations applied to the third stator

calculation, the distributions of total pressure, P_o , total temperature, T_o , and inlet flow angle, were then applied as inlet conditions to the third-stage for all of the simulations in the sensitivity analysis.

The impact of the geometric variability is quantified for the stage total pressure ratio, efficiency and stalling pressure rise margin along the operating line which was established as follows. The design operating point for the third stage (with nominal geometry) was chosen as the maximum efficiency point along the speedline. For the perturbed geometries, the operating point at design speed is established by requiring that the ratio of $\pi = P_{o2}/P_{o1}$ and mass flow, \dot{m} , is constant. That is

$$\left(\frac{\pi}{\dot{m}}\right)_{perturbed} = \left(\frac{\pi}{\dot{m}}\right)_{nominal}. \quad (2.1)$$

This definition for the operating line is related to holding the exit corrected mass flow $W_{exit} = \frac{\dot{m}\sqrt{T_{o_{exit}}}}{A \cdot P_{o_{exit}}}$ constant neglecting the variation of total temperature at the exit of the stage. 3-D calculations show this assumption is valid for this study since the exit total temperature does not vary by more than 0.7% even for the case where the clearances are doubled on both rotor and stator¹. The operating point on the new speedline with deformed geometry is found at the

¹This case is not used for the calculation of the sensitivities since two deformations are applied in the same time.

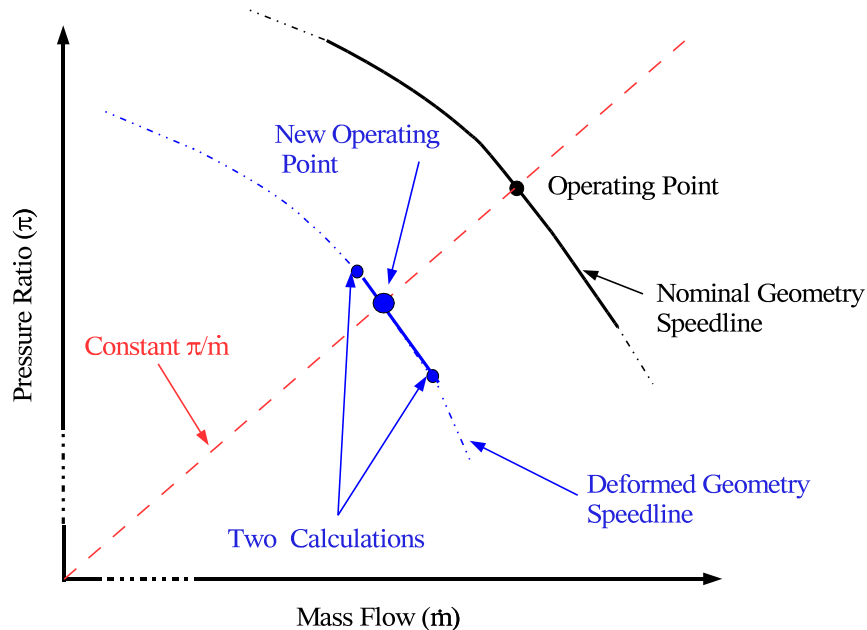


Figure 2-4: The π/\dot{m} graphic method in the compressor map

intersection of the new speedline and the constant π/\dot{m} line, as drawn in Figure 2-4. Two points are required on the speedline for each geometry perturbation so the sensitivity analysis requires 4 simulations for each of the 14 geometry parameters, resulting in 56 runs for the entire analysis beyond those required to establish the nominal speedline.

2.4 Maximum Pressure Rise Correlation from GE

In [11], an empirical correlation is developed to estimate the maximum pressure rise achievable by the compressor stage. The method is derived on the analogy between an axial compressor and a diffuser. The stalling pressure rise is assumed to be only a function of the cascade geometry parameters : tip clearance (ϵ), axial gap (Δz), arc length of the airfoil (L), cascade trailing edge staggered spacing (g_2), cascade staggered spacing (g) and Reynolds number (Re) (see Figure 2-5).

The ratio L/g_2 is viewed as analogous to the ratio (diffuser length)/(exit passage width) for a diffuser and the other quantities are used to match experimental results for axial compressors. These geometric quantities are used on a stage basis, with the rotor and stator values weighted

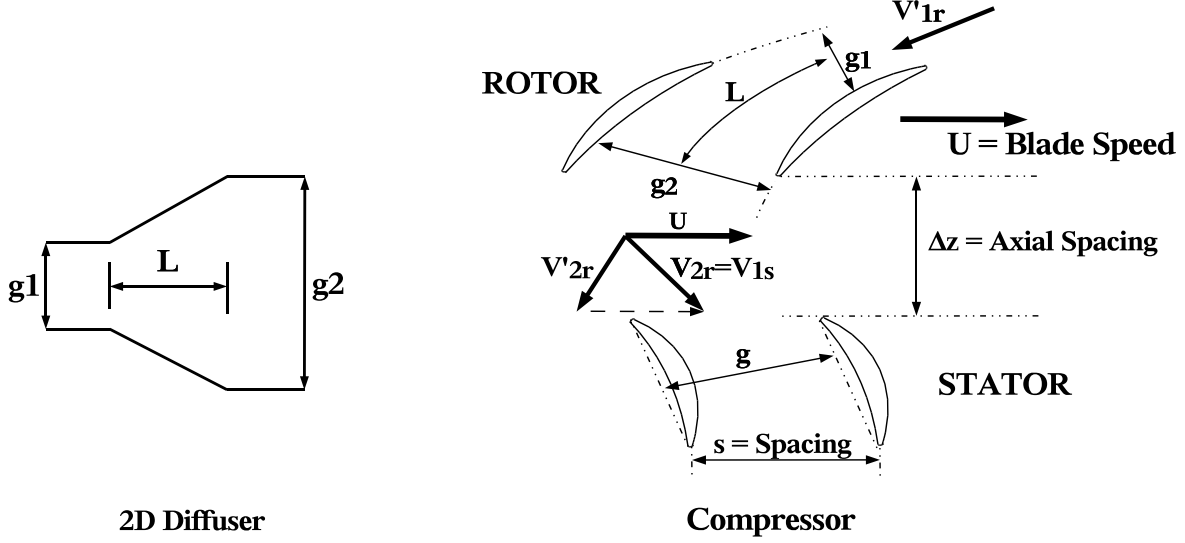


Figure 2-5: The diffuser/stage geometry parameters

by the respective inlet dynamic head to obtain the stage value. The quantity used as a metric for pressure rise is the overall stage enthalpy-equivalent static-pressure-rise coefficient, C_h , based on pitchline free-stream dynamic head :

$$C_h = \frac{c_p \cdot T_1 \left(\left(\frac{P_2}{P_1} \right)^{\frac{\gamma-1}{\gamma}} - 1 \right) - \frac{1}{2} \cdot (U_2^2 - U_1^2)_{rotor}}{\frac{1}{2} \cdot (V_{1rotor}^2 + V_{1stator}^2)} \quad (2.2)$$

The first term in the numerator is the isentropic enthalpy rise and the second term is the enthalpy rise due the change in radius of the streamline along the rotor. In the incompressible limit, the isentropic enthalpy rise can be approximated by

$$\Delta(h)_{isentropic} = c_p \cdot T_1 \left(\left(\frac{P_2}{P_1} \right)^{\frac{\gamma-1}{\gamma}} - 1 \right) \simeq \frac{\Delta P}{\rho_1}. \quad (2.3)$$

If no change in radius for the streamline is considered (2-D approximation) then,

$$C_h \simeq \frac{(\Delta P)_{stage}}{\frac{1}{2} \cdot \rho_1 \cdot (V_{1rotor}^2 + V_{1stator}^2)}. \quad (2.4)$$

Thus, C_h is a compressible generalization of the non-dimensional stage static pressure rise.

Koch relates the maximum pressure rise $C_{h_{max}}$ to geometric parameters. The curves that show this relation are given in Appendix B.1. A final adjustment is to weight C_h by the effective dynamic head,

$$C_{h_{eff}} = C_h \frac{V_{1_{rotor}}'^2 + V_{1_{stator}}^2}{V_{1_{rotor_{eff}}}'^2 + V_{1_{stator_{eff}}}^2}. \quad (2.5)$$

The calculation of the effective velocities is detailed in [11] (see Fig. 13). Given $C_{h_{max}}$, a stalling pressure rise margin is defined using the ratio $\frac{C_{h_{eff}}}{C_{h_{max}}}$ as

$$Mg = 1 - \frac{C_{h_{eff}}}{C_{h_{max}}}. \quad (2.6)$$

2.5 Results of the Deterministic Sensitivity Analysis

The sensitivity analysis results are summarized in Table 2.1. The conclusions that can be drawn from the table are the following.

The three output performance metrics of the stage are more sensitive to the rotor tip clearance variation than any other parameter variation. Doubling the rotor tip clearance reduces the efficiency by 5.9 points and the total pressure ratio by 5.4 points. The sensitivities of the stator hub clearance are much smaller, giving changes of about a point in efficiency and pressure ratio.

The stator geometry variations are substantially smaller than the rotor sensitivities. In part, this can be explained by the higher dynamic pressure on the rotors.

The leading edge and trailing edge angles of the rotor show the next largest changes. Reduction of the leading edge angle by 2.7° reduces the efficiency by almost one point. Reduction of the trailing edge angle by 2.7° reduces the pressure ratio by almost one point. For the rotor leading edge and trailing edge angle deformations, the diffusion losses on the rotor and stator are changed. In the rotor leading edge case, the rotor sees different incidence for the same inlet flow. In the rotor trailing edge case, the inlet flow of the stator is changed and the speedline of the deformed stage is different from the nominal case.

The next most sensitive parameter is the maximum thickness of the rotor, which changes the stage efficiency by roughly one-third point. Adding thickness degrades performance and reducing thickness improves performance. The maximum thickness of the blades affects the minimum area

<i>Geometry</i>	<i>Row</i>		$100\frac{\Delta P_o}{P_{o_{in}}}$	$100\Delta\eta$	$100\Delta Mg$
NOMINAL					
Clearance	R3	Nom \times 2	-5.4 (1)	-5.9 (1)	13.6 (1)
Clearance	S3	Nom \times 2	-0.33 (7)	-0.70 (4)	-2.4 (2)
Clearance	R3	Nom \div 2	1.4 (2)	1.7 (2)	-1.6 (5)
Clearance	S3	Nom \div 2	0.13	0.34 (6)	1.5 (6)
Chord	R3	+1.45%c	-0.002	-0.046	0.24
Chord	S3	+1.56%c	-0.029	-0.060	0.25
Chord	R3	-1.45%c	0.004	0.030	-0.23
Chord	S3	-1.56%c	0.003	0.030	-0.21
LE Angle	R3	+2.7deg	0.29 (9)	0.42 (5)	-0.79 (10)
LE Angle	S3	+2.7deg	-0.046	-0.12	0.12
LE Angle	R3	-2.7deg	-0.64 (5)	-0.94 (3)	1.6 (4)
LE Angle	S3	-2.7deg	-0.003	-0.010	0.019
TE Angle	R3	+2.7deg	0.79 (4)	0.23 (9)	-1.2 (7)
TE Angle	S3	+2.7deg	0.019	0.097	0.28
TE Angle	R3	-2.7deg	-0.95 (3)	-0.087	1.7 (3)
TE Angle	S3	-2.7deg	-0.023	-0.11	-0.19
LE Thick.	R3	+0.73%c	-0.21	-0.26 (8)	0.58
LE Thick.	S3	+0.78%c	-0.027	-0.098	0.077
LE Thick.	R3	-0.73%c	0.002	0.037	-0.011
LE Thick.	S3	-0.78%c	-0.024	-0.057	0.046
TE Thick.	R3	+0.73%c	-0.29 (8)	-0.064	0.95 (8)
TE Thick.	S3	+0.78%c	-0.009	-0.012	0.18
TE Thick.	R3	-0.73%c	0.21 (10)	0.016	-0.72
TE Thick.	S3	-0.78%c	0.006	0.007	-0.14
Max Thick.	R3	+0.73%c	-0.34 (6)	-0.29 (7)	0.80 (9)
Max Thick.	S3	+0.78%c	-0.063	-0.16 (10)	0.23
Max Thick.	R3	-0.73%c	0.18	0.13	-0.41
Max Thick.	S3	-0.78%c	0.043	0.11	-0.18

Table 2.1: Results of the sensitivity analysis of the 3rd stage with the 3-D simulation. Figures in parenthesis are rankings of the ten most important noises. The first column is the varying blade geometry parameter. The second column indicates the row on which the geometry variations have been applied : R3 for rotor and S3 for stator. The third column gives the quantitative value of the deformation. The last three columns are the results of the sensitivity analysis relative to the nominal geometry for total pressure ratio ($\Delta PR = \frac{\Delta P_o}{P_{o_{in}}}$), isentropic efficiency (η) and stalling pressure rise margin (Mg).

of the passage, thereby changing the mass flow and translating the speedline horizontally. The sensitivity of the pressure ratio occurs because when adding thickness, the speedline is moved to the left of the compressor map (decreased mass flow) and therefore the intersection point of the speedline with the π/\dot{m} operating line has lower pressure ratio. If maximum thickness is reduced, the speedline is translated to the right and the pressure ratio of the intersection is higher. Figure 2-6 illustrates this effect.

The smallest parameter sensitivity is the chord length where a variation of less than 0.06 points in efficiency and 0.03 points in total pressure ratio is observed.

Opening the clearance adds stall margin and closing the clearance reduces margin, which contradicts existing data [11]. Figure 2-7 shows the $C_{h_{eff}}$ curves calculated from the 3-D simulation for the nominal geometry and the doubled-clearance cases. For the nominal clearance speedline, the $C_{h_{eff}}$ curve never achieves the $C_{h_{max}}$ level estimated by the correlation. Thus, the stalling pressure rise margin will be overestimated. Furthermore, the results for the doubled-clearance speedline show that the contradictory (compared to past data) sensitivity predictions occur because the change in the effective pressure rise $|\Delta C_{h_{eff}}|$ is clearly larger than the change in the maximum pressure rise $|\Delta C_{h_{max}}|$. As a result the margin increases (decreases) with increasing (decreasing) clearance. However, in the other sensitivity cases for which the clearance is fixed, $C_{h_{max}}$ hardly varies. In these cases, the margin sensitivities may be more accurate as they only depend on the accuracy of the pressure rise trends.

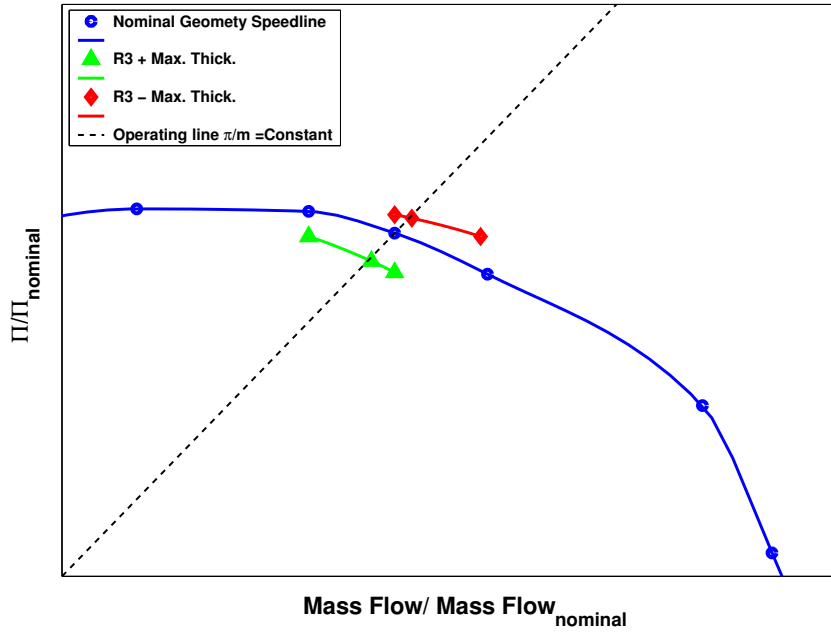


Figure 2-6: Illustration of change in operating line pressure ratio due to increase in blade thickness

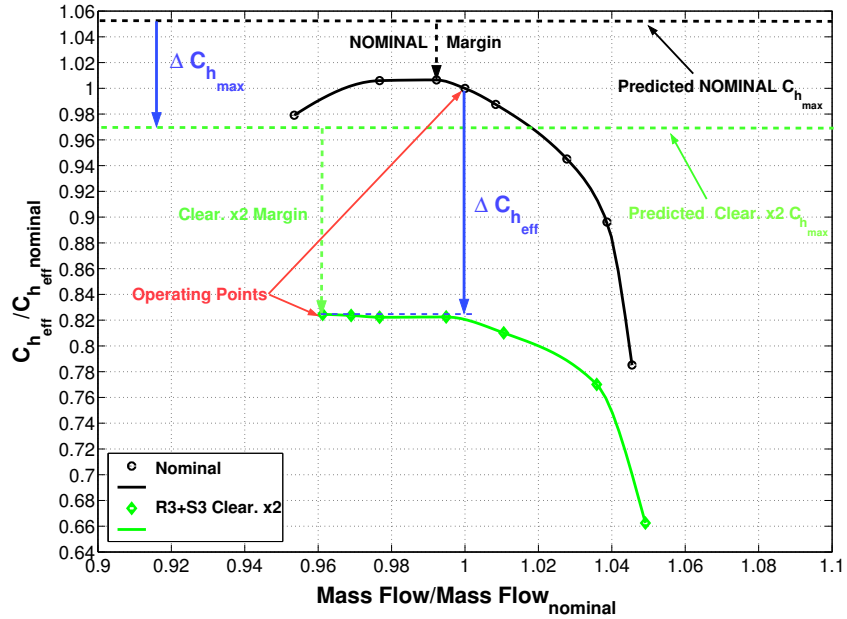


Figure 2-7: Illustration of increased stalling pressure rise margin due to erroneous estimation of $C_{h_{max}}$ sensitivity

2.6 Probabilistic Sensitivity Analysis

2.6.1 Introduction to Probabilistic Sensitivity Analysis

Probabilistic analysis gives additional information to the deterministic analysis, which is described in this section. The three probabilistic metrics used in this analysis are illustrated in Figure 2-8 and are as follows.

The mean shift is defined as the difference between the average and the nominal performance. A mean shift can arise anytime when the output is a nonlinear function of the inputs or if the input distributions are not centered and symmetric about the nominal values.

The standard deviation, denoted by σ , measures the variability of the performance. For a normal distribution, the 4σ interval centered on the mean is the interval that includes 95% of the population.

The fifth percentile is the value for which 95% of the population has higher value. In terms of stage performance, this value is meaningful in quantifying the performance change for outliers of a population (of compressors) and is related to the risk of meeting design requirements.

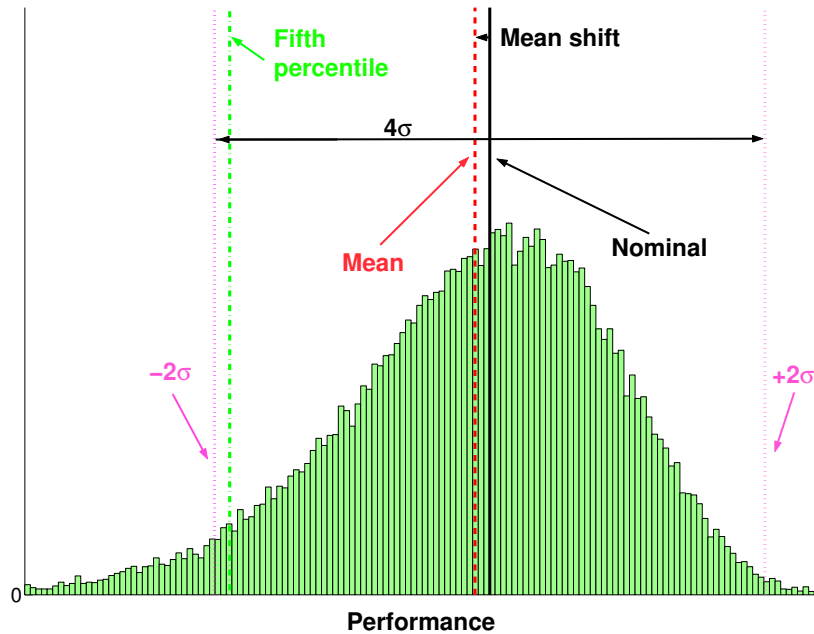


Figure 2-8: Illustration of the three probabilistic metrics used.

2.6.2 Response Surface Method

The response surface method (RSM) is a process of fitting the experimental data by creating a regression surface in a N-dimension space, where N is the number of input variables. A response surface was built for pressure ratio, efficiency and stalling pressure rise margin. The response surface equation was chosen to be quadratic to account for the non-linearity of the 3-D response and has the following form,

$$f^{3D} = \sum_{j=1}^N a_j^{3D} x_j^2 + \sum_{j=1}^N b_j^{3D} x_j + c^{3D} \quad (2.7)$$

There are no cross terms, a_{ij} , because the sensitivity analysis varied each geometric parameter independently (see Ref.[13] for more details on the calculation of coefficients a_j^{3D} , b_j^{3D} and c^{3D}). Given the response surface and assuming an accurate fit throughout the input space, probabilistic analyses can be conducted evaluating the f^{3D} as opposed to performing 3-D CFD simulations.

2.6.3 Input Distributions

For all the deformations except the clearances, the distributions are assumed Gaussian, and centered on the nominal geometry value. The deformations listed in Table 2.1 are assumed to be $\pm 2\sigma$ values.

For tip/hub clearance, the distribution is not centered and is bounded on one side by the nominal distance to the wall. In addition, the mean of the distribution is believed, from SNECMA experience, to be the nominal value. These requirements are not achievable with a log-normal distribution or even a beta distribution. For this purpose, a PDF and a cumulative density function (CDF) were built using polynomials. The constraints used were :

1. 95% of the probability is between clearance $\div 2$ and $\times 2$
2. The mean of the distribution must be the nominal value
3. Clearances cannot be decreased by more than the nominal distance to the wall.

Figure 2-9 shows the PDF that was developed to match the constraints. This PDF has an analytical form (a high-degree polynomial) and the corresponding CDF is created by integrating the PDF polynomial.

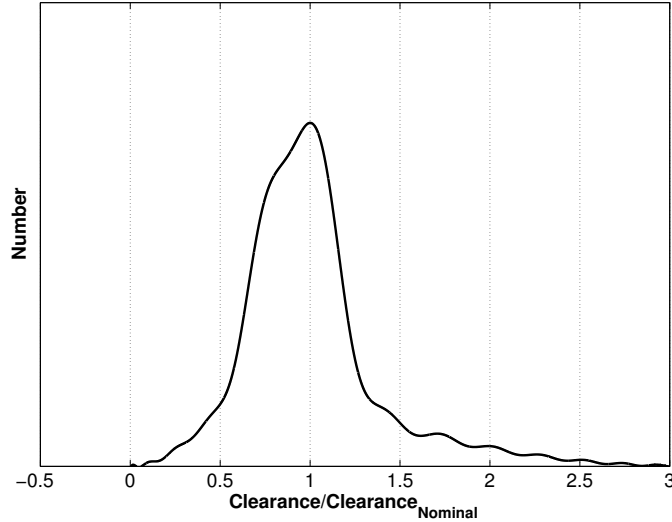


Figure 2-9: Input clearance distribution using the created CDF

2.6.4 Monte-Carlo Analysis Results with all Geometry Noises

A Monte-Carlo analysis was run on the response surface taking the input variables x_j from the distributions presented in the previous paragraph. The output PDF's and CDF's are shown in Figures 2-10 and 2-11 respectively. The conclusions from the Monte-Carlo analysis results are the following.

A mean shift can be observed in all plots. The mean efficiency is 0.45 point lower than the nominal efficiency, and the mean pressure ratio is 0.41 point lower than the nominal pressure ratio. If the requirement was set at the nominal value, this mean shift implies that the population of stages would not meet the nominal performance by a half point on average.

The standard deviation of the pressure ratio is 1.8 points. For the efficiency, the standard deviation is 2.0 points. These two figures imply that the input noise leads to a large performance variability.

The fifth percentile value for both efficiency and pressure ratio are 4 points below the nominal value. Thus 5% of all stages would miss the design efficiency and pressure ratio by 4 points. The potential for large performance misses can be seen in the large negative tails of efficiency and pressure ratio distribution in Figure 2-10.

The stalling pressure rise margin mean shift is favorable. The population has, on average, a larger stalling pressure rise margin than the nominal stage because of the trends in stalling pressure

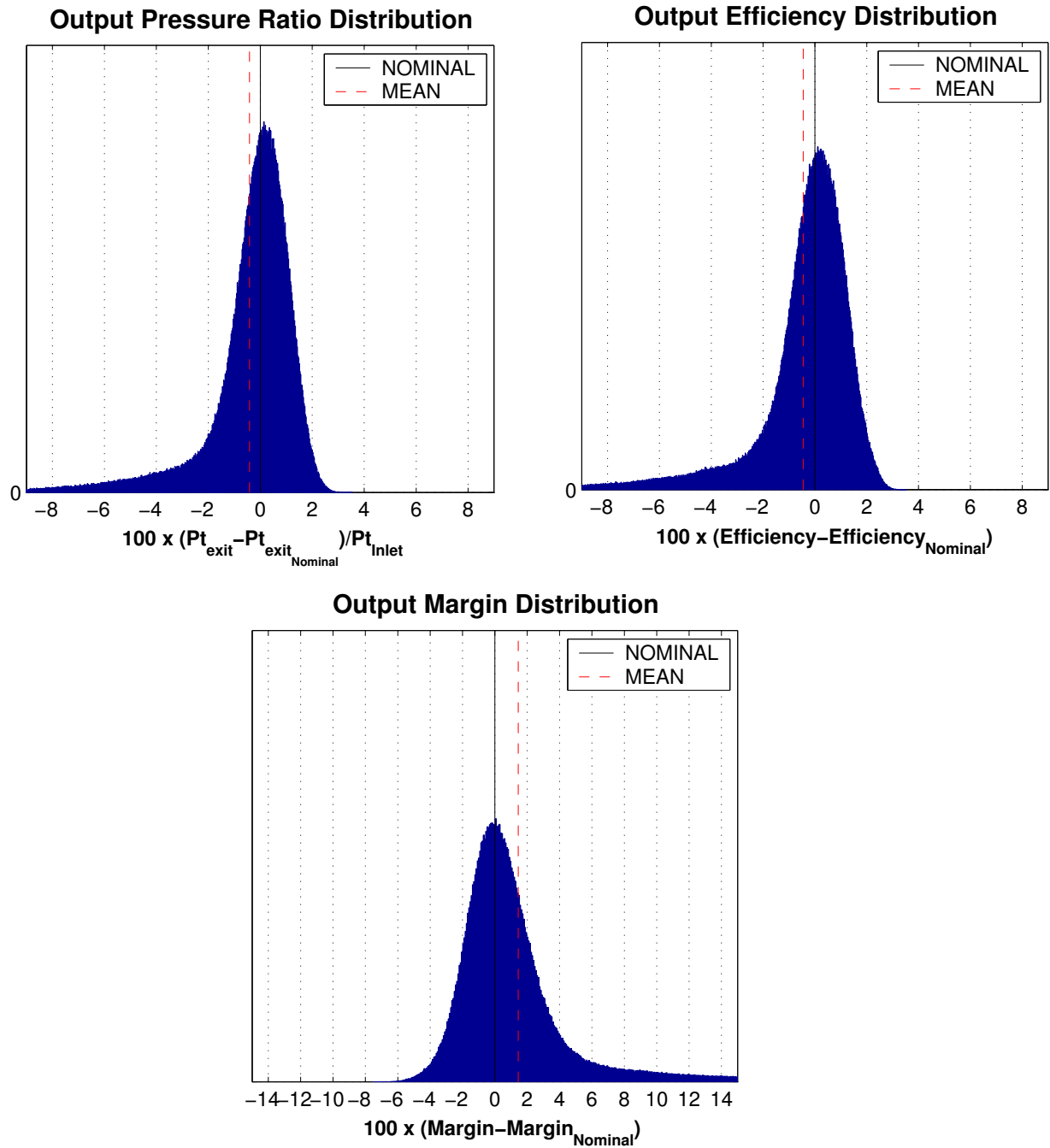


Figure 2-10: Output distributions from the Monte-Carlo analysis using the response surface based on 3-D simulations.

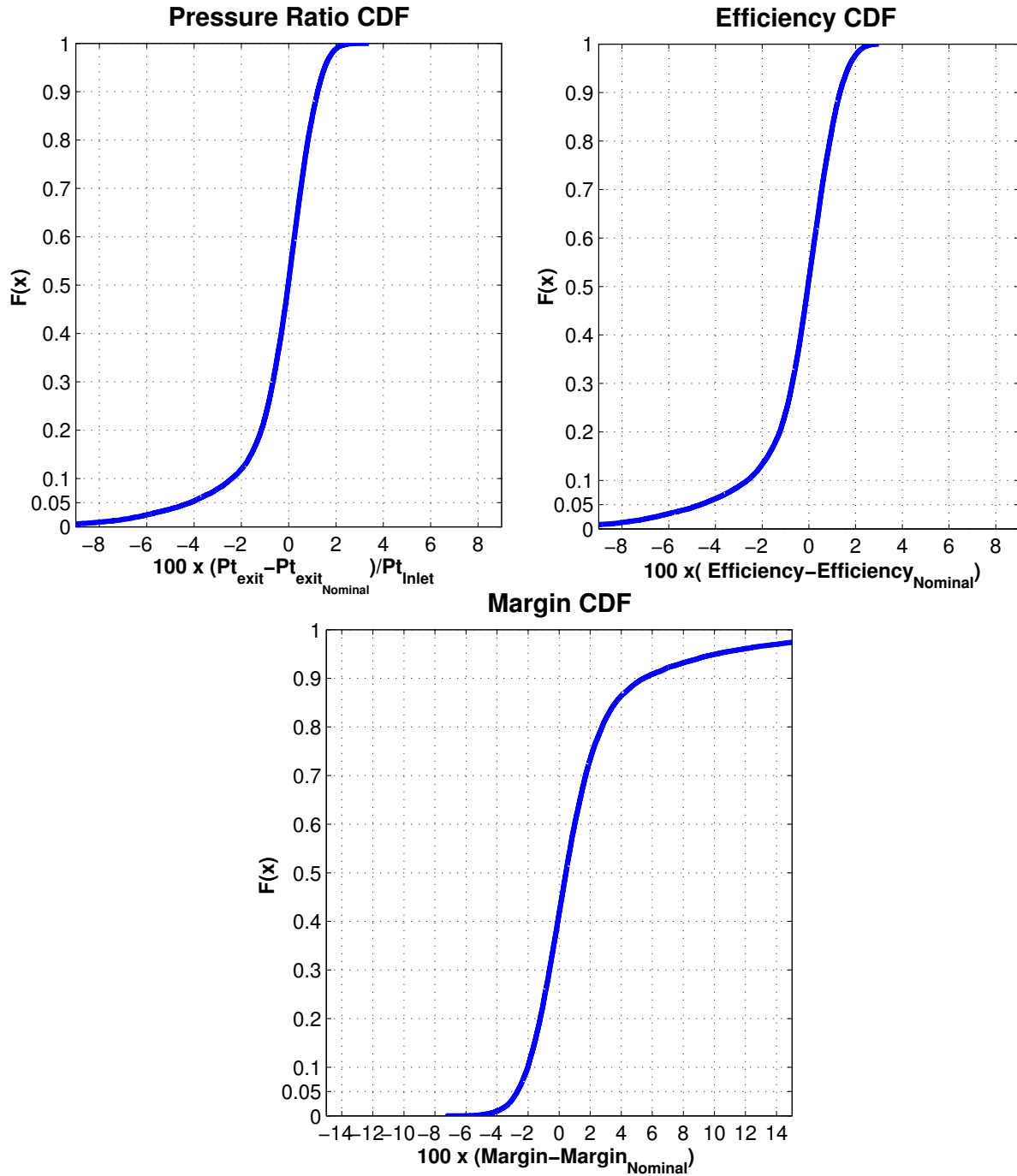


Figure 2-11: Output CDF's from the Monte-Carlo analysis using the response surface based on 3-D simulation.

rise margin sensitivities to clearance opening described previously.

2.6.5 Effect of Individual Geometric Noises on Mean Performance and Variability

In this section, we quantify the impact of individual noise variables on the output mean and variability. The goal is to determine which factors most contribute to a loss of performance. For this purpose, one can set to zero the variation (or noise) of the geometric variables one at a time and observe the impact on the output performance distributions. Tables 2.2, 2.3, and 2.4 and Figure 2-12 rank the five most important noise factors.

Rotor tip clearance appears in the probabilistic results as the most important geometric factor for mean shift. Figure 2-12 shows when the rotor tip clearance (R C) noise is set to zero, the mean shift of pressure ratio and efficiency are reduced by 63% and 57% respectively, which is considerable compared to the other noises. The second important geometric factor for mean shift is the rotor leading edge angle (R LEA). When no R LEA variation is applied on it, the pressure ratio mean shift is reduced by 11% and the efficiency mean shift by 15%.

Similar to the mean shift, the most important geometric factor for variability is, by far, rotor tip clearance. When no rotor tip clearance noise is applied, the standard deviation of the pressure ratio and efficiency are reduced by 70% and 75% respectively. After rotor tip clearance, the next most important parameters reduce the pressure ratio and efficiency by 2%-3% when the variation is removed.

With no rotor tip clearance noise, the fifth percentile distance to the nominal value is reduced by 75% for both pressure ratio and efficiency. This means that with a nominal efficiency of value η_{nom} , when all noises are applied, 95% of the stage population has higher efficiency than $\eta_{nom}-0.04$. When no rotor tip clearance noise is applied, 95% of the stage population have higher a efficiency than $\eta_{nom}-0.01$.

To summarize the findings, for the geometric noise that has been input, the variability of the stage performance can be substantial. For instance, the fifth percentile of efficiency is four points lower than the nominal and the mean shift is almost a half a point of efficiency. The geometric parameter that most impacts the performance uncertainty and mean shift is the rotor tip clearance, and then with much smaller impact, the rotor leading edge parameters. Rotor tip clearance therefore

appears to be the first geometric parameter upon which noise reduction should be applied to reduce the variability in pressure ratio and efficiency.

	<i>Row</i>	$100\left(\frac{\overline{P_o}-P_o}{P_{oin}}\right)$	$100(\overline{\eta}-\eta)$	$100(\overline{Mg}-Mg)$
All Applied		-0.41	-0.45	1.4
<i>Var. NOT Applied</i>	<i>Row</i>	$100\left(\frac{(\overline{P_o})_i-\overline{P_o}}{P_{oin}}\right)$	$100(\overline{\eta}_i-\overline{\eta})$	$100(\overline{Mg}_i-\overline{Mg})$
Clearance	R3	0.26 (1)	0.26 (1)	-1.0 (1)
Clearance	S3	0.009	-0.003	-0.043
Chord	R3	0.001	0.003	-0.007
Chord	S3	0.006	0.007	-0.016
LE Angle	R3	0.042 (2)	0.064 (2)	-0.10 (2)
LE Angle	S3	0.008	0.019 (5)	-0.026
TE Angle	R3	0.020 (4)	0.017	-0.062 (3)
TE Angle	S3	0.001	0.000	-0.013
LE Thick.	R3	0.024 (3)	0.035 (3)	-0.054 (4)
LE Thick.	S3	0.007	0.020 (4)	-0.021
TE Thick.	R3	0.013	0.010	-0.040
TE Thick.	S3	0.001	0.000	-0.011
Max Thick.	R3	0.018 (5)	0.015	-0.048 (5)
Max Thick.	S3	0.004	0.007	-0.011

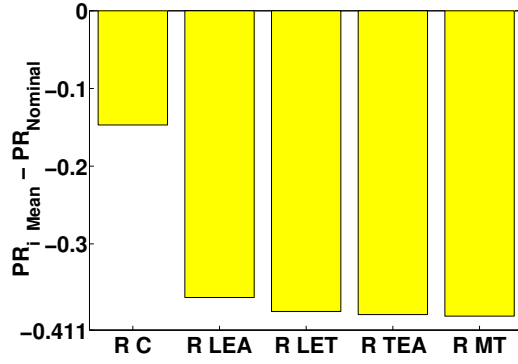
Table 2.2: Mean shift of the Monte-Carlo analysis results on the response surface of the 3-D simulations. Figures in parenthesis ranks the five most important noises.

<i>Var. NOT Applied</i>	<i>Row</i>	$100 \cdot \sigma_{\frac{P_o}{P_{o_{in}}}}$	$100 \cdot \sigma_{\eta}$	$100 \cdot \sigma_{Mg}$
All Applied		1.8	2.0	4.5
<i>Var. NOT Applied</i>	<i>Row</i>	$100 \left[\sigma \left(\frac{P_o}{P_{o_{in}}} \right)_i - \sigma \left(\frac{P_o}{P_{o_{in}}} \right) \right]$	$100(\sigma_{\eta_i} - \sigma_{\eta})$	$100(\sigma_{Mg_i} - \sigma_{Mg})$
Clearance	R3	-1.3 (1)	-1.5 (1)	-3.0 (1)
Clearance	S3	-0.004	-0.016 (3)	-0.11 (2)
Chord	R3	-0.007	-0.007	-0.018
Chord	S3	-0.008	-0.007	-0.024
LE Angle	R3	-0.017 (3)	-0.033 (2)	-0.047 (4)
LE Angle	S3	-0.006	-0.007	-0.018
TE Angle	R3	-0.056 (2)	-0.006	-0.072 (3)
TE Angle	S3	0.000	-0.001	-0.001
LE Thick.	R3	0.002	0.001	0.006
LE Thick.	S3	-0.008 (5)	-0.009 (4)	-0.022
TE Thick.	R3	-0.009 (4)	-0.007	-0.031 (5)
TE Thick.	S3	-0.002	-0.003	-0.003
Max Thick.	R3	-0.005	-0.004	-0.014
Max Thick.	S3	-0.007	-0.008 (5)	-0.019

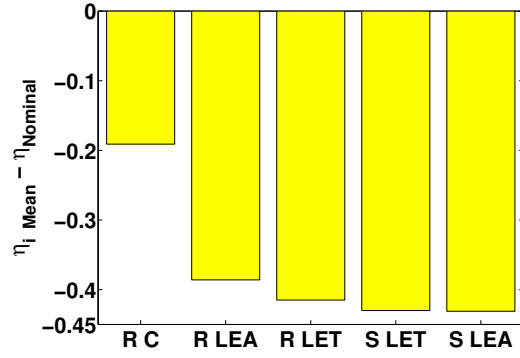
Table 2.3: Standard deviation of the Monte-Carlo analysis results on the response surface of the 3-D simulations. Figures in parenthesis ranks the five most important noises.

<i>Var. NOT Applied</i>	<i>Row</i>	$100\left(\frac{P_{o5\%}-P_o}{P_{oin}}\right)$	$100(\eta_{5\%} - \eta)$	$100(Mg_{5\%} - Mg)$
All Applied		-4.1	-4.6	-2.7
<i>Var. NOT Applied</i>	<i>Row</i>	$100\left(\frac{(P_{o5\%})_i-P_{o5\%}}{P_{oin}}\right)$	$100(\eta_{5\%_i} - \eta_{5\%})$	$100(Mg_{5\%_i} - Mg_{5\%})$
Clearance	R3	3.2 (1)	3.6 (1)	0.59 (1)
Clearance	S3	0.008	0.009 (3)	0.49 (2)
Chord	R3	0.022 (5)	0.032 (4)	0.009
Chord	S3	0.019	0.024	0.001
LE Angle	R3	0.051 (3)	0.092 (2)	0.064 (4)
LE Angle	S3	0.014	0.024	-0.018
TE Angle	R3	0.069 (2)	0.030 (5)	0.200 (3)
TE Angle	S3	-0.013	-0.002	-0.004
LE Thick.	R3	0.008	0.024	-0.054
LE Thick.	S3	0.015	0.029	-0.010
TE Thick.	R3	0.032 (4)	0.036 (3)	0.053 (5)
TE Thick.	S3	0.008	0.009	-0.008
Max Thick.	R3	0.008	0.015	-0.014
Max Thick.	S3	0.020	0.026	0.002

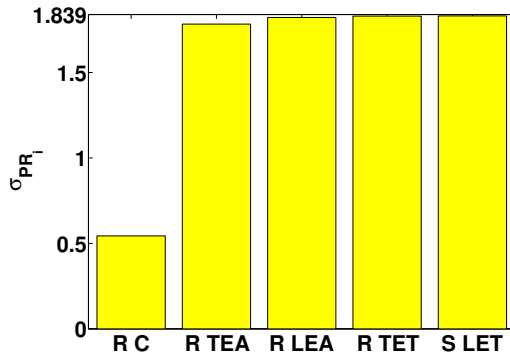
Table 2.4: Fifth percentile of the Monte-Carlo analysis results on the response surface of the 3-D simulations. Figures in parenthesis ranks the five most important noises.



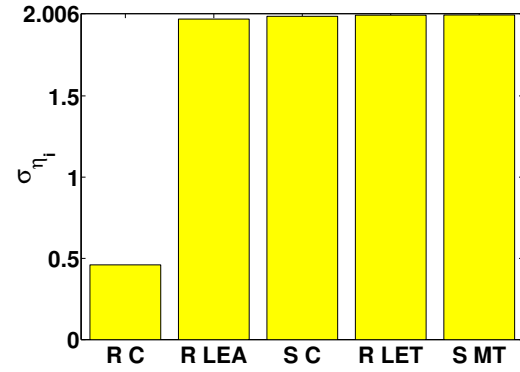
$$(a) 100 \left(\frac{\overline{(P_o)_i} - P_o}{P_{o_{in}}} \right)$$



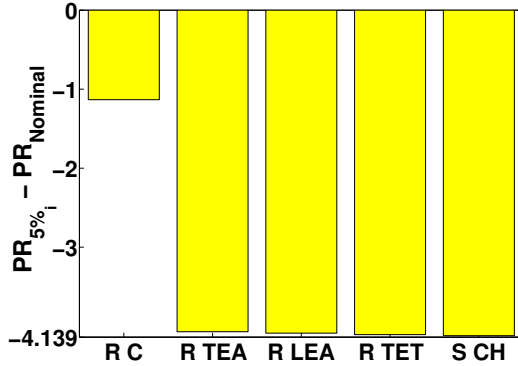
$$(b) 100(\overline{\eta}_i - \eta)$$



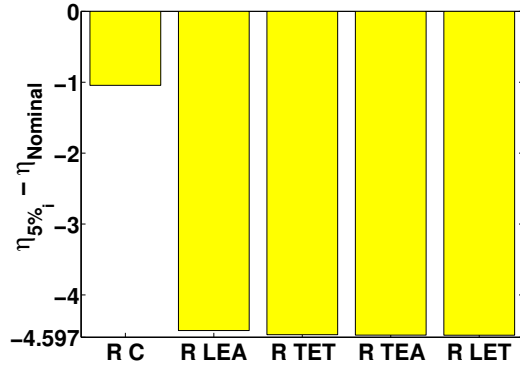
$$(c) 100 \cdot \sigma \left(\frac{P_o}{P_{o_{in}}} \right)_i$$



$$(d) 100 \cdot \sigma_{\eta_i}$$



$$(e) 100 \left(\frac{(P_{o_{5\%}})_i - P_o}{P_{o_{in}}} \right)$$



$$(f) 100(\eta_{5\%_i} - \eta)$$

Figure 2-12: Rank of the five geometric parameter that most impact the performances. The X-axis gives the parameter whose uncertainty is set to zero. R is for rotor, S for stator, C for clearance, LE for leading edge, TE for trailing edge, M for maximum, A for angle, T for thickness, and CH for chord.

Chapter 3

Flow Models for End-wall Effects

3.1 Introduction

One goal of this research was to create a compressor flow model for a probabilistic design tool that would include 3-D effects such as losses and blockage in the end-wall region, but which would be much faster computationally than a 3-D RANS solver. An appealing method for this purpose was the correlations presented in [10, 11, 15], because of the simplicity of implementation, experiment-based results, and successful use in the industrial design of compressors. However, this basic approach required modifications to account for the effects of end-wall flow blockage on the passage area contraction across a row (measured by the quantity $AVDR = \frac{\rho_2 V_{x_2}}{\rho_1 V_{x_1}} = \frac{A_1}{A_2}$). The importance of these effects on the model estimates of stage performance is illustrated by 3-D calculations, and is supported by the work of Horlock [8]. Using Horlock's analysis, we develop a simple extension of the GE correlations to account for these effects.

The main advantage of the meanline model is that the deterministic sensitivity results are obtained in a day or less, whereas the 3-D deterministic sensitivity analysis takes three months. Whereas a single meanline calculation takes about 3 minutes, a 3-D calculation takes between 30 to 40 hours.

3.2 GE End-wall Correlations

In [15] and [10], Koch and Smith present a method for estimating the displacement thickness and the loss in efficiency due to the flow in the end-wall region of a compressor stage as a function of the ratio of pressure rise over maximum pressure rise for a repeating stage. This method is based on experimental observations from low-speed compressors.

The procedure relates the efficiency losses due to end-walls to two properties of an end-wall boundary layer : the displacement thickness δ^* and the tangential-force thickness v [10]. The performance of the compressor is first calculated in the freestream region where the flow is not affected by the end-walls. The displacement thicknesses of the boundary layers at tip and hub are defined as [15],

$$\delta_{hub}^* = \frac{1}{r_{hub} \cdot \tilde{\rho}_{hub} \tilde{V}_{x_h}} \int_{r_{hub}}^{r_{hub} + \delta_{hub}} (\tilde{\rho} \tilde{V}_x - \rho V_x) r dr \quad (3.1)$$

$$\delta_{tip}^* = \frac{1}{r_{tip} \cdot \tilde{\rho}_{tip} \tilde{V}_{x_t}} \int_{r_{tip}}^{r_{tip} + \delta_{tip}} (\tilde{\rho} \tilde{V}_x - \rho V_x) r dr. \quad (3.2)$$

The boundary parameter related to tangential-force loss in the end-wall boundary layer as the displacement thickness is related to the flow loss is the tangential-force thickness :

$$v_{hub} = \frac{1}{r_{hub} \cdot \tilde{F}_{\theta_h}} \int_{r_{hub}}^{r_{hub} + \delta_{hub}} (\tilde{F}_\theta - F_\theta) r dr \quad (3.3)$$

$$v_{tip} = \frac{1}{r_{tip} \cdot \tilde{F}_{\theta_t}} \int_{r_{tip}}^{r_{tip} + \delta_{tip}} (\tilde{F}_\theta - F_\theta) r dr. \quad (3.4)$$

In reference [10], v is taken as a fixed fraction of δ^* based on the data. Koch and Smith found good agreement between predicted and measured pressure rise and efficiency using this assumption.

To calculate δ^* and v , the assumption is made that these quantities are only a function of $\frac{C_h}{C_{h_{max}}}$, geometry, and clearance. In the incompressible limit,

$$\frac{C_h}{C_{h_{max}}} = \left(\frac{\Delta P_R + \Delta P_S}{q_{1R} + q_{1S}} \right) / \left(\frac{\Delta P_R + \Delta P_S}{q_{1R} + q_{1S}} \right)_{max}. \quad (3.5)$$

The dependence on clearance is of the form [15]:

$$\frac{\delta^*}{g} = \frac{\delta^*}{g} \Big|_{\epsilon/g=0} + \frac{\epsilon}{g} \left[\left(\frac{\Delta P_R + \Delta P_S}{q_{1R} + q_{1S}} \right) / \left(\frac{\Delta P_R + \Delta P_S}{q_{1R} + q_{1S}} \right)_{max} \right]. \quad (3.6)$$

The original chart of these correlations with GE experimental data is available in Appendix B.2.

To calculate the actual quantities, the correlation follows the two-step procedure represented by Figure 3.2. First, at constant static pressure rise, the mass flow \dot{m} is reduced by an amount appropriate for the displacement thicknesses :

$$\dot{m} = \tilde{m} \left(1 - \frac{A^*}{A}\right) = \tilde{m} \left(1 - \frac{2(\delta_{tip}^* r_{tip} + \delta_{hub}^* r_{hub})}{r_{tip}^2 - r_{hub}^2}\right) \quad (3.7)$$

where ($\tilde{}$) quantities are freestream quantities. When $\frac{(r_{tip} - r_{hub})}{r_{tip}} \ll 1$,

$$\dot{m} \simeq \tilde{m} \left(1 - \frac{\delta_{tip}^* + \delta_{hub}^*}{h}\right) \quad (3.8)$$

where h is the height of the passage. Similarly, using the tangential-force thickness, the power applied to the blade can be written

$$\mathcal{P} = \Omega \mathcal{T} = \Omega \tilde{\mathcal{T}} \left(1 - \frac{v_t + v_h}{h}\right) \quad (3.9)$$

where Ω is the shaft angular velocity and \mathcal{T} the torque applied to the rotor. The stage efficiency is then related to the freestream efficiency $\tilde{\eta}$ by :

$$\eta = \frac{\Delta P}{\Omega} \frac{\dot{m}}{\mathcal{T}} = \tilde{\eta} \frac{1 - \frac{\delta_{tip}^* + \delta_{hub}^*}{h}}{1 - \frac{v_{tip} + v_{hub}}{h}} \quad (3.10)$$

The procedure to obtain the stage total pressure rise is described in Section 3.5.5.

3.3 Effect of End-wall Flow Blockage on the Freestream Flow : The AVDR

3.3.1 Blockage Results from the 3-D Calculations

In the repeating stage model, the velocity distributions at the exit of a stage are assumed to be the same as at the stage inlet. However, this assumption does not require that the velocity distributions and therefore the end-wall flow blockage remain constant within a repeating stage.

Figure 3-2 shows the evolution of the displacement thickness, δ^* , for both hub and tip along

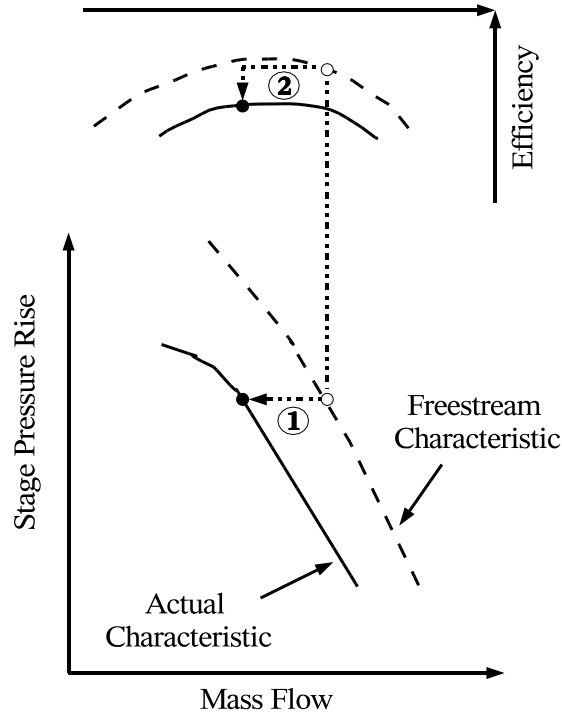
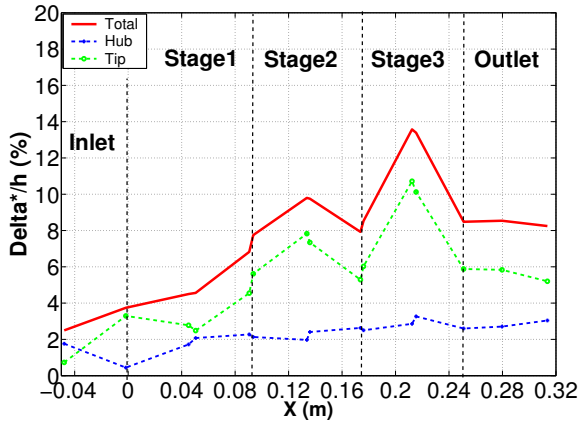


Figure 3-1: Two-step procedure to obtain the stage characteristic, from [15]

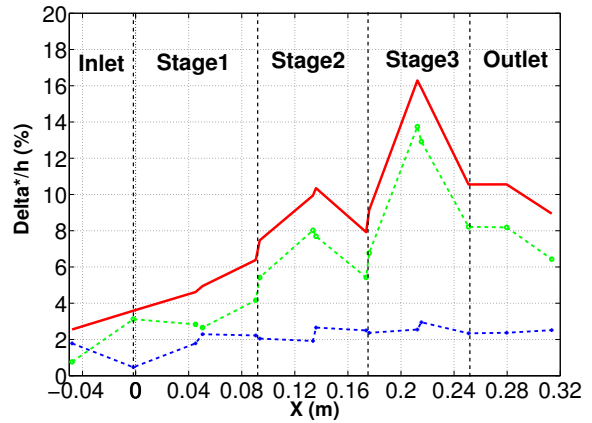
the three-stage compressor CREATE, for different geometries and exit conditions, and for the third stage only. In Figure 3-2 a, the first stage shows an increase in displacement thickness but in the second and third stage, a repeating pattern occurs. The displacement thickness at the tip δ_{tip}^* increases across the rotor, and then decreases across the stator, with a stage exit value close to the stage inlet value. At this design operating point therefore, for the nominal geometry, repeating behavior is seen. At a higher exit static pressure (Figure 3-2 b), the repeating stage behavior does not occur possibly because there is mismatch. The observed trends lead us to conclude that the repeating stage behavior is more likely to occur for well-designed compressors operating near design condition. For compressor flows with some stages operating nearer to stall, the repeating behavior is less likely to occur. This is clearly the case for Figure 3-2 b where the third stage seems to be nearer to stall than the second stage.

A related effect is observed in the simulations performed only on the third stage with fixed inlet

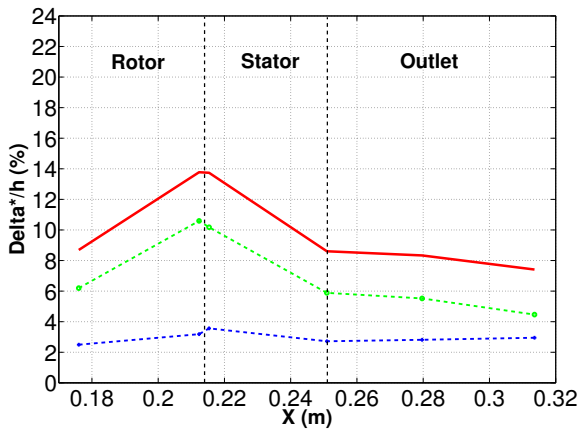
conditions based on the results of a nominal simulation of the entire compressor (shown Figure 3-2 c and d). The former shows a repeating behavior, however for the double clearance situation in Figure 3-2 d, the exit boundary layers are larger than the inlet. In addition, the variation of δ_{hub}^* across the compressor can be seen to be minor relative to the variation of δ_{tip}^* , implying that hub and tip displacement thicknesses behave differently.



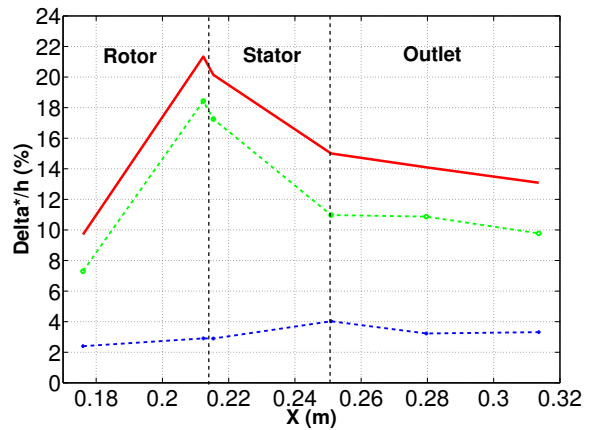
(a) Simulation of the entire compressor at operating point



(b) Simulation of the entire compressor at high pressure ratio $\pi/\pi_{nominal} = 1.044$



(c) Simulation of the third stage at peak efficiency, nominal geometry



(d) Simulation of the third stage at $\pi/\pi_{nominal} = 0.96$, tip and hub clearances multiplied by two

Figure 3-2: Evolution of the blockage at hub and tip for (a) CREATE compressor at operating point, nominal geometry (b) CREATE compressor at $\pi/\pi_{nominal} = 1.044$, nominal geometry (c) STAGE3 at at peak efficiency, nominal geometry (d) STAGE3 at $\pi/\pi_{nominal} = 0.96$, tip and hub clearances multiplied by two

3.3.2 Comparison of blockage behavior at hub and tip

As observed, the hub end-wall thicknesses are relatively constant along the compressor. This behavior can be corroborated by a more detail inspection of the total pressure distributions from the 3-D simulations. In fact, from Crook [2], it is known that the end-wall flow blockage appears to be directly linked to low total pressures associated with the clearance flow. We have considered a case where both the rotor and stator have double clearance and plotted lines of iso-total pressure on different axial cuts from leading edge to trailing edge using the coefficient C_{p_o} ,

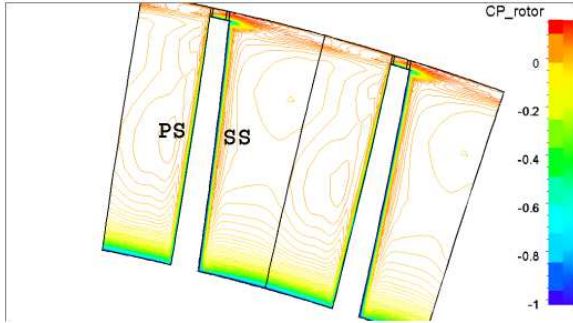
$$C_{p_o} = \frac{P_o - P_{o_{in}}}{P_{o_{in}} - P_{in}}. \quad (3.11)$$

The total pressure is relative for the rotor and absolute for the stator. The plots for the rotor are shown in Figure 3-3 and in Figure 3-4 for the stator.

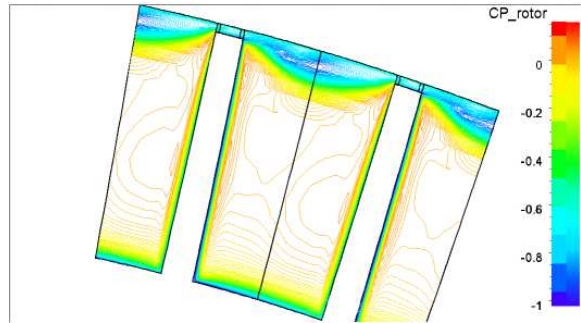
Crook [2] observes the location of the clearance vortex core is well approximated by the center of the concentric low total pressure distribution in the end-wall region. The vortex core can be then localized in Figure 3-3 and Figure 3-4. The tip clearance vortex is traveling much faster from the suction side to the pressure side than the hub clearance vortex. At 10% of the chord (Fig. 3-3 b), the tip vortex has already reached the next blade whereas the hub vortex is still close to the clearance gap. Then, from 10% of chord to trailing edge, the tip clearance vortex expands radially to take half of the flow path area at the trailing edge (Fig. 3-3 e). In contrast, the hub clearance vortex reaches the pressure side of the next blade at about 60% of the chord and does not diffuse radially. The cause of this difference in the end-wall behavior remains to be explained.

3.3.3 Effect of End-wall Flow Blockage on Freestream Flow Quantities

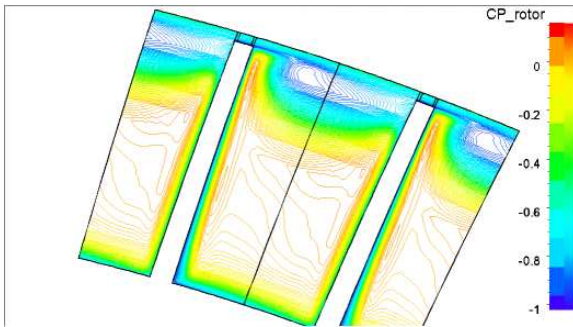
In the previous section, a variation of end-wall flow blockage across the compressor and, in particular across the third stage was shown. Although the effect of AVDR has been known a long time, the effect of end-wall boundary layer variation is less known. In fact, Koch and Smith [10, 11, 15] assumed constant end-wall boundary layer across the repeating stage and found good agreement with the experiment. However, all the stage's blades used in developing these correlations had aspect ratios higher than two and the stages were run in the design region. Therefore, the effect of end-wall boundary layer variation was not as important as in our particular case where



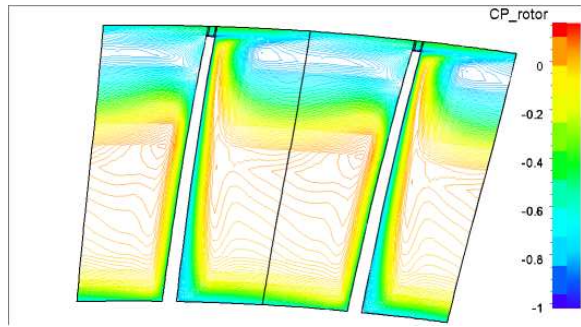
(a) 10% of rotor chord



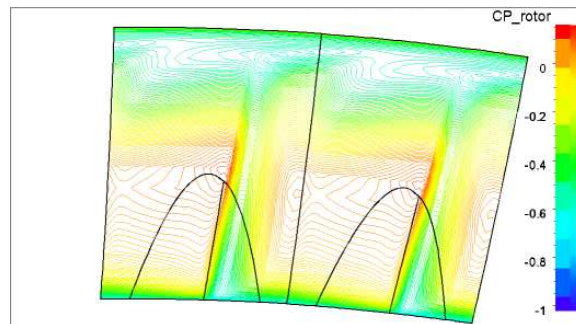
(b) 30% of rotor chord



(c) 60% of rotor chord

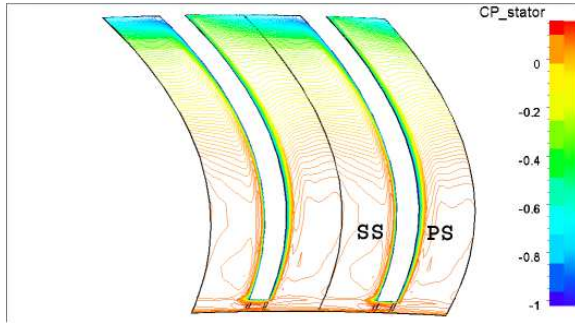


(d) 80% of rotor chord

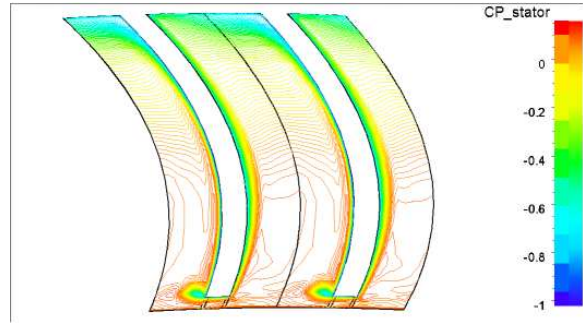


(e) trailing edge of rotor

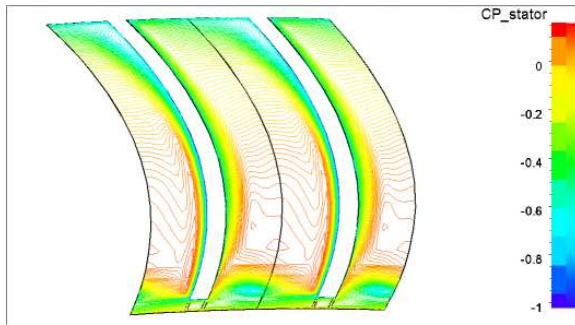
Figure 3-3: Isoline of rotor $C_{p_o} = \frac{P_o - P_{o_{in}}}{P_{o_{in}} - P_{in}}$ at 10% chord (a), 30% (b), 60% (c), 80% (d) and just after the trailing edge (e). PS is for pressure side and SS for suction side



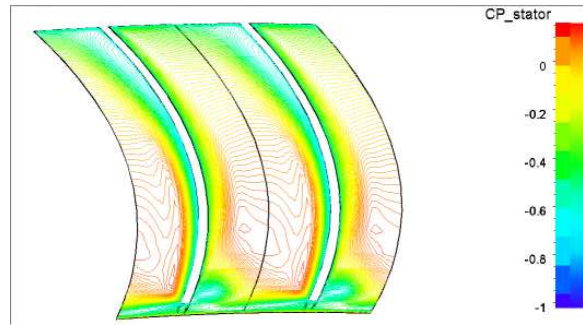
(a) 10% of stator chord



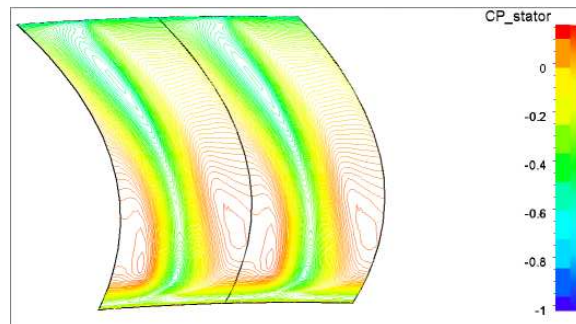
(b) 30% of stator chord



(c) 60% of stator chord



(d) 80% of stator chord



(e) trailing edge of stator chord

Figure 3-4: Isoline of stator $C_{p_o} = \frac{P_o - P_{o_{in}}}{P_{o_{in}} - P_{i_{in}}}$ at 10% chord (a), 30% (b), 60% (c), 80% (d) and just after the trailing edge (e). PS is for pressure side and SS for suction side

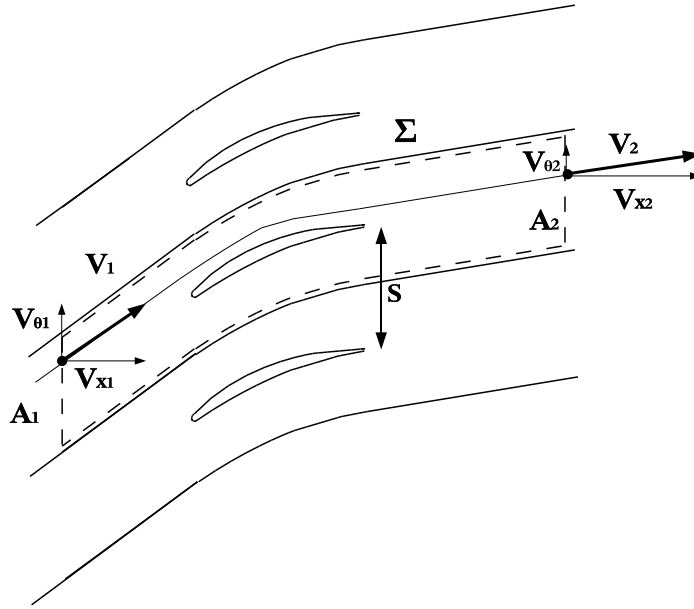


Figure 3-5: Σ -contour on a stream-surface across a blade passage

the third stage has an aspect ratio lower than one and where the cases with varied clearances have flows that can be far from normal operations; as shown in Figure 3-2 b and d.

The change in the end-wall blockage variation across the stage with geometry variation can have a significant impact on the freestream flow quantities and therefore play an important part in the sensitivity of the stage performance to geometry variations. In this section, reproducing the end-wall flow blockage behavior observed in the 3-D calculations, the effects of blockage in the end-wall region on the freestream flow are observed using MISES, and explained using a very simple 1-D incompressible flow model. The purpose of this study is to show the necessity in our case, of a model for the end-wall flow blockage within a stage. In this study, the end-wall flow blockage is shown to reduce the freestream static pressure by 1.4% and the total pressure ratio by 1.1% compared with the case with no end-wall boundary layer variation.

Consider a stream-surface at the mean radius across a blade row (see Figure 3-5) for an incompressible, non-viscous fluid. A_1 and A_2 are the passage areas at location 1 and 2, and the product of the spacing (s) which is constant and the respective local passage height (h_1) and (h_2). We denote (geom) the case where the AVDR is the flow path geometric area ratio and (inc) the case where we increase the displacement thickness at the passage outlet due to end-wall flow blockage.

Considering the contour Σ in Figure 3-5 and using continuity, it is found that

$$V_{x2(inc)} = V_{x2(geom)} \frac{h2(geom)}{h2(inc)}. \quad (3.12)$$

Now, if we assume that the exit flow angle at the blade trailing edge are fixed to the metal angle value, the change in exit tangential velocity can be expressed,

$$V_{\theta2(inc)} = V_{\theta2(geom)} \frac{h2(geom)}{h2(inc)}, \quad (3.13)$$

as well as the change in $\Delta V_\theta = V_{\theta1} - V_{\theta2}$

$$\Delta V_{\theta(inc)} - \Delta V_{\theta(geom)} = V_{\theta2(geom)} \left(1 - \frac{h2(geom)}{h2(inc)} \right). \quad (3.14)$$

Bernoulli equation gives the pressure rise variation,

$$\Delta P = \frac{\rho}{2} (V_{x1}^2 - V_{x2}^2) + \frac{\rho}{2} (V_{\theta1}^2 - V_{\theta2}^2), \quad (3.15)$$

and Euler equation the relation between the and the total pressure rise :

$$\frac{\Delta P_{oabs}}{\rho} = \Omega r \Delta V_\theta \quad (3.16)$$

Now, using MISES, the third stage was first run with the nominal flow path geometry, then the contraction of the passage was increased across the rotor alone case (a), decreased across the stator alone (b) and finally both simultaneously (c). This method allowed us to separate the effect of the increase of end-wall flow blockage across the rotor and the decrease across the stator. The results are summarized in Tables 3.1 and 3.2 and all the quantities are normalized by the nominal quantities.

Table 3.1: The Three AVDR Variation Cases

Case	a	b	c
AVDR Rotor	1.0526	1.0000	1.0526
AVDR Stator	1.0000	0.9492	0.9492

Table 3.2: AVDR Variation Effects on Freestream Quantities

Case	AVDR	$\left(\frac{P_2}{P_1}\right)_R$	$\left(\frac{P_{o_{abs2}}}{P_{o_{abs1}}}\right)_R$	$ \Delta V_\theta _R$	ω_R	$V_{x_{2R}}$	$V'_{\theta_{2R}}$
a	Rotor	0.9830	0.9903	0.9705	0.9608	1.0654	1.0343
b	Stator	1.0000	1.0000	1.0000	1.0000	1.0000	1.0000
c	Both	0.9830	0.9903	0.9705	0.9608	1.0654	1.0343
Case	AVDR	$\left(\frac{P_2}{P_1}\right)_S$	$\left(\frac{P_{o_{abs2}}}{P_{o_{abs1}}}\right)_S$	$ \Delta V_\theta _S$	ω_S	$V_{x_{2S}}$	$V_{\theta_{1S}}$
a	Rotor	0.9925	0.9987	0.9605	1.1123	1.0729	0.9787
b	Stator	1.0092	0.9997	1.0002	1.0276	0.9430	1.0000
c	Both	1.0033	0.9983	0.9606	1.1395	1.0106	0.9787

In case (a), an increase in $V_{x_{2R}}$ and $V_{\theta_{2R}}$ is observed, which is explained by Equation 3.12 and Equation 3.13 respectively, where $\frac{h_{2(geom)}}{h_{2(inc)}} > 1$. Therefore, both terms of the right hand side of Equation 3.15 are reduced which decreases the rotor static pressure rise. The rotor total pressure decrease comes from the reduction of ΔV_{θ_R} (Equation 3.16).

The stator ΔV_θ of case (a) is significantly lower than in the nominal case. This is a result of a change in stator inlet conditions due to matching with the rotor. Thus, the stator inlet tangential velocity V_{θ_1} is reduced, decreasing ΔV_{θ_S} and the stator static pressure rise (Equation 3.15). As the stator is not rotating, the absolute total pressure is only affected by the diffusion losses. Since the diffusion losses are not substantially changed, the total pressure is not significantly altered as in case (a), nor in any of the other cases.

In case (b), the rotor performance is unaffected and therefore the stator inlet conditions are identical to the nominal case. The stator absolute total pressure rise does not vary since the inlet flow conditions are identical, implying similar diffusion losses. Using the same arguments as in case (a) for the rotor AVDR increase, we can explain the increases in stator static pressure rise due to AVDR decrease.

Case (c) is a result of the combination of case (a) and (b) effects. There is an overall 1.4% decrease in static pressure ratio and 1.1% total pressure ratio a decrease across the entire stage. This proves that assuming no end-wall flow blockage variation across the stage can lead to an erroneous calculation of C_h .

3.4 The End-wall Blockage Model of Horlock [8]

The observed increase of the tip blockage across the rotor and the subsequent decrease of the tip blockage across the stator have been discussed by Horlock [8]. From the experimental data for repeating stages collected from Smith [15], Cumpsty [3] and Howard [9], Horlock [8] deduces that the repetition occurs not only after the stators of the repeating stages but also after the rotors and that the profiles at exit of stators and rotors are clearly different from each other. He states that in a repeating stage with constant passage height h , the sum (rotor plus stator) of the axial component of the blade forces must be constant along the blade span because the pressure rise is constant along the blade span.

In a rotor with tip clearance, there is a region where there is no blade force and thus a force deficit. But the pressure difference along the blade stays constant. The resulting difference between the integrated axial force and the product of pressure change times area (which is negative) will reduce the axial momentum of the flow and increase the blockage. In the subsequent stator which does not have clearance, an equal but opposite difference must exist since the sum (rotor plus stator) of the axial component of the blades forces is constant. Horlock [8] uses the axial force deficit thickness introduced by Smith [15] :

$$\nu_x = \int \left(1 - \frac{f_x}{F_x}\right) dz \quad (3.17)$$

where f_x is the local blade force in the deficit region and F_x is the axial force on the blade per unit length in the freestream. For the rotor (subscript R), $F_{xR} = s \cdot \Delta P_R$. He then shows that the pitch-averaged change in axial momentum thickness in the clearance region across the rotor can be written as :

$$(\Delta \bar{\theta}_x)_R = \frac{(F_x)_R (\nu_x)_R}{s \rho \bar{V}_x^2} \quad (3.18)$$

From [7], Horlock states that the axial force deficit thickness $(\nu_x)_R$ is a product of an empirical constant K ($O(1)$) and the tip clearance ϵ , and that the boundary layer shape factor is constant. Then, relating the momentum thickness $(\Delta \bar{\theta}_x)_R$ with the displacement thickness $(\Delta \bar{\delta}_x^*)_R$ through the boundary layer shape factor H , the change in axial blockage across the rotor $(\Delta A_{bx})_R$ is

$$(\Delta A_{bx})_R = s(\Delta \bar{\delta}_x^*)_R = sH(\Delta \bar{\theta}_x)_R = \frac{(F_x)_R (KH)\epsilon}{\rho \bar{V}_x^2}. \quad (3.19)$$

Since the value of K from experiment is in the interval (1,2), and the shape factor for boundary layer is about one, Horlock [8] empirically sets the constant (KH) to 2. It is then possible to calculate the change in axial displacement thickness across each row when the clearance is only on the rotor

$$\begin{cases} (\Delta\delta_x^*)_R = R \frac{(\Delta P)_{stage}}{\frac{1}{2}\rho V_x^2} \epsilon_{tip} \\ (\Delta\delta_x^*)_S = -R \frac{(\Delta P)_{stage}}{\frac{1}{2}\rho V_x^2} \epsilon_{tip} \end{cases} \quad (3.20)$$

where R is the reaction of the stage. For a hub clearance on the stator,

$$\begin{cases} (\Delta\delta_x^*)_S = (1 - R) \frac{(\Delta P)_{stage}}{\frac{1}{2}\rho V_x^2} \epsilon_{hub} \\ (\Delta\delta_x^*)_R = (R - 1) \frac{(\Delta P)_{stage}}{\frac{1}{2}\rho V_x^2} \epsilon_{hub}. \end{cases} \quad (3.21)$$

3.5 An Empirically Based Meanline Model for the Third Stage

In this section, the model used to account for the end-wall flow losses and blockage is presented. The validity of these assumptions is assessed by comparison to the 3-D calculations. The four assumptions are the following.

1. Constant δ_{hub}^* and δ_{tip}^* at the inlet of the third stage
2. No variation of δ_{hub}^* across the stage
3. $\Delta(\delta_{tip}^*)$ across the rotor is calculated from Horlock's [8]
4. The exit value δ_{tip}^* is given by the repeating stage estimate from the correlations of Koch and Smith [10, 15].

3.5.1 Constant δ_{hub}^* and δ_{tip}^* at the Inlet

The inlet conditions to the third stage used in the sensitivity analysis correspond to the operating point of the three-stage compressor at nominal geometry. Inlet total pressure, temperature and absolute flow angle thus are the same for all cases.

Figure 3-6 a and b show δ_{hub}^* and δ_{tip}^* at the inlet versus the rotor tip clearance. In Figure 3-6 a, for δ_{hub}^* , the data is tightly clustered. For δ_{tip}^* however, the data has a scatter. For the high clearance cases [$\epsilon/h = 0.035$], points have higher δ_{tip}^* than at nominal. This difference is due to the effect of the third stage rotor tip clearance on the upstream flow at the inlet close to the end-wall.

Comparing Figure 3-6 a and Figure 3-6 b, it can be observed that the scatter for the nominal clearance is largely due to points on the speedline that were run near stall or near choking, and were not used for the sensitivity analysis. For the cases where the rotor tip clearance is halved, all the values of δ_{tip}^* are lower than the nominal and the scatter is reduced.

To summarize, the assumption of a constant δ_{hub}^* at the inlet seems to be valid. However, δ_{tip}^* does vary at the inlet, in particular for cases where the rotor tip clearance is changed or when the stage is off-design. Since the off-design cases were not used for the sensitivity analysis, the only cases where the assumption of constant inlet tip displacement thickness will have an impact is the doubled rotor clearance. All of the other 27 cases (nominal and halved rotor tip clearance) are in the design region and δ_{tip}^* does not vary much (Figure 3-6 b).

3.5.2 No Variation in δ_{hub}^*

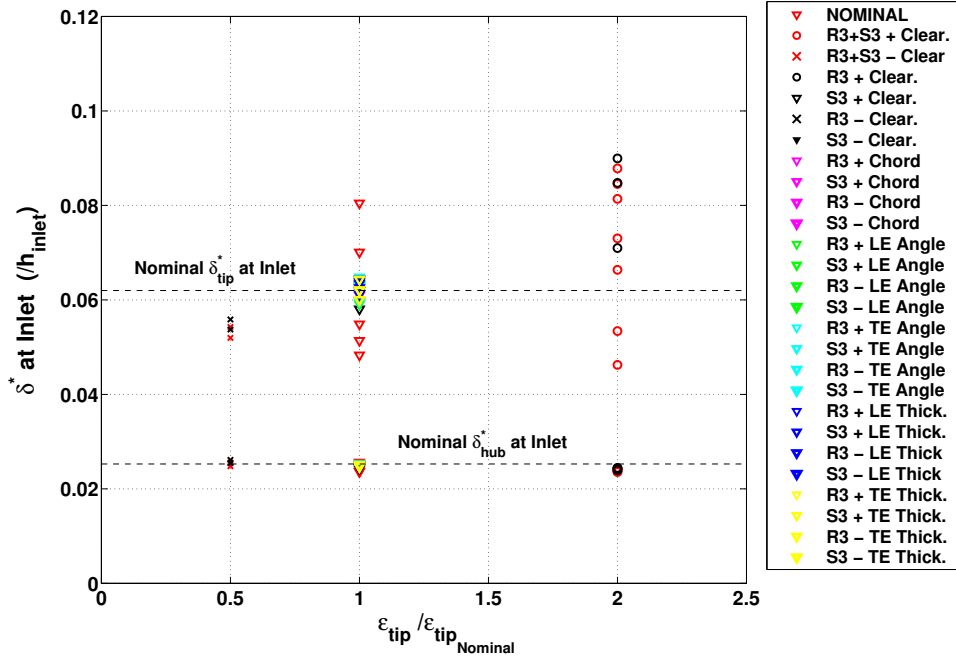
Figure 3-7 shows the value of δ^* at hub and tip along the third stage from the 3-D calculations. The figure show that although the tip displacement thickness can change by more than +12% of the passage height, depending on the geometry and conditions, the hub displacement thickness changes by less than 2% of the passage height across the stage for all the cases. Thus, the assumption that δ_{hub}^* is constant across the compressor seems close to the 3-D calculation and is considered valid. However, as discussed in Section 3.3.2, the reason for this behavior is unknown.

3.5.3 Calculation of $\Delta(\delta_{tip}^*)$ across the rotor from Horlock's model [8]

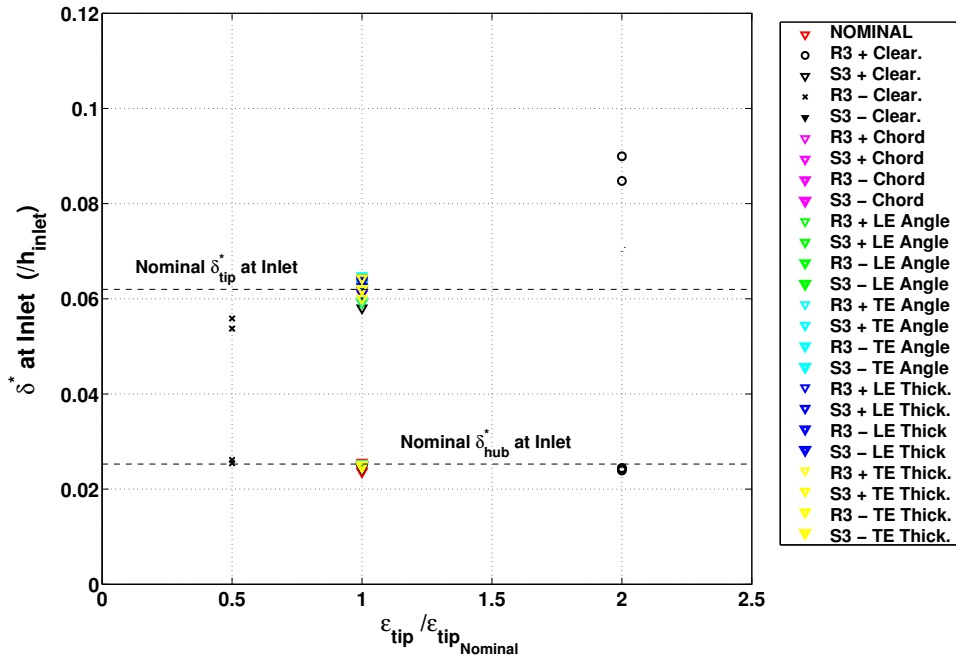
From Equation 3.20, the increase in displacement thickness at the rotor tip and the decrease through the stator can be expressed for a repeating stage. The increase in blockage through the rotor can be written from Equation 3.20 as

$$(\Delta\delta_x^*)_{rotor} = \left(\frac{\Delta P}{\frac{1}{2}\rho\bar{V}_x^2} \right)_{rotor} \epsilon_{tip} \quad (3.22)$$

From the 3-D calculations, $(\Delta\delta_x^*)_{rotor}$ is plotted as a function of $\left(\frac{\Delta P}{\frac{1}{2}\rho\bar{V}_x^2} \right)_{rotor} \epsilon_{tip}$. Comparing Figure 3-8 a and b, most of the points used for the sensitivity analysis are close to the dashed line which represents Horlock's model. The only points in Figure 3-8 b that are not close to the dashed line are the two double tip clearance cases. In Figure 3-8 a, the points that are the furthest from Horlock's



(a) All 3-D third stage calculations including rotor+stator clearance variation cases and the entire nominal geometry speedline



(b) Only 3-D third stage calculations used for the sensitivity analysis

Figure 3-6: Variation of δ^* at the inlet of the third stage for (a) all the 3-D calculations conducted and (b) only the calculations used for the sensitivity analysis. Points at the bottom of the figure are δ_{hub}^* and points at the top are δ_{tip}^*

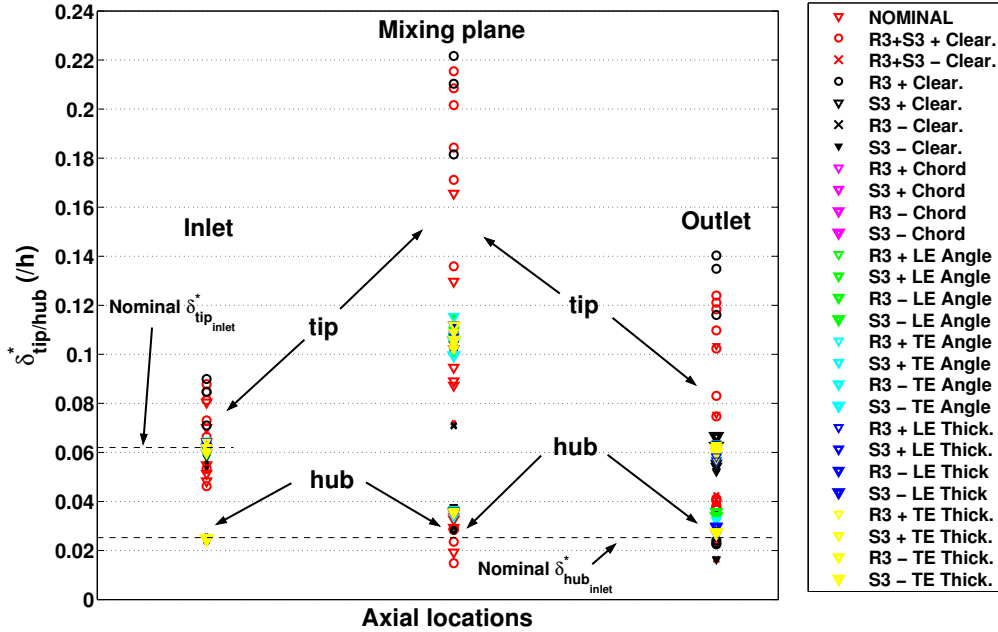


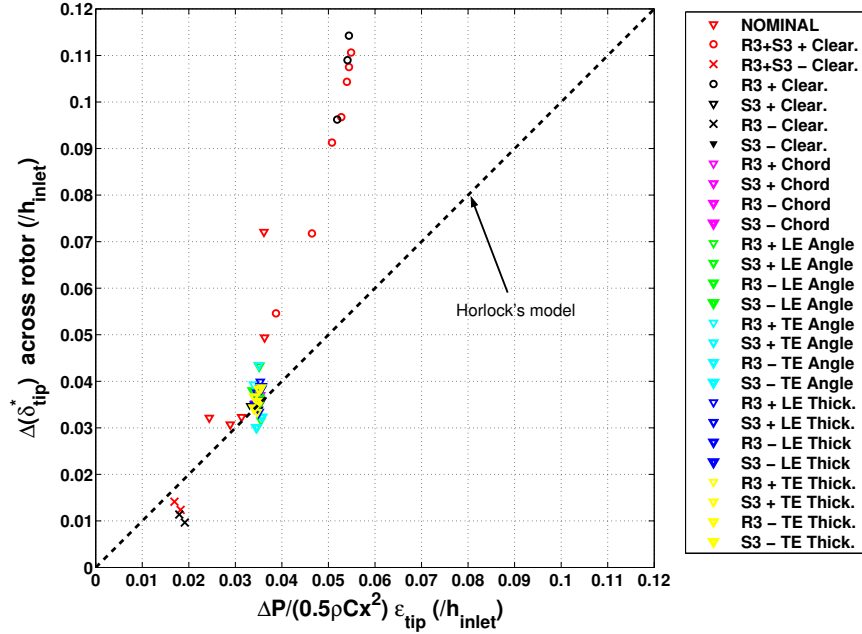
Figure 3-7: Variation of δ^* across the third stage for all the 3-D calculations conducted. The first location on the X-axis from the left is the inlet of the stage. In the middle is the mixing plane between rotor and stator and on the right is the exit of the stator.

model are off-design (near stall and near choking) with nominal tip clearance or have doubled tip clearance. One explanation for this phenomenon is that the flow close to the wall is observed to separate for most of these high clearance and off-design cases and that the boundary layers cannot be treated the same way as on-design cases. Horlock's assumption of constant shape factor may be therefore valid only near design with reasonable clearance.

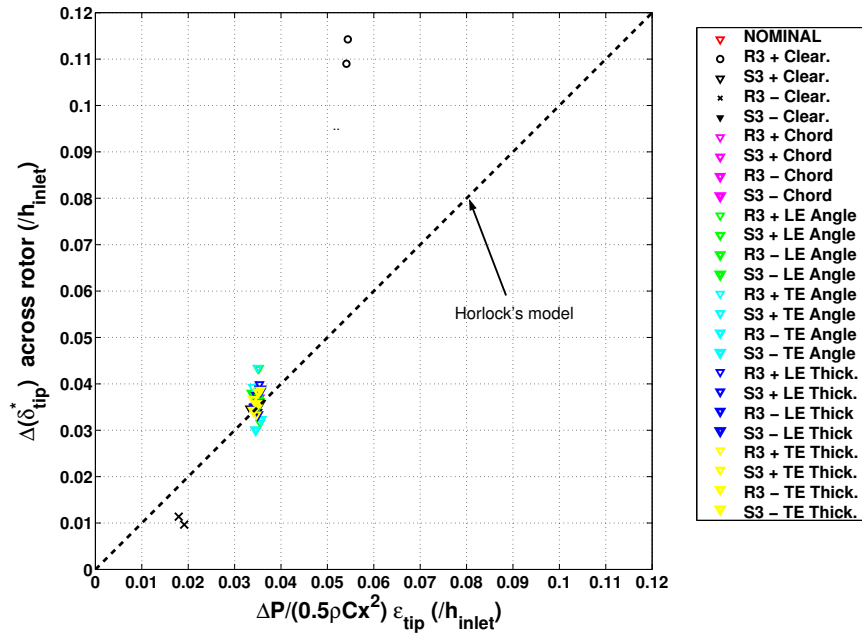
To summarize, Horlock's model on the increase of displacement thickness is applicable for all the sensitivity analysis except the tip clearance where it underestimates the growth in end-wall boundary layer across the rotor.

3.5.4 Repeating stage value of δ^*_{tip} after the stator

According to Horlock, the decrease in tip region displacement thickness across the stator in a repeating stage context should be the opposite of the increase across the rotor. So, the displacement thickness at the exit are the same as the inlet. However, in the cases considered here, the geometry perturbation changes the repeating stage value. In the proposed approach, we assume that the



(a) All 3-D third stage calculations including rotor+stator clearance variation cases and the entire nominal geometry speedline



(b) Only 3-D third stage calculations used for the sensitivity analysis

Figure 3-8: $\Delta(\delta_{tip}^*)_{rotor}$ as a function of $\left(\frac{\Delta P}{\frac{1}{2}\rho V_x^2}\right)_{rotor} \epsilon_{tip}$ for (a) all the 3-D calculations conducted and (b) only the calculations used for the sensitivity analysis. The quantities are normalized by the inlet passage height h_{inlet} . The dashed line represents Horlock's model.

exit displacement thickness is equal to the repeating stage value from [10, 15]. The assumption is essentially that a transition from one repeating stage value of displacement thickness to another occurs across a single stage.

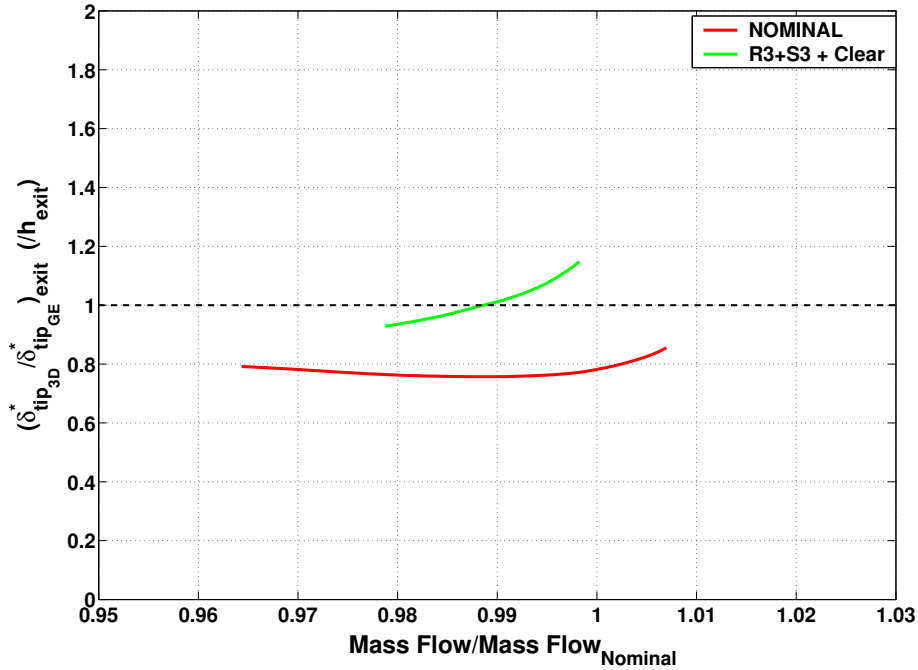


Figure 3-9: Ratio of $\delta_{tip_{3D}}^*$ and $\delta_{tip_{GE}}^*$ at exit as a function of mass Flow. The red line represents the nominal geometry speedline, the green line the double clearance speedline.

To assess the validity of this assumption, Figure 3-9 shows the ratio of the actual value of δ_{tip}^* from the 3-D calculations and the value of δ_{tip}^* applied in the meanline analysis from the repeating stage value from [10, 15] using the peak efficiency mass flow adjustment presented previously. Only two speedlines are shown because only two complete speedlines were calculated with the 3-D simulation. For the nominal geometry, the ratio is about 0.8 and the variation of the 3-D δ_{tip}^* along the speedline is close to the variation of the GE δ_{tip}^* from the repeating stage correlations. For a clearance of twice the nominal value on both rotor and stator, the ratio is close to 1. These computations support the assumption that δ_{tip}^* after the stator is the repeating stage value calculated from the GE correlations.

3.5.5 Calculation of the stage performance

Once the meanline calculation is run with the end-wall flow blockage calculated from the four assumptions described previously, the freestream inlet and exit quantities are known. We can then apply the end-wall flow blockage and loss estimates to calculate the effect on the stage performance. Using the repeating stage value δ_{tipGE}^* , the efficiency is :

$$\eta = \tilde{\eta} \frac{1 - \frac{\delta_{tipGE}^* + \delta_{hubGE}^*}{h}}{1 - \frac{v_{tipGE} + v_{hubGE}}{h}}, \quad (3.23)$$

and the mass flow :

$$\dot{m} \simeq C \rho_{in} \tilde{V}_{x_{in}} A_{geom_{in}} \left(1 - \frac{\delta_{tip_{in}}^* + \delta_{hub_{in}}^*}{h} \right) \quad (3.24)$$

where A_{geom} is the geometrical area of the flow path (without the displacement thickness) and C is the mass flow adjustment constant to match 3-D and meanline peak efficiency at nominal geometry. The actual static pressure rise is known since it is the same as the freestream. The stage efficiency is:

$$\eta = \frac{\dot{m}(h_{o2_{is}} - h_{o1})}{\mathcal{P}}, \quad (3.25)$$

where \mathcal{P} , the power, equals the actual torque applied to the blade times the wheel speed. Using the force deficit thickness, the power is :

$$\mathcal{P} = \Omega \mathcal{T} = \Omega \tilde{\mathcal{T}} \left(1 - \frac{v_{tipGE} + v_{hubGE}}{h} \right) \quad (3.26)$$

From the Euler equation, the power applied on the blade without clearance can be expressed as,

$$\mathcal{P} = \Omega \tilde{\mathcal{T}} = \dot{m}(\tilde{h}_{o2} - h_{o1}) = c_p \dot{m}(\tilde{T}_{o2} - T_{o1}). \quad (3.27)$$

Equations 3.26 and 3.27 allow Equation 3.25 to be rewritten as,

$$\eta = \frac{(T_{o2_{is}} - T_{o1})}{(\tilde{T}_{o2} - T_{o1}) \left(1 - \frac{v_{tipGE} + v_{hubGE}}{h} \right)}, \quad (3.28)$$

Finally, to obtain the stage total pressure rise, $\frac{P_{o2}}{P_{o1}}$:

$$\frac{P_{o2}}{P_{o1}} = \left[\eta \left(\frac{\tilde{T}_{o2}}{T_{o1}} - 1 \right) \left(1 - \frac{v_{tipGE} + v_{hubGE}}{h} \right) + 1 \right]^{\left(\frac{\gamma}{\gamma-1}\right)}. \quad (3.29)$$

The implementation of the meanline model with the correlations for end-wall flow blockage and losses is detailed in Appendix C.

Chapter 4

Meanline Sensitivity Analysis

4.1 Introduction

This chapter presents an analysis of the sensitivity of the third stage performance to geometry variation using the meanline model described in Chapter 3. A quadratic response surface of the meanline results is then constructed and used in a Monte-Carlo analysis. Finally, a probabilistic analysis is performed to identify the key drivers of the uncertainty between the 3-D and the meanline models.

As with the 3-D results, the probabilistic sensitivity analysis results using the meanline simulation show large performance variability due to geometric noise. The largest variation is from the rotor leading edge angle and the second is the rotor tip clearance. This ranking is different from the 3-D simulation results where the rotor tip clearance was the dominant sensitivity. The probabilistic comparison study shows that this difference in trends arises (as one might expect) mostly because of the modeling of the impact of rotor tip clearance on stage performance.

4.2 Results of the Deterministic Sensitivity Analysis using the Meanline Model

In the present section, sensitivity results are observed from a deterministic point of view, but the difference between the 3-D and meanline models is not analyzed in detail. The present purpose is to see if general conclusions, similar to the 3-D simulation sensitivity results, can be drawn. The

sensitivity analysis results are summarized in Table 4.1.

The most sensitive geometric parameter in the meanline model is the rotor leading edge angle with -2.0 points in pressure ratio, -1.7 points in efficiency and +5.6 points in surge margin. This was not the case for the 3-D calculations in which the rotor leading edge angle sensitivities were -0.64, -0.94 and -1.6 points respectively.

Clearances are the second most sensitive geometric parameters. For pressure ratio and efficiency, the tip clearance sensitivity is larger than the hub clearance sensitivity. However, the sensitivities of the increased tip clearance are lower than in the 3-D simulations by a factor of roughly five for the increased tip clearance and less than two for the decreased tip clearance.

Except for the rotor leading angle, the ranking of rotor sensitivities of pressure ratio and efficiency is similar to the 3-D : clearance, maximum thickness, trailing edge angle, leading and trailing edge thickness and finally, chord length.

Cases with varying clearances behave differently than the 3-D results for stalling pressure rise margin. While pressure ratio and efficiency are more sensitive to tip clearance, stalling pressure rise margin is more sensitive to hub clearance. Indeed, doubling the hub clearance costs 4 points in stalling pressure rise margin and only half a point when doubling the tip clearance. The reason for this behavior is that in the increased tip clearance case, the stalling pressure rise $C_{h_{max}}$ decreases ([10, 15]) and the freestream pressure rise decreases by the effect of the increased end-wall boundary layer growth on the AVDR. However, in the increased hub clearance case, $C_{h_{max}}$ decreases (slightly less than in the tip clearance case) but the freestream pressure rise does not vary since the hub end-wall boundary layer is assumed constant.

When the rotor leading edge angle is reduced, pressure ratio and efficiency are decreased but stalling pressure rise margin is increased. This observation can be related to the previous discussion in Section 2.5 about the graphical interpretation of 3-D deterministic sensitivities. Changing the rotor leading edge angle changes the compressor speedline. When the rotor leading angle is decreased by 2.7° , the new operating point on the new speedline is much closer to the choking limit than in the nominal geometry case.

<i>Geometry</i>	<i>Row</i>		$100\frac{\Delta P_o}{P_{o_{in}}}$	$100\Delta\eta$	$100\Delta Mg$
Clearance	R3	Nom \times 2	-1.2 (2)	-1.8 (2)	-0.66
Clearance	S3	Nom \times 2	-0.67 (4)	-1.6 (4)	-4.1 (2)
Clearance	R3	Nom \div 2	0.64 (5)	1.9 (1)	0.87
Clearance	S3	Nom \div 2	0.26	0.64 (7)	2.5 (3)
Chord	R3	+1.45%c	-0.068	-0.059	0.54
Chord	S3	+1.56%c	-0.007	-0.027	0.210
Chord	R3	-1.45%c	0.064	-0.089	-0.666
Chord	S3	-1.56%c	-0.013	-0.028	-0.32
LE Angle	R3	+2.7deg	0.58	0.060	-1.9 (6)
LE Angle	S3	+2.7deg	-0.041	-0.21	0.27
LE Angle	R3	-2.7deg	-2.0 (1)	-1.7 (3)	5.6 (1)
LE Angle	S3	-2.7deg	0.012	0.094	-0.19
TE Angle	R3	+2.7deg	0.38 (8)	-0.99 (5)	-1.37 (8)
TE Angle	S3	+2.7deg	0.039	0.100	0.40
TE Angle	R3	-2.7deg	-0.35 (10)	0.69 (6)	1.2 (10)
TE Angle	S3	-2.7deg	-0.048	-0.14	-0.41
LE Thick.	R3	+0.73%c	-0.52 (7)	-0.50 (9)	1.6 (7)
LE Thick.	S3	+0.78%c	-0.022	-0.091	0.072
LE Thick.	R3	-0.73%c	-0.37 (9)	-0.36	1.2 (8)
LE Thick.	S3	-0.78%c	-0.023	-0.11	0.14
TE Thick.	R3	+0.73%c	-0.10	0.29	1.0
TE Thick.	S3	+0.78%c	0.002	0.004	0.14
TE Thick.	R3	-0.73%c	0.025	-0.32	-0.85
TE Thick.	S3	-0.78%c	-0.014	-0.032	-0.18
Max Thick.	R3	+0.73%c	-0.82 (3)	-0.59 (8)	2.3 (4)
Max Thick.	S3	+0.78%c	-0.078	-0.38 (10)	0.44
Max Thick.	R3	-0.73%c	0.60 (6)	-0.083	-1.9 (5)
Max Thick.	S3	-0.78%c	0.039	0.23	-0.42

Table 4.1: Results of the sensitivity analysis of the 3rd stage with the meanline simulation. Figures in parenthesis are rankings of the ten most important noises. The first column is the varying blade geometry parameter. The second column indicates the row on which the geometry variations have been applied: R3 for rotor and S3 for stator. The third column gives the quantitative value of the deformation. The last three columns are the results of the sensitivity analysis relative to the nominal geometry for total pressure ratio ($\Delta PR = \frac{\Delta P_o}{P_{o_{in}}}$), isentropic efficiency (η) and stalling pressure rise margin (Mg).

4.3 Results of Probabilistic Sensitivity Analysis

4.3.1 All Geometric Parameters have Variability

The quadratic response surface for the meanline model is constructed like the 3-D simulation response surface. The Monte-Carlo analysis uses the same input distributions for the geometric parameters and the same CDF is used for the generation of input clearance distributions. Figures 4-1 and 4-2 give the output PDF and CDF of total pressure ratio, isentropic efficiency and stalling pressure rise margin.

The mean shift results in all three figures are similar to those from the 3-D simulation. Pressure ratio, efficiency, and stalling pressure rise margin mean shift are -0.36, -0.41, and 1.01 points respectively compared to -0.59, -0.45, and 1.4 points for the 3-D. The stalling pressure rise margin mean is one percentage point higher than the nominal. The mean shift in stalling pressure rise margin is due to the positive deterministic sensitivities described in Section 2.5.

Although the meanline distributions have smaller standard deviations than those of the 3-D model, they are still significant. Pressure ratio, efficiency, and stalling pressure rise margin standard deviations are 0.96, 1.8, and 3.0 points, respectively, compared to 1.2, 2.0, and 4.5 points for the latter. The performance variability predicted by the meanline model remains large with a 4σ range of four points in efficiency and pressure ratio. The three points in stalling pressure rise margin standard deviation mean that the meanline model predicts a large stalling pressure rise margin variability due to geometric variability.

The fifth percentile value is approximately 2 points below the nominal for pressure ratio, 2.7 points for efficiency and 3.7 for stalling pressure rise margin. These are, as with the 3-D simulation, large values that could lead to problems in meeting design requirements.

4.3.2 Effect of Individual Geometric Noises on Mean Performance and Variability

As with the 3-D probabilistic sensitivity analysis, a Monte-Carlo analysis was run with the geometric noises removed one at a time. The purpose was to determine the key geometric factors for output performance variability and mean shift. Tables 4.2, 4.3, and 4.4 give the results of this study. Figure 4-3 and 4-4 summarize the ranking of the five most important mean shift and

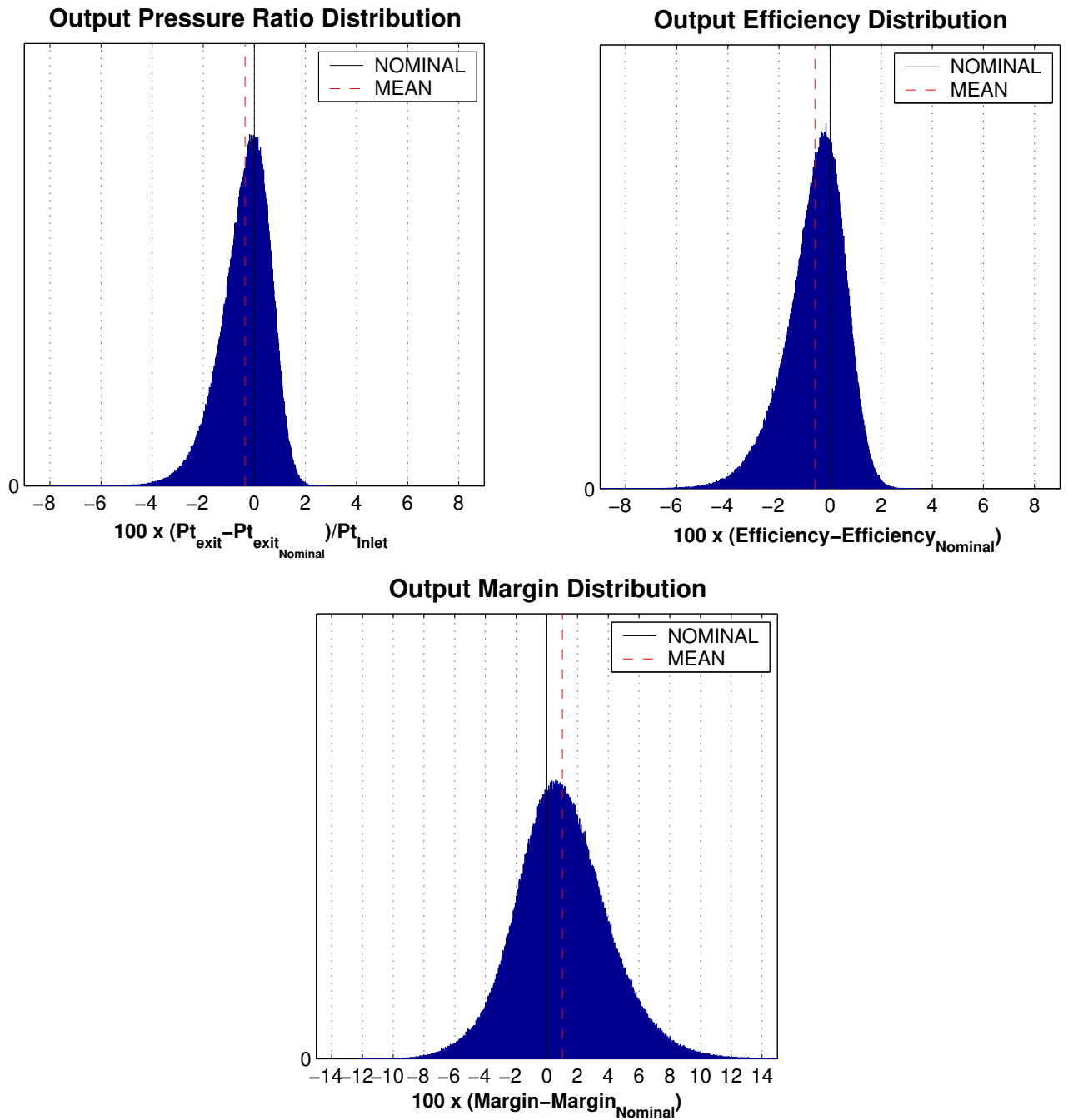


Figure 4-1: Output distributions from the Monte-Carlo analysis using the response surface based on the meanline simulation

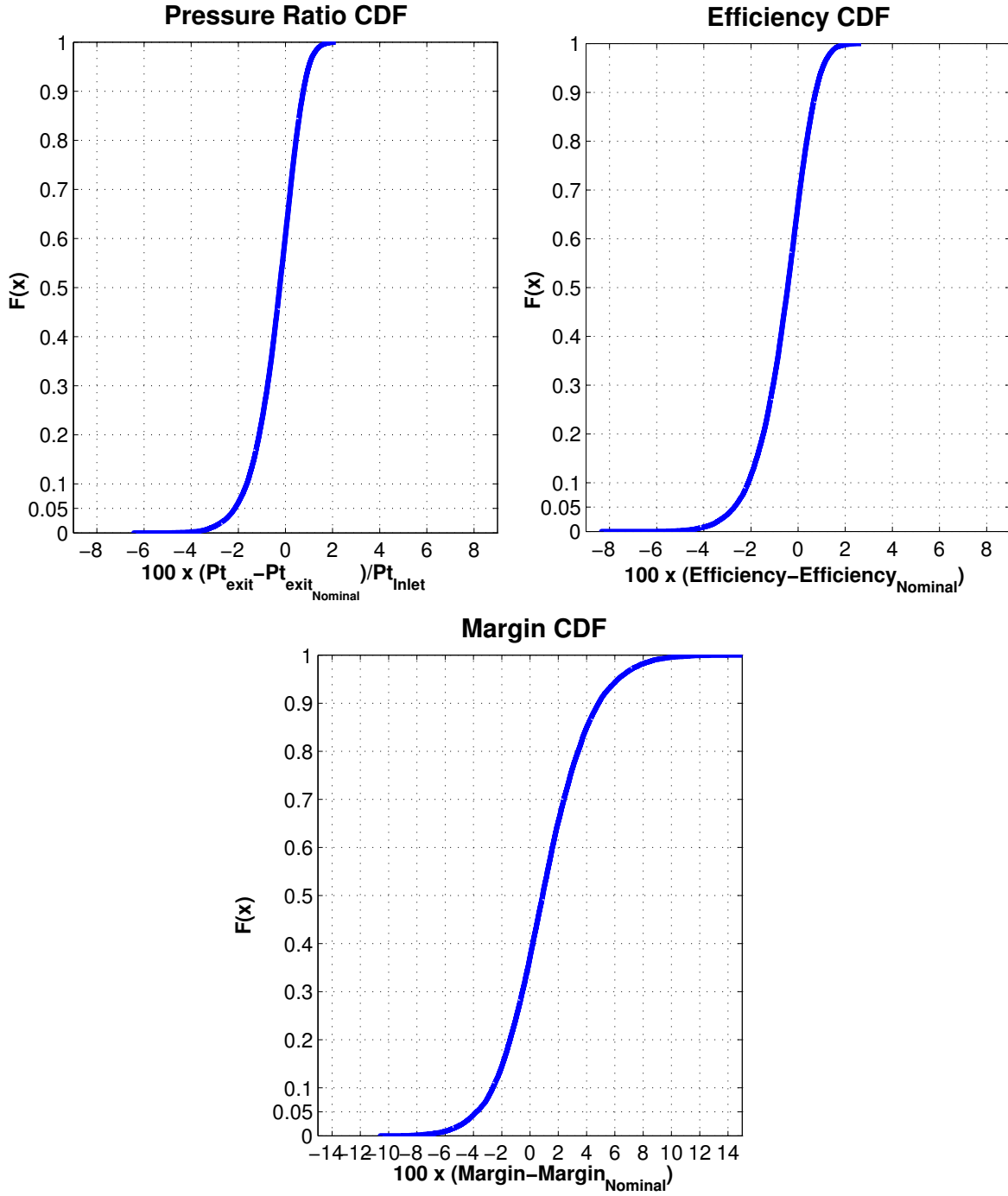


Figure 4-2: Output CDF's from the Monte-Carlo analysis using the response surface based on the meanline simulation

variability factors.

The dominant geometric parameter for most of the output performance metrics is not, as with the 3-D simulation, the rotor clearance, but rather the rotor leading edge angle. In Figures 4-3 and 4-4, rotor leading edge angle (R LEA) is usually first in most of the metrics, whereas for the 3-D, it is ranked second. However, rotor tip clearance (R C), the main noise factor in the 3-D simulation, is also important in the meanline simulation, in particular for the variability of the distribution. Observations are made concerning the mean shift, the standard deviation and the fifth percentile value.

	<i>Row</i>	$100\left(\frac{\overline{P_o}-P_o}{P_{o_{in}}}\right)$	$100(\overline{\eta} - \eta)$	$100(\overline{Mg} - Mg)$
All Applied		-0.36	-0.59	1.0
<i>Var. NOT Applied</i>	<i>Row</i>	$100\left(\frac{(\overline{P_o})_i-\overline{P_o}}{P_{o_{in}}}\right)$	$100(\overline{\eta}_i - \overline{\eta})$	$100(\overline{Mg}_i - \overline{Mg})$
Clearance	R3	0.000	0.020	-0.087 (3)
Clearance	S3	0.019 (4)	0.044 (4)	-0.053 (4)
Chord	R3	0.000	0.022	0.025
Chord	S3	0.003	0.009	0.020
LE Angle	R3	0.18 (1)	0.21 (1)	-0.46 (1)
LE Angle	S3	0.004	0.017	-0.007
TE Angle	R3	-0.003	0.041 (5)	0.026
TE Angle	S3	0.004	0.008	0.002
LE Thick.	R3	0.11 (2)	0.11 (2)	-0.35 (2)
LE Thick.	S3	0.000	0.028	-0.025
TE Thick.	R3	0.010 (5)	0.006	-0.019
TE Thick.	S3	0.004	0.007	0.004
Max Thick.	R3	0.030 (3)	0.088 (3)	-0.049 (5)
Max Thick.	S3	0.006	0.021	0.003

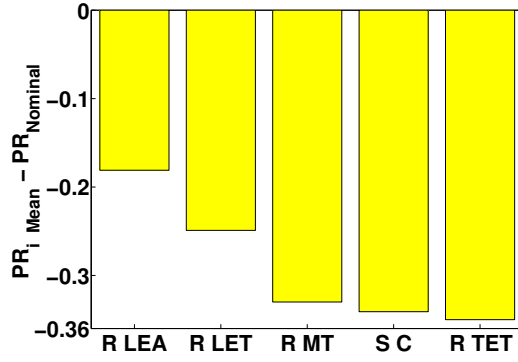
Table 4.2: Mean shift of the Monte-Carlo analysis on the response surface of the meanline simulation. Figures in parenthesis rank the five most important geometric noises.

	<i>Row</i>	$100 \cdot \sigma_{\frac{P_o}{P_{o_{in}}}}$	$100 \cdot \sigma_{\eta}$	$100 \cdot \sigma_{Mg}$
All Applied		0.97	1.2	3.0
<i>Var. NOT Applied</i>	<i>Row</i>	$100 \left[\sigma \left(\frac{P_o}{P_{o_{in}}} \right)_i - \sigma \left(\frac{P_o}{P_{o_{in}}} \right) \right]$	$100(\sigma_{\eta_i} - \sigma_{\eta})$	$100(\sigma_{Mg_i} - \sigma_{Mg})$
Clearance	R3	-0.11 (2)	-0.21 (1)	-0.027
Clearance	S3	-0.028 (4)	-0.15 (2)	-0.51 (1)
Chord	R3	-0.001	-0.001	-0.012
Chord	S3	0.001	-0.001	-0.002
LE Angle	R3	-0.29 (1)	-0.13 (3)	-0.46 (2)
LE Angle	S3	0.001	-0.001	-0.001
TE Angle	R3	-0.016 (5)	-0.081 (4)	-0.064 (4)
TE Angle	S3	0.001	-0.002	-0.009
LE Thick.	R3	-0.012	-0.011	-0.042 (5)
LE Thick.	S3	0.000	-0.001	-0.001
TE Thick.	R3	0.000	-0.010	-0.034
TE Thick.	S3	0.000	-0.001	-0.001
Max Thick.	R3	-0.068 (3)	-0.013 (5)	-0.20 (3)
Max Thick.	S3	0.000	-0.012	0.000

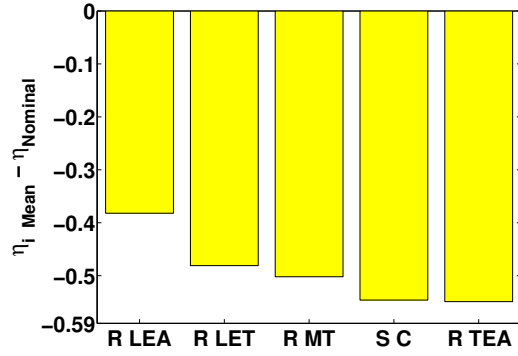
Table 4.3: Standard deviation of the Monte-Carlo analysis on the response surface of the meanline simulation. The Figures in parenthesis rank the five most important geometric noises.

	<i>Row</i>	$100\left(\frac{P_{o5\%}-P_o}{P_{oin}}\right)$	$100(\eta_{5\%}-\eta)$	$100(Mg_{5\%}-Mg)$
All Applied		-2.1	-2.7	-3.7
<i>Var. NOT Applied</i>	<i>Row</i>	$100\left(\frac{(P_{o5\%})_i-P_{o5\%}}{P_{oin}}\right)$	$100(\eta_{5\%_i}-\eta_{5\%})$	$100(Mg_{5\%_i}-Mg_{5\%})$
Clearance	R3	0.18 (2)	0.39 (2)	-0.035
Clearance	S3	0.061 (5)	0.30 (3)	1.1 (1)
Chord	R3	-0.002	0.021	0.043
Chord	S3	0.005	0.011	0.021
LE Angle	R3	0.73 (1)	0.42 (1)	0.30 (2)
LE Angle	S3	0.006	0.020	-0.007
TE Angle	R3	0.016	0.15 (4)	0.16 (5)
TE Angle	S3	0.005	0.012	0.019
LE Thick.	R3	0.13 (3)	0.13 (5)	-0.28 (4)
LE Thick.	S3	0.007	0.027	-0.021
TE Thick.	R3	0.010	0.015	0.040
TE Thick.	S3	0.008	0.008	0.007
Max Thick.	R3	0.12 (4)	0.10	0.28 (3)
Max Thick.	S3	0.011	0.038	0.009

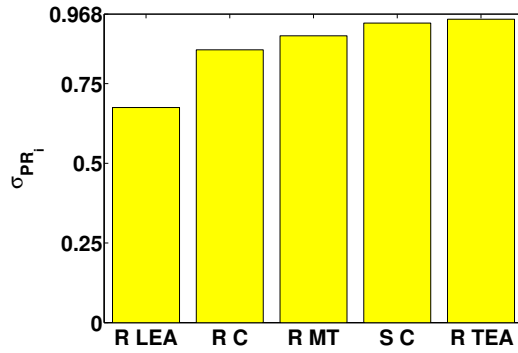
Table 4.4: Fifth percentile value of the Monte-Carlo analysis on the response surface of the meanline simulation. Figures in parenthesis are ranking the five most important geometric noises.



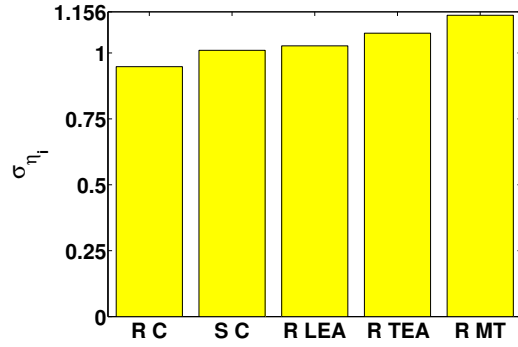
$$(a) 100 \left(\frac{\overline{(P_o)_i} - P_o}{P_{o_{in}}} \right)$$



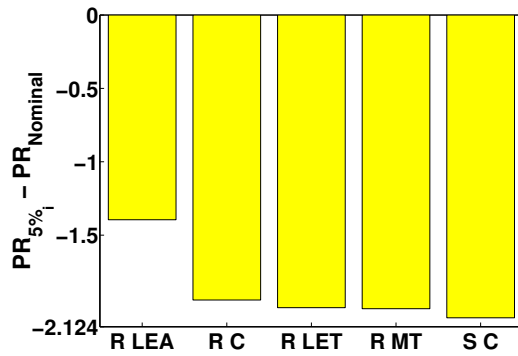
$$(b) 100(\overline{\eta}_i - \eta)$$



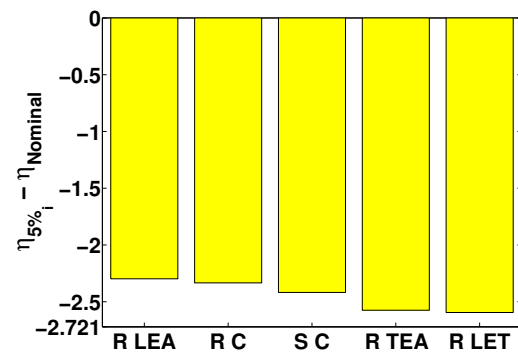
$$(c) 100 \cdot \sigma \left(\frac{P_o}{P_{o_{in}}} \right)_i$$



$$(d) 100 \cdot \sigma_{\eta_i}$$



$$(e) 100 \left(\frac{(P_{o_{5\%}})_i - P_o}{P_{o_{in}}} \right)$$



$$(f) 100(\eta_{5\%_i} - \eta)$$

Figure 4-3: Ranking of the five geometric parameters that most impact the pressure ratio and efficiency distributions. The X-axis gives the parameter which variability is set to zero. R is for rotor, S for stator, C for clearance, LE for leading edge, TE for trailing edge, M for maximum, A for angle, T for thickness and CH for chord.

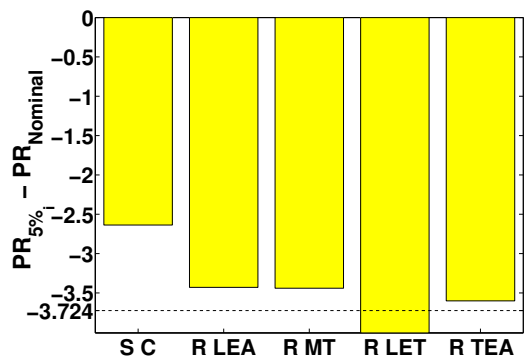
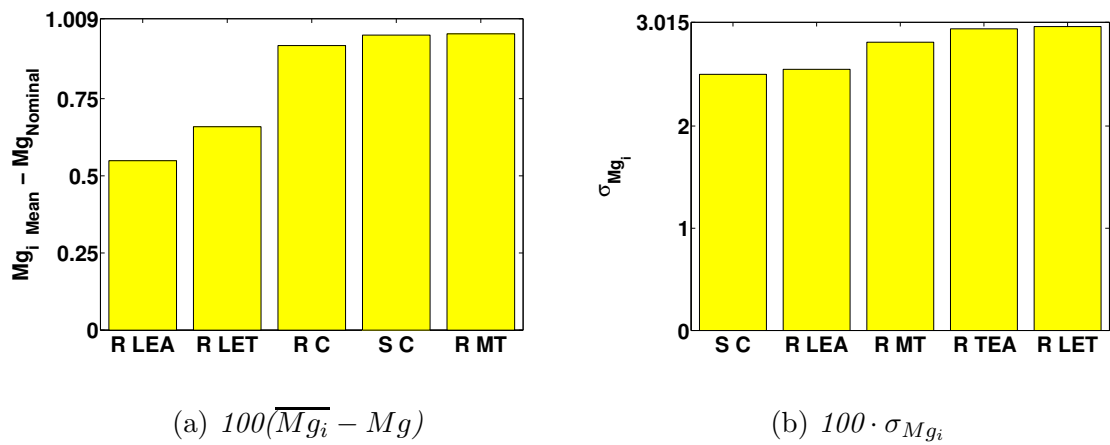


Figure 4-4: Ranking of the five geometric parameter that most impact the stalling pressure rise margin distribution. The X-axis gives the parameter which variability is set to zero. R is for rotor, S for stator, C for clearance, LE for leading edge, TE for trailing edge, M for maximum, A for angle, T for thickness and CH for chord

Mean Shift

Table 4.2, histograms (a) and (b) of Figure 4-3 and histogram (a) of Figure 4-4 give the impact of geometric noise on the performance mean shift. The rotor leading edge angle is observed to play a main role in the mean shift for all the performance metrics. With no rotor leading edge angle noise, pressure ratio, efficiency and stalling pressure rise margin mean shifts are reduced by 50%, 37% and 43% respectively. The second and third most important geometric parameters are the rotor leading edge thickness and maximum thickness.

In summary, compared to the 3-D response surface simulation where rotor tip clearance is the most important contribution to the mean shift in stage performance (see histograms (a),(b) of Figure 4-3), the meanline simulation shows much less mean shift reduction when rotor or stator clearance noise is removed.

Standard Deviation

Table 4.3, histograms (c) and (d) of Figure 4-3 and histogram (b) of Figure 4-4 give the impact of geometric noise on the performance standard deviation. The main factors of performance variability are rotor leading edge angle and the rotor tip clearance. The stator clearance is important as well, in particular for the stalling pressure rise margin where it is ranked second. Rotor tip clearance and leading edge angle account for 18% and 10% respectively of the efficiency standard deviation. The main noise factor for stalling pressure rise margin is stator hub clearance with a 17% reduction of standard deviation followed by rotor leading edge angle with 15% reduction. The standard deviation margin sensitivity to stator hub clearance is related to the deterministic sensitivity of stalling pressure rise margin to stator hub clearance, which reason is explained in Section 4.2. In comparison with the 3-D model, the meanline analysis results of the meanline simulation do not portray the same quantitative importance of the rotor clearance, although rotor clearance and rotor leading edge angle are the most important noise factors in both models.

Fifth Percentile

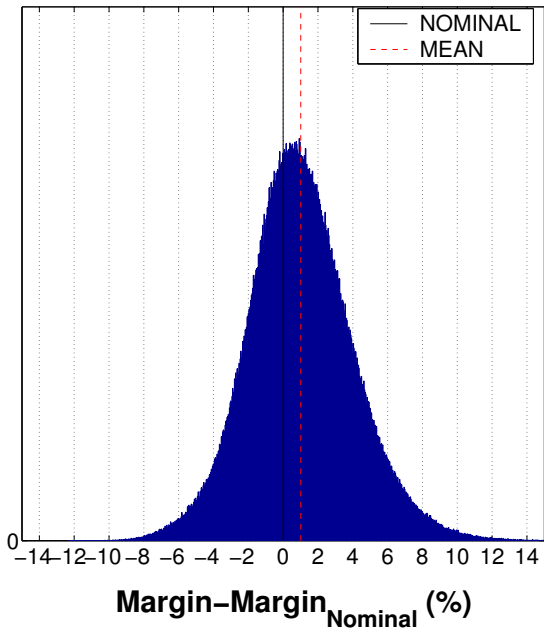
Table 4.4 shows, as in histograms (e) and (f) of Figure 4-3 and histogram (c) of Figure 4-4, the impact of the geometric noise on the fifth percentile value of the performance metrics distributions. The main geometric noises are rotor leading edge angle and rotor tip clearance for pressure ratio

and efficiency. When the rotor leading edge angle noise is removed, a 34% reduction of the fifth percentile distance to nominal pressure ratio is achieved, against 9% for the removal of rotor tip clearance noise. For efficiency, the reductions are 16% and 14% respectively.

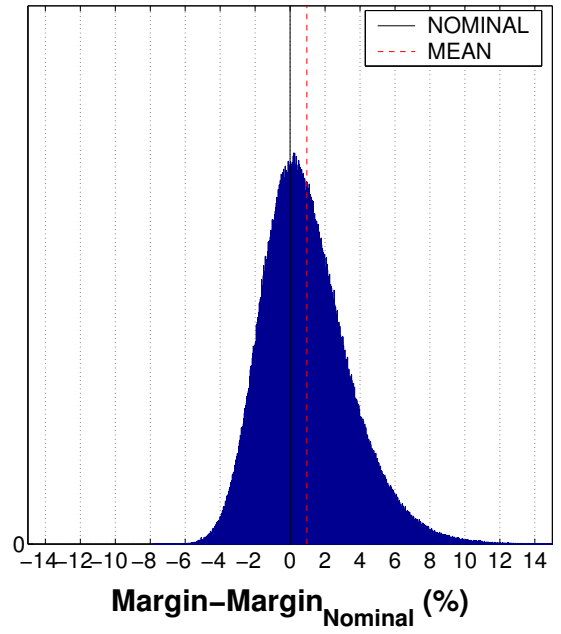
Stalling pressure rise margin is the geometric parameter that most reduces the distance between the fifth percentile value and the nominal value is stator hub clearance. The rotor leading edge angle is ranked second with a reduction of only 8% against 29% for stator clearance. Figure 4-5 gives a graphical explanation of the phenomenon. This case shows the information added by the knowledge of the fifth percentile value. Figure 4-5 b (no stator clearance noise) shows that the reduction of uncertainty mostly influences the lower values of the distribution, removing the left-hand tail. The reduction of stalling pressure rise variability in Figure 4-5 however (no rotor leading edge angle noise), removes the high stalling pressure rise margin population. Even though stator clearance noise and rotor leading edge angle noise have the same impact on stalling pressure rise variability, it appears more useful to reduce stator clearance noise in order to have a population that meets requirement.

Summary

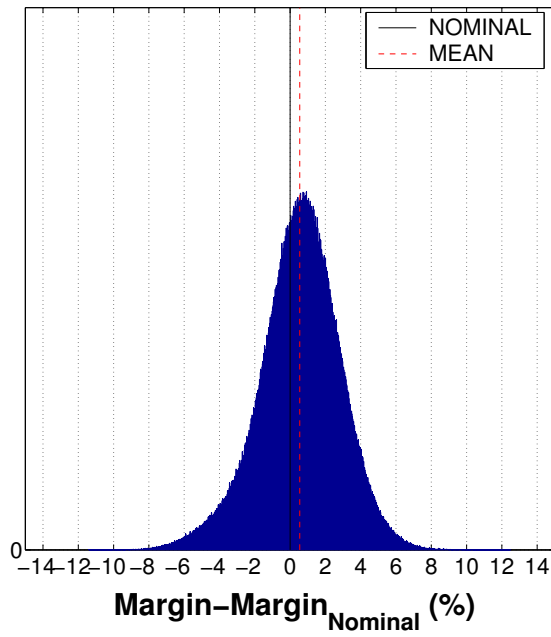
The main geometric contribution to pressure ratio, efficiency and stalling pressure rise margin mean shift and variability are, as in the 3-D rotor leading edge angle and rotor tip clearance. However, the 3-D results attribute more importance to the rotor tip clearance whereas the meanline ranks the rotor leading edge angle first noise factor. The meanline results also indicate that stator clearance, is a major factor in low stalling pressure rise margin stages in the population.



(a) Nominal case



(b) No stator hub clearance noise



(c) No rotor leading edge angle

Figure 4-5: The margin standard deviation reduction.

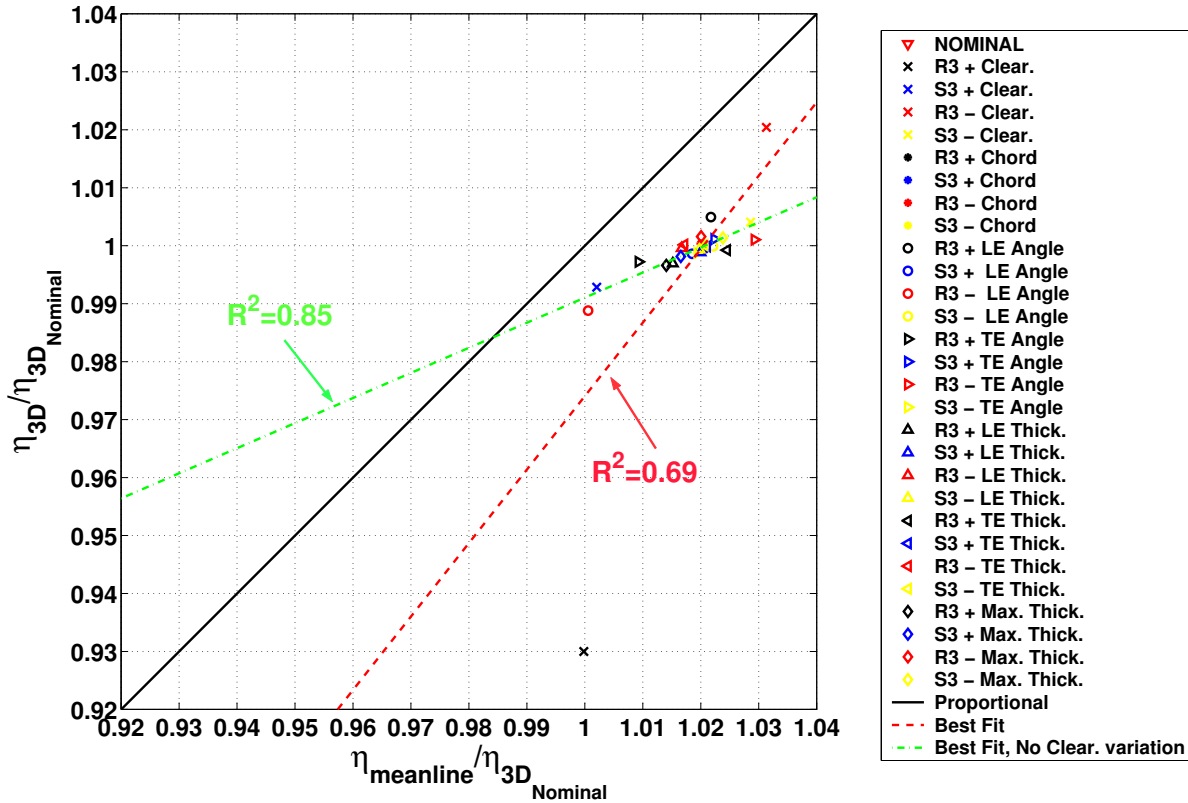


Figure 4-6: Prediction of efficiency for 3-D and meanline models. The value are normalized by the 3-D efficiency at nominal geometry on the operating point

4.4 Comparison of 3-D and Meanline Models

4.4.1 Deterministic Comparison of the 3-D and Meanline Models

The difference between the meanline and the 3-D simulation results is defined as the error. Figure 4-6 plots the meanline and the 3-D simulation efficiency for all cases. Since all the points are below the proportionality line, the meanline overpredicts efficiency for all the cases. The biggest error in the meanline model is in the prediction of the effect of rotor tip clearance on the efficiency compared to the 3-D simulation. In particular, the case where the rotor tip clearance is doubled shows a larger distance to the proportionality line compared to the other cases.

A best fit of the data is built with all the cases (dashed line). This best fit line and the proportionality lines have similar directions, which shows the general trends are similar. However, the best fit line is not parallel to the proportionality line, indicating that the quantitative trends

in both models are different. Additionally, R^2 of the best fit regression is only 0.69, indicating the best fit line models the actual trends with poor confidence. If only the nominal clearance cases are taken for the regression (dot and dashed line), the trends are less similar, but the confidence is larger with $R^2 = 0.85$.

4.4.2 Probabilistic Comparison of the 3-D and Meanline Models

A probabilistic comparison of the two models has been made using a quadratic response surface based on the error between them :

$$\epsilon = f^{3D} - f^m = \sum_{j=1}^N a_j^\epsilon x_j^2 + \sum_{j=1}^N b_j^\epsilon x_j + c^\epsilon, \quad (4.1)$$

where f^{3D} and f^m are

$$f^{3D} = \sum_{j=1}^N a_j^{3D} x_j^2 + \sum_{j=1}^N b_j^{3D} x_j + c^{3D}, \quad (4.2)$$

$$f^m = \sum_{j=1}^N a_j^m x_j^2 + \sum_{j=1}^N b_j^m x_j + c^m. \quad (4.3)$$

Figure 4-7 shows the error distributions of pressure ratio, efficiency and stalling pressure rise margin that result from a Monte-Carlo analysis. The mean error measures the average offset of the meanline from the 3-D simulation while the standard deviation quantifies the uncertainty of the difference between the models. We find that : that

1. The mean error of efficiency is -1.5 points, closer to zero than the nominal error.
2. The standard deviation error of efficiency is about 1.1 points.

This means that the meanline model efficiency departs from the the 3-D results by 1.5 ± 2.2 points, on average. This information cannot be extracted easily from a deterministic study of the error. The large confidence interval indicates the trends of the two models are quantitatively different.

We can also set the noise of each geometric parameter to zero to determine the key contributions to the error standard deviation. Tables 4.5 and 4.6 and Figure 4-8 give the results of this study. The main conclusion is the role of rotor tip clearance variability on the difference in trends between the meanline and the 3-D models. When the rotor tip clearance noise is removed, the standard

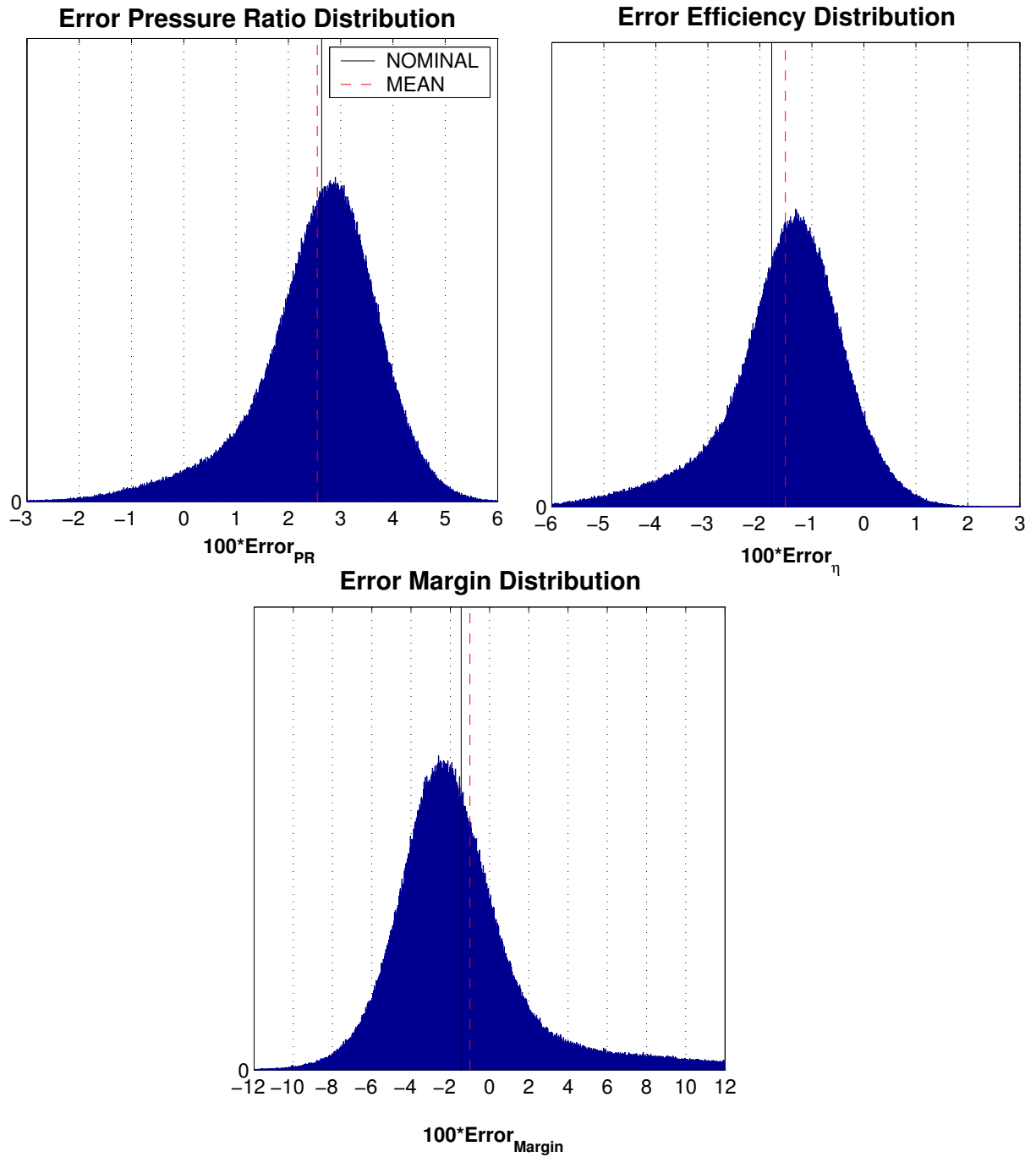


Figure 4-7: Output distribution from the Monte-Carlo analysis on the response surface from the meanline sensitivity analysis

deviation of pressure ratio error is reduced by 49% and the standard deviation of efficiency error by 48%, so the confidence interval of the efficiency predicted by the meanline is divided by two. Taking the changed mean shift into account, it would become 1.3 ± 1.2 points above the 3-D results on average, which is a significant improvement.

In summary, the impact of rotor tip clearance on performance is much more important in the 3-D calculations than in the meanline simulation used in this thesis. The absence of noise in rotor tip clearance noise halves the standard deviation of all performance metrics error.

Table 4.5: Mean shift of the Monte-Carlo analysis on the response surface of the meanline model error.

<i>Var. NOT Applied</i>	<i>Row</i>	$100 \cdot \bar{\epsilon} \left(\frac{P_o}{P_{o_{in}}} \right)$	$100 \cdot \bar{\epsilon}_\eta$	$100 \cdot \bar{\epsilon}_{Mg}$
All Applied		2.555	-1.508	-1.013
<i>Var. NOT Applied</i>	<i>Row</i>	$100 \left[\bar{\epsilon} \left(\frac{P_o}{P_{o_{in}}} \right)_i - \bar{\epsilon} \left(\frac{P_o}{P_{o_{in}}} \right) \right]$	$100(\bar{\epsilon}_{\eta_i} - \bar{\epsilon}_\eta)$	$100(\bar{\epsilon}_{Mg_i} - \bar{\epsilon}_{Mg})$
Clearance	R3	0.264 (1)	0.242 (1)	-0.932 (1)
Clearance	S3	-0.011 (5)	-0.050	0.017
Chord	R3	0.002	-0.018	-0.013
Chord	S3	0.030	-0.137 (3)	-0.022 (5)
LE Angle	R3	-0.136 (2)	-0.144 (2)	0.359 (2)
LE Angle	S3	0.001	-0.001	-0.004
TE Angle	R3	0.024 (4)	-0.020	-0.078 (4)
TE Angle	S3	-0.002	-0.002	-0.008
LE Thick.	R3	-0.085 (3)	-0.071 (4)	0.278 (3)
LE Thick.	S3	0.004	-0.006	0.011
TE Thick.	R3	-0.001	0.000	-0.001
TE Thick.	S3	-0.003	-0.004	-0.007
Max Thick.	R3	-0.006	-0.064 (5)	-0.004
Max Thick.	S3	-0.001	-0.002	0.000

Table 4.6: Standard deviation of the Monte-Carlo analysis on the response surface of the meanline model error.

<i>Var. NOT Applied</i>	<i>Row</i>	$100 \cdot \sigma_{\epsilon} \left(\frac{P_o}{P_{o_{in}}} \right)$	$100 \cdot \sigma_{\epsilon_{\eta}}$	$100 \cdot \sigma_{\epsilon_{Mg}}$
All Applied		1.197	1.149	4.812
<i>Var. NOT Applied</i>	<i>Row</i>	$100 \left[\sigma_{\epsilon} \left(\frac{P_o}{P_{o_{in}}} \right)_i - \sigma_{\epsilon} \left(\frac{P_o}{P_{o_{in}}} \right)_j \right]$	$100(\sigma_{\epsilon_{\eta_i}} - \sigma_{\epsilon_{\eta_j}})$	$100(\sigma_{\epsilon_{Mg_i}} - \sigma_{\epsilon_{Mg_j}})$
Clearance	R3	-0.590 (1)	-0.558 (1)	-3.031 (1)
Clearance	S3	0.029 (3)	0.040 (2)	-0.044 (4)
hline Chord	R3	0.001	0.001	-0.006
Chord	S3	0.000	-0.016 (5)	0.004
LE Angle	R3	-0.089 (2)	-0.021 (3)	-0.181 (2)
LE Angle	S3	0.003	0.001	0.006
TE Angle	R3	-0.025 (4)	-0.020 (4)	0.078 (3)
TE Angle	S3	0.003	0.002	0.004
LE Thick.	R3	-0.005	-0.005	-0.023 (5)
LE Thick.	S3	0.004	0.003	0.007
TE Thick.	R3	0.000	-0.011	0.013
TE Thick.	S3	0.003	0.002	0.009
Max Thick.	R3	-0.020 (5)	-0.003	-0.004
Max Thick.	S3	0.0004	-0.002	0.013

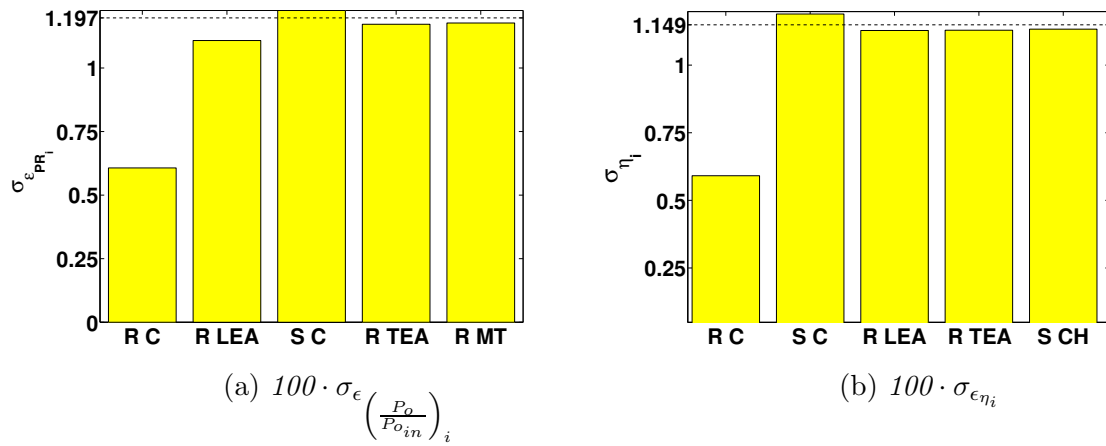


Figure 4-8: Ranking of the five geometric parameter that most impact the standard deviation error. The X-axis gives the parameter which uncertainty is set to zero. R is for rotor, S for stator, LE for leading edge, TE for trailing edge, M for maximum, A for angle, T for thickness, CH for chord

Chapter 5

Summary and Conclusions

5.1 Thesis Summary

The impact of blade geometry variation on a compressor stage has been assessed deterministically and probabilistically, using both a 3-D simulation and a meanline model based on repeating stages.

A deterministic analysis of the sensitivity (to geometric variation) of the third stage performance for the CREATE compressor has been conducted using the 3-D-RANS solver Euranus from NUMECA. Geometry changes were applied to clearance, chord, leading and trailing edge angle and thickness, and maximum thickness based on manufacturing tolerances. The impacts of these geometric variations on stage pressure ratio, efficiency and stalling pressure rise margin were analyzed.

The strongest sensitivity was found to be to rotor tip clearance. The second most sensitive effect was found to be rotor leading edge parameters.

The probabilistic sensitivity analysis was conducted using a response surface. The impact of blade geometric noise due to manufacturing on stage performance was assessed. For the input variability, the mean efficiency was found to be approximately a half point below the nominal efficiency, with most of this shift attributable to rotor tip clearance. The standard deviation in efficiency was 2 points, with 75% of the variability due to rotor tip clearance.

A meanline simulation for repeating stages that accounts for end-wall flow losses and blockage has been developed. The meanline simulation used the quasi-3-D solver MISES for the freestream flow and was coupled with end-wall correlations for repeating stages [10, 11, 15]. A empirical

modification, based on the 3-D simulations, accounts for end-wall flow blockage behavior within the stage. For the case of interest, if this effect is not taken into account, a substantial difference exists for the pressure rise and efficiency compared to the 3-D analysis.

A deterministic sensitivity analysis was conducted with the meanline model. It was found that the main performance sensitivities were due to rotor leading edge angle and rotor tip clearance, in that order.

A probabilistic analysis was also conducted with the meanline model again using a response surface. This showed similar mean shift trends to that of the 3-D response surface simulation, but the pressure ratio and efficiency standard deviations were approximately half those of the 3-D analysis. The main factor of performance mean shift was rotor leading edge angle thickness and the main factors of performance variability were rotor tip clearance and rotor leading edge angle. A comparison of the meanline and 3-D model results was conducted and showed differences in trends. The difference between the two models was defined as error. The main driver of the error variability was the rotor tip clearance which accounts for half of the variability.

5.2 Recommendations for Future Work

1. Develop an end-wall model that improves the estimation of blockage behavior within a stage and is suitable for use in a probabilistic framework. This is the most important work task for the future.
2. Assess the 3-D calculations accuracy using other 3-D solvers with the same geometry or using existing 3-D results for similar geometries. In particular, investigate trends in rotor/stator blockage behavior.
3. Investigate what determines the peak pressure rise on a row basis. This work may help to resolve the issue of the discrepancy in the calculation of $C_{h_{max}}$ for the 3-D simulation and for the correlation.
4. Create a simple end-wall model to explain the physical mechanism underlying the rotor/stator blockage behavior found in the 3-D calculations.
5. Run a complete probabilistic analysis of a stage using the meanline model without building

a response surface. It would be possible to run a Monte-Carlo analysis following Garzon's [5] work for the geometry blade creation since a single run computation time for a stage is about 2-5 minutes. An estimated time for a 5000 run Monte-Carlo analysis is about a week. As this analysis would take the cross-effects into account, conclusions about the importance of these effects could be drawn by comparing the current results with the response surfaces results.

Appendix A

Meanline Analysis without endwalls on CREATE Compressor Using MISES

A.1 Introduction

The first task of this research was to run a meanline analysis on the CREATE compressor without end-walls. This was done using the quasi-3D code MISES created by Pr. Drela at the ACDL. MISES is a code based on the fully coupled viscous/inviscid method, using the steady Euler equations and integral boundary layer equations solved with a Newton-Raphson technique. [18].

As MISES can only be run on a single row, the task was to create an interface capable of matching the 6 rows of the compressor. This interface is only applicable when no one of the 6 rows is choked. This is due to the fact that boundary conditions are set at the inlet of each row. Therefore, there is no possibility to set a back pressure on any row.

MATLAB was used to prepare the geometry data given by SNECMA to be readable by MISES and FORTRAN77 codes were added to the source directory of MISES under /src to make the interface easier to run. However, the interface was built on top of the previous version of MISES so that all the previous programs can be still used the way they were, our interface just automates the process. The interface was written for a 6 rows compressor. However, the fact that it was built on top prevents from making major changes when run on more or less rows. The compressor case

was run via a script `run_comp.sh` that launched every single Fortran program.

A.2 Creating the Geometry for MISES

The geometry given by SNECMA was in the form of 3D blade geometry files consisting in 13 constant radial sections in XYZ coordinates. These files are used for the 3D runs on NUMECA and have a special format. The XYZ coordinates are defined as the following : X being the pitch coordinate, Y radial coordinate (span) and Z the axial coordinate (rotation axis of the compressor). For the meanline analysis, it is necessary to cut the blades and transform them into a format that MISES can read.

As MISES works on a row basis, it is also necessary to create some files that indicate to MISES how to transmit the information from one row to another. In particular, for each row, the knowledge of the inlet and outlet mixing planes location is needed. A description of the whole process is detailed in Figure A-4.

A.2.1 The Meanline Analysis

The analysis is achieved on the meanline which radius $r_{meanline}$ is defined

$$\frac{r_{meanline}^2 - r_{min}^2}{r_{max}^2 - r_{min}^2} = \frac{1}{2}. \quad (\text{A.1})$$

It is necessary to cut the blade along this streamsurface in order to run MISES. Using a 3D geometry file `blade3D.xxx` created by the matlab executable `Transcoord.m`, the Fortran program, `Streamcut_comp.f`, cuts the blade on the particular surface defined by the equation A.1 (see details in Appendix, Fig.A-4) The thickness b of the streamtube is taken equal to the actual geometric flow path height such that,

$$b = r_{max} - r_{min} = r_{tip} - r_{hub}. \quad (\text{A.2})$$

A.2.2 The m' θ Coordinates

Before running MISES, it is nessecary to present the coordinates system the code uses. As detailed in the MISES Manual [4] (Section 2), MISES uses the m' θ coordinates (see Figure A-2).

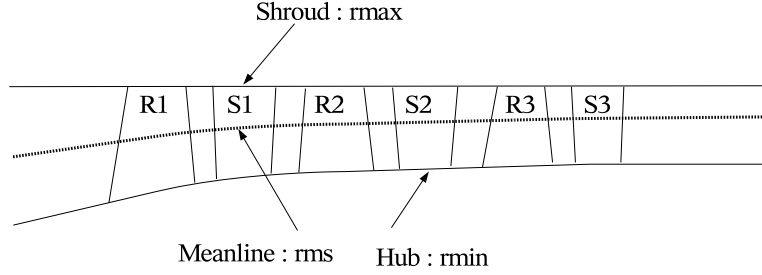


Figure A-1: The Meanline Analysis

The m' coordinates are defined by the integral

$$m' = \int \frac{dm}{r} = \int \frac{\sqrt{dr^2 + dz^2}}{r} \quad (\text{A.3})$$

while θ is the circumferential angle.

The streamline file **stream.xxx** and the blade geometry **blade.xxx** have to be in the $m' - \theta$ coordinates to be readable by MISES. In the present case, since for each row $m' = 0$ represents the leading edge of the blade, it is necessary to generate a **stream.xxx** file for each row -this is done via the matlab program **Streamfile_all.m**. The process is the following : starting from the leading edge at $m' = 0$, for a point $(r_i, z_i(r_i), b_i(r_i))$, the m'_i point is calculated with a trapezoidal integration, i can be positive and negative,

$$m'_i = m'_{i-1} + \frac{2}{r_i + r_{i-1}} \sqrt{(r_i - r_{i-1})^2 + (z_i - z_{i-1})^2}. \quad (\text{A.4})$$

Stream.xxx is then stored in the following format $(m'_i, z_i(m'_i), b_i(m'_i))$ which is readable by MISES. The transformation of the blade geometry to the $m' - \theta$ coordinates is done by **Streamcut_comp.f**. The format of the **blade.xxx** file is then (m'_i, θ_i) .

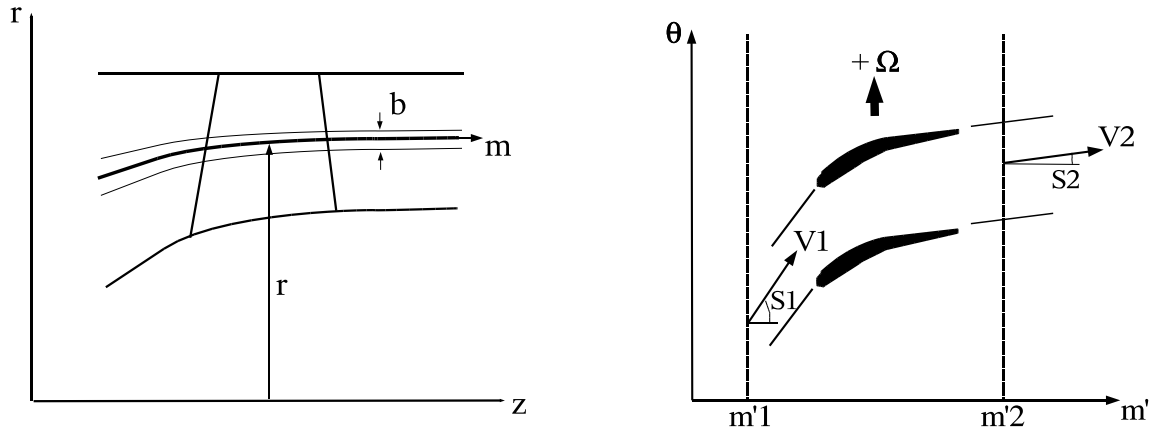


Figure A-2: The Streamline coordinates $m' \theta$

A.2.3 The `XinXout.CREATE` and `interstream.CREATE` files

The `XinXout.CREATE` and `interstream.CREATE` files are necessary to run MISES on the compressor because they contain the location of the mixing planes for each row in the $X - Z$ and $m' - \theta$ coordinates.

They are created by the matlab program `intersect_project.m`. Splines are used to find the intersection of the leading and trailing edge (LE/TE) of each blade with the meanline. The mixing "point" is then located on the meanline at 50% of the distance between the leading and trailing edge. For the first row, the point where the inlet conditions are set is not on the inlet plane at $Z = -48mm$ but on a plane given by SNECMA which is close to the leading edge of the first rotor. The intersection of the meanline and this plane gives the inlet point at $X = 235.41mm$, $Z = -1.315mm$.

The `interstream.CREATE` is read when the distance between leading, trailing edges or mixing planes are needed in the XYZ coordinate system. This is useful for instance for the calculation of the axial spacing between row used in the end-wall correlation, but the file this is not read when not using the correlations. The file has the following format, all the distance are normalized by $l_{ref} = 259.1mm$,

- $(Z, X, b)_{inlet}$
- $(Z, X, b)_{inlet_{R1}}$

- $(Z, X, b)_{LE_{R1}}$
- $(Z, X, b)_{TE_{R1}}$
- $(Z, X, b)_{Mixing\ plane1}$
- $(Z, X, b)_{LE_{S1}}$
- $(Z, X, b)_{TE_{S1}}$
- $(Z, X, b)_{Mixing\ plane2}$
- ...
- $(Z, X, b)_{Mixing\ plane5}$
- $(Z, X, b)_{LE_{S3}}$
- $(Z, X, b)_{TE_{S3}}$
- $(Z, X, b)_{Outlet}$.

By storing the location of the mixing planes for each row, the **XinXout.CREATE** file is essential to the multiple stages run with MISES. In particular, the file is used to write the quantities Xin and $Xout$ in the **ises.xxx** file using the program **interblade.f** . Xin is the inlet-condition location $m'1$ in m' coordinates (see Fig.A-2), thus, Xin is always negative. Similarly, Xin is the outlet-condition location $m'2$. The file is written as the vector

- $(Xin)_{R1}$
- $(Xout)_{R1}$
- $(Xin)_{S1}$
- ...
- $(Xin)_{S3}$
- $(Xout)_{S3}$.

A.3 Inlet and first row initialization

MISES uses non-dimensional quantities on a single row. To be able to run MISES using dimensional input and output for the whole compressor, it is necessary to initialize the quantities at the inlet of the first row and to therefore calculate the quantities that are used to normalize all MISES quantities.

MISES defines the "absolute" total quantities ρ_{o_a}, a_{o_a} (respectively rotation corrected stagnation density and speed of sound) as reference so that $\rho_{o_a} = 1$ and $a_{o_a} = 1$ by definition. There are not to be confused with *absolute-frame* total quantities in the sense that it implies an isentropic process where the fluid is brought to rest in the relative frame, and taken to the rotation center $r = 0$ (cf MISES Manual [4] Section 2).

For a non-dimensional quantity in the relative frame notated X , the dimensional value will be written \bar{X} and the absolute-frame total quantity $X_{o_{abs}}$. X_1 is the inlet quantity and X_2 is the outlet quantity.

The inlet dimensional quantities known at the inlet are in the **inlet_R1.dat** file :

- $\bar{T}_{o_{1_{abs}}}$
- $\bar{P}_{o_{1_{abs}}}$
- $M_{1_{abs}}$
- $\beta_{1_{abs}}$

A.3.1 Velocity

As pressure and temperature are calculated as ratio by the **iprint** file, it is only necessary to calculate the dimensional quantity used by MISES to normalize all the velocities, which is \bar{a}_{o_a} . The following non-dimensional quantities are calculable with the **iprint** file from MISES package,

$$a_1 = \sqrt{\frac{\gamma \cdot P_1}{\rho_1}} \quad a_2 = \sqrt{\frac{\gamma \cdot P_2}{\rho_2}} \quad (\text{A.5})$$

and

$$a_{o_1} = a_1 \cdot \sqrt{1 + \frac{\gamma - 1}{2} \cdot M_1^2} \quad a_{o_2} = a_2 \cdot \sqrt{1 + \frac{\gamma - 1}{2} \cdot M_2^2}. \quad (\text{A.6})$$

The inlet quantities enable us to calculate

$$\bar{a}_{o_1} = A = \bar{a}_{o_{1_{abs}}} \cdot \sqrt{\frac{1 + \frac{\gamma - 1}{2} \cdot M_1^2}{1 + \frac{\gamma - 1}{2} \cdot M_{1_{abs}}^2}}, \quad \text{with} \quad \bar{a}_{o_{1_{abs}}} = \sqrt{\gamma \cdot r \cdot \bar{T}_{T_{1_{abs}}}}. \quad (\text{A.7})$$

Then, the ratio

$$\frac{\bar{a}_{o_1}}{a_{o_1}} = \bar{A}00 = \bar{a}_{o_a} \quad (m/s) \quad (\text{A.8})$$

is defined as the reference velocity $\bar{A}00$ for all dimensional velocities in the future.

A.3.2 Wheel Rotation Speed

MISES is always in the relative frame. To be able to have absolute values out of MISES, it is required to give MISES a wheel rotation speed quantity *ROTREL*. It has to be entered in the **stream.xxx** file and is defined as

$$ROTREL = \frac{\Omega \cdot L_{ref}}{\bar{a}_{o_1}}. \quad (A.9)$$

ROTREL is now calculable since \bar{a}_{o_1} is known, $L_{ref} = 259.1$ mm and $\Omega = -1208.8$ rad/s.

A.3.3 Temperature

As the ratio $\frac{h_{o_2_{abs}}}{h_{o_1_{abs}}}$ is known from the **iprint** file, the absolute total temperature at the exit can be found :

$$\bar{T}_{o_2_{abs}} = \frac{h_{o_2_{abs}}}{h_{o_1_{abs}}} \cdot \bar{T}_{o_1_{abs}}. \quad (A.10)$$

A.3.4 Pressure

The dimensional absolute total pressure at the exit of the first row is now researched. As

$$\frac{P_{o_1_{abs}}}{P_{o_1}} = \left(\frac{T_{o_1_{abs}}}{T_{o_1}} \right)^{\frac{\gamma}{\gamma-1}} = \left(\frac{h_{o_1_{abs}}}{h_{o_1}} \right)^{\frac{\gamma}{\gamma-1}}, \quad \frac{P_{o_2_{abs}}}{P_{o_2}} = \left(\frac{T_{o_2_{abs}}}{T_{o_1}} \right)^{\frac{\gamma}{\gamma-1}} = \left(\frac{h_{o_2_{abs}}}{h_{o_2}} \right)^{\frac{\gamma}{\gamma-1}}, \quad (A.11)$$

a quantity *PSTRATA* can be defined such that

$$PSTRATA = \frac{P_{o_2_{abs}}}{P_{o_1_{abs}}} = \frac{P_{o_2}}{P_{o_1}} \cdot \left[\frac{h_{o_1}}{h_{o_2}} \cdot \frac{h_{o_2_{abs}}}{h_{o_1_{abs}}} \right]^{\frac{\gamma}{\gamma-1}}, \quad (A.12)$$

where all the ratios, $\frac{P_{o_2}}{P_{o_1}}, \frac{h_{o_2}}{h_{o_1}}, \frac{h_{o_2_{abs}}}{h_{o_1_{abs}}}$ are directly known from the **iprint** file. Finally,

$$\bar{P}_{o_2_{abs}} = PSTRATA \cdot \bar{P}_{o_1_{abs}}. \quad (A.13)$$

A.3.5 Reynolds Number

For MISES to solve the flow on the first row, the **ises.xxx** file needs the Reynolds Number defined as the following :

$$Re = \frac{\rho \cdot V \cdot L_{ref}}{\mu}, \quad (\text{A.14})$$

The Sutherland law is used to calculate the dynamic viscosity [16] :

$$\mu = \mu_o \cdot \left(\frac{T}{T_o}\right)^{3/2} \cdot \frac{S + T_o}{S + T} \quad (\text{A.15})$$

with $T_o = 273.2\text{K}$, $S = 111\text{K}$ and $\mu = 1.71 \times 10^{-5}$ kg/ms for air.

The **inlet_R1.dat** file gives all the quantities needed to calculate V and ρ , and $L_{ref} = 259.1$ mm by definition.

A.3.6 The output file out.xxx

To be able to transmit flow information from one row to another and, therefore, march down the compressor, it becomes necessary, considering the structure of MISES code to write a file where all the necessary quantities are stored. This file is called **out.xxx** and is created by the program **iprint**, **out.xxx** can be considered as a mixing plane values storage. All the quantities in **out.xxx** are *absolute-frame* quantities. The file pattern is the following for out.R1xx written by **iprint_trans_init.f** :

- r_2 (m)
- $\bar{V}_{x_1} = V_{x_1} \cdot \bar{A}00$ (m/s)
- $\bar{V}_{x_2} = V_{x_2} \cdot \bar{A}00$ (m/s)
- $M_{2_{abs}}$
- $\beta_{2_{abs}}$ (deg)
- $a_{o2_{abs}} = RA_{S100}$
- $\bar{a}_{o1_{abs}} = a_{o1_{abs}} \cdot \bar{A}00$ (m/s)
- $\bar{a}_{o2_{abs}} = a_{o2_{abs}} \cdot \bar{A}00$ (m/s)
- $\bar{A}00$ (m/s)
- $\bar{P}_{o2_{abs}} = PSTRATA \cdot \bar{P}_{o1_{abs}}$ (Pa)

- $\bar{T}_{o2_{abs}} = \frac{h_{o2_{abs}}}{h_{o1_{abs}}} \cdot \bar{T}_{o1_{abs}}$ (K)
- ω

The RA term is explained later when describing the process of marching down the compressor.

A.4 Row to Row Information Transmission

A.4.1 The `interblade.f` File

Interblade.f reads the exit quantities of the previous row in order to march down the compressor and to propagate the information to the next row (see details in Fig.A-5).

If the previous row is a rotor, absolute quantities are needed to enter the inlet quantities of the stator. **Interblade.f** reads the **out.Rxx** file and write the inlet quantities in **ises.Syy** and **iset.Syy**. If the previous row is a stator, relative quantities are needed to enter the inlet quantities of the rotor. **Interblade.f** reads the **outrel.Sxx** created by **triangle.f** (see Section A.4.3) and writes in **ises.Ryy** and **iset.Ryy**.

The quantities stored by **iprint_mix** in **out.xxx** are all mixed-out quantities. **Interblade.f** has a similar function than a mixing plane.

The quantities read from the previous row are : $M_{rel/abs}$, V_x , $\beta_{rel/abs}$, $\bar{P}_{o_{abs}}$ and $\bar{T}_{o_{abs}}$. These quantities enables to calculate the Reynolds number for the **ises.xxx** file. **Interblade.f** also read the mixing planes location X_{in} and X_{out} from the **XinXoutCREATE00.dat** file and write them in the **ises.xxx** file as well.

A.4.2 From Rotor to Stator

Initialization of Stator Inlet Conditions

To initialize the stator calculation, MISES needs the inlet flow conditions : M_{abs} , $\beta_{1_{abs}}$ and Re . As described previously, these quantities are directly readable -using **interblade.f**- from the file **out.xxx** of the precedent rotor (see Section A.3.6) since the quantities in this file are in the absolute frame:

$$(X_{1_{abs}})_{stator} = (X_{2_{abs}})_{previous.rotor} \quad \text{with } X = M, V_x, \beta, \bar{P}_o \text{ or } \bar{T}_o \quad (\text{A.16})$$

Post-processing the Stator Quantities

Quantities out of MISES are non-dimensional. The **iprint** execution and the **out.xxx** file from the previous rotor enables to have easily access to the exit dimensional pressure and temperature of the stator using the ratio $\frac{h_{o2_{abs}}}{h_{o1_{abs}}}$ and *PSTRATA*. However, it is less trivial to calculate the dimensional velocities. As for the first rotor, the velocity normalization is that $a_{o_a} = 1$ by definition. However, in the stator case,

$$(\bar{a}_{o_a})_{stator} = (\bar{a}_{o_{1_{abs}}})_{stator} = (\bar{a}_{o_{2_{abs}}})_{previous.rotor} . \quad (\text{A.17})$$

The *RA* quantity written in the **out.xxx** file of the previous rotor (see Section A.3.6) can now be explained and used. *RA* is defined such that, for a given row,

$$(RA)_{row} = \frac{(\bar{a}_{o_a})_{row}}{(\bar{a}_{o_a})_{inlet}} = \frac{(\bar{a}_{o_a})_{row}}{A00} . \quad (\text{A.18})$$

In the first stator case, using Equation A.17, *RA* becomes

$$(RA)_{stator1} = \frac{(\bar{a}_{o_a})_{stator}}{(\bar{a}_{o_a})_{inlet}} = \frac{(\bar{a}_{o_{2_{abs}}})_{rotor1}}{(\bar{a}_{o_a})_{rotor1}} = (a_{o_{2_{abs}}})_{rotor1} \quad (\text{A.19})$$

which is how *RA* is calculated in the out.R1xx in the Section A.3.6. For the following rows, *RA* will be calculated such that the equation A.18 is always true by definition, with *A00* constant. For a given row, $A00 \cdot RA$ is finally the normalized quantity by which we need to multiply the non-dimensional velocities of the row to have the dimensional ones. For instance :

$$\bar{V}_{row} = (\bar{A00} \cdot RA_{row}) \cdot V_{row} . \quad (\text{A.20})$$

The out.Syyy file

Like the first rotor, it is necessary to write the mixed-out quantities at the exit of the stator to run the next row. For the stator,

$$(\bar{a}_{o_{2_{abs}}})_{stator} = (\bar{a}_{o_{1_{abs}}})_{stator} \quad (\text{A.21})$$

Therefore, the RA ratio in the **out.Syyy** file is not changed. The file is written by **iprint_trans_stator.f** and has the following format,

- $r_{2stator}$ (m)
- $\bar{V}_{x1stator} = V_{x1stator} \cdot (\bar{A}00 \cdot RA_{stator})$ (m/s)
- $\bar{V}_{x2stator} = V_{x2stator} \cdot (\bar{A}00 \cdot RA_{stator})$ (m/s)
- $M_{2absstator}$
- $\beta_{2absstator}$ (deg)
- $RA_{stator} = RA_{previous.rotor}$
- $(\bar{a}_{o1abs})_{stator} = (\bar{a}_{o2abs})_{previous.rotor}$ (m/s)
- $(\bar{a}_{o2abs})_{stator} = (\bar{a}_{o1abs})_{stator} \cdot \left(\frac{a_{o2abs}}{a_{o1abs}}\right)_{stator} = (\bar{a}_{o1abs})_{stator}$ (m/s)
- $\bar{A}00$ (m/s)
- $(\bar{P}_{o2abs})_{stator} = PSTRATA_{stator} \cdot (\bar{P}_{o1abs})_{stator}$ (Pa)
- $(\bar{T}_{o2abs})_{stator} = \left(\frac{h_{o2abs}}{h_{o1abs}}\right)_{stator} \cdot (\bar{T}_{o1abs})_{stator}$ (K)
- $(\omega)_{stator}$

A.4.3 From Stator to Rotor

The triangle.f and outrel.xxx Files

The purpose of **triangle.f** is to change the quantities on the mixing plane from absolute to relative frame. This is necessary when writing the inlet conditions for the rotor reading outlet quantities from the previous stator with **out.Sxxx**. **Triangle.f** read **sout.Sxxx** and writes **outrel.Sxxx** and **stream.Ryyy** (see details in Figure A-5). Then, **interblade.f** reads **outrel.Sxxx** to write the inlet conditions of the rotor in the relative frame into **ises.Ryyy** (see Section A.4.1). The quantities that differ between **out.Sxxx** and **outrel.Sxxx** are the flow angle, β , and the Mach number, M . The rest of the file is kept identical, and in particular total pressure and temperature are still expressed in the absolute frame. The relationship between absolute frame and relative frame quantities are :

$$\beta = atan\left(\frac{\Omega r - V_x \cdot \tan\beta_{abs}}{V_x}\right) \quad (A.22)$$

$$M = M_{abs} \cdot \left(\frac{\cos\beta_{abs}}{\cos\beta}\right) \quad (A.23)$$

To set the inlet conditions of the rotor, it is also necessary to set the wheel speed using the *ROTREL* parameter as defined in Section A.3.2. **Triangle.f** calculates $(\bar{a}_{o_1})_{rotor}$ using $(\bar{a}_{o_2_{abs}})_{stator}$ from the **out.Sxxx** file (see Section A.4.2) :

$$(\bar{a}_{o_1})_{rotor} = (\bar{a}_{o_2_{abs}})_{stator} \cdot \left(\sqrt{\frac{1 + \frac{\gamma-1}{2} M^2}{1 + \frac{\gamma-1}{2} M_{abs}^2}} \right). \quad (\text{A.24})$$

Post-processing the Rotor Quantities

Like the stator, all quantities out of MISES are non-dimensional. The **iprint** execution and the **out.xxx** file from the previous stator enables to have access to the exit dimensional pressure and temperature of the rotor in the absolute frame using the ratio $\frac{h_{o_2_{abs}}}{h_{o_1_{abs}}}$ and *PSTRATA*.

For the velocity normalization, $a_{o_{a_{rotor}}} = 1$ by definition. RA_{rotor} is defined as :

$$RA_{rotor} = \frac{(\bar{a}_{o_a})_{rotor}}{\bar{A}00} = \frac{(\bar{a}_{o_a})_{rotor}}{(\bar{a}_{o_a})_{prev.stator}} \cdot \frac{(\bar{a}_{o_a})_{prev.stator}}{\bar{A}00} \quad (\text{A.25})$$

As stated in Equations A.21 and A.17,

$$(\bar{a}_{o_a})_{prev.stator} = (\bar{a}_{o_1_{abs}})_{prev.stator} = (\bar{a}_{o_2_{abs}})_{prev.stator}, \quad (\text{A.26})$$

and by definition of $RA_{prev.stator}$, it is possible to write

$$RA_{rotor} = \frac{(\bar{a}_{o_a})_{rotor}}{(\bar{a}_{o_2_{abs}})_{prev.stator}} \cdot RA_{prev.stator}. \quad (\text{A.27})$$

On the mixing plane,

$$(X_{1_{abs}})_{rotor} = (X_{2_{abs}})_{previous.stator} \quad \text{with } X = M, V_x, \beta, \bar{P}_o \text{ or } \bar{T}_o, \quad (\text{A.28})$$

then ,

$$RA_{rotor} = \frac{(\bar{a}_{o_a})_{rotor}}{(\bar{a}_{o_1_{abs}})_{rotor}} \cdot RA_{prev.stator} = \frac{(a_{o_a})_{rotor}}{(a_{o_1_{abs}})_{rotor}} \cdot RA_{prev.stat} \quad (\text{A.29})$$

and finally,

$$RA_{rotor} = \frac{RA_{prev.stat}}{(a_{o_1_{abs}})_{rotor}}. \quad (\text{A.30})$$

Thus, the **out.Rxx** file written by **iprint_trans_rotor.f** has the following format :

- $r_{2_{rotor}}$ (m)
- $\bar{V}_{x_{1_{rotor}}} = V_{x_{1_{rotor}}} \cdot (\bar{A}00 \cdot RA_{rotor})$ (m/s)
- $\bar{V}_{x_{2_{rotor}}} = V_{x_{2_{rotor}}} \cdot (\bar{A}00 \cdot RA_{rotor})$ (m/s)
- $M_{2_{abs_{rotor}}}$
- $\beta_{2_{abs_{rotor}}}$ (deg)
- $RA_{next.stator} = RA_{rotor} \cdot (a_{o2_{abs}})_{rotor}$
- $(\bar{a}_{o1_{abs}})_{rotor} = (\bar{a}_{o2_{abs}})_{previous.stator}$ (m/s)
- $(\bar{a}_{o2_{abs}})_{rotor} = (\bar{a}_{o1_{abs}})_{rotor} \cdot \left(\frac{a_{o2_{abs}}}{a_{o1_{abs}}}\right)_{rotor}$ (m/s)
- $\bar{A}00$ (m/s)
- $(\bar{P}_{o2_{abs}})_{rotor} = PSTRATA_{rotor} \cdot (\bar{P}_{o1_{abs}})_{rotor}$ (Pa)
- $(\bar{T}_{o2_{abs}})_{rotor} = \left(\frac{h_{o2_{abs}}}{h_{o1_{abs}}}\right)_{rotor} \cdot (\bar{T}_{o1_{abs}})_{rotor}$ (K)
- $(\omega)_{rotor}$

It is important to notice that the RA stored in the outlet rotor file **out.Rxx** is the $RA_{next.stator}$. This is only a programming matter which is linked to the storage of the quantity $(a_{o2_{abs}})_{rotor}$. In particular, this enable to use the same programs for the next stages i.e. the next stator will use the same process as described in Section A.4.2.

The whole process described in the last two sections is summarized by the flowchart fig.A-3 p.106.

A.5 Detailed First Row Process for Running MISES on Compressor

In this Appendix are presented the processes for running MISES on the CREATE Compressor. The processes are described using flowcharts in order to give the reader a global understanding as well as the logical links between the different programs. Figure A-4 develops the process of generating the geometry of the compressor from the 3D data from SNECMA to files readable by MISES. Figure A-5 described in detail how one stage is run from the rotor absolute inlet conditions to the postprocess at the exit of the stator.

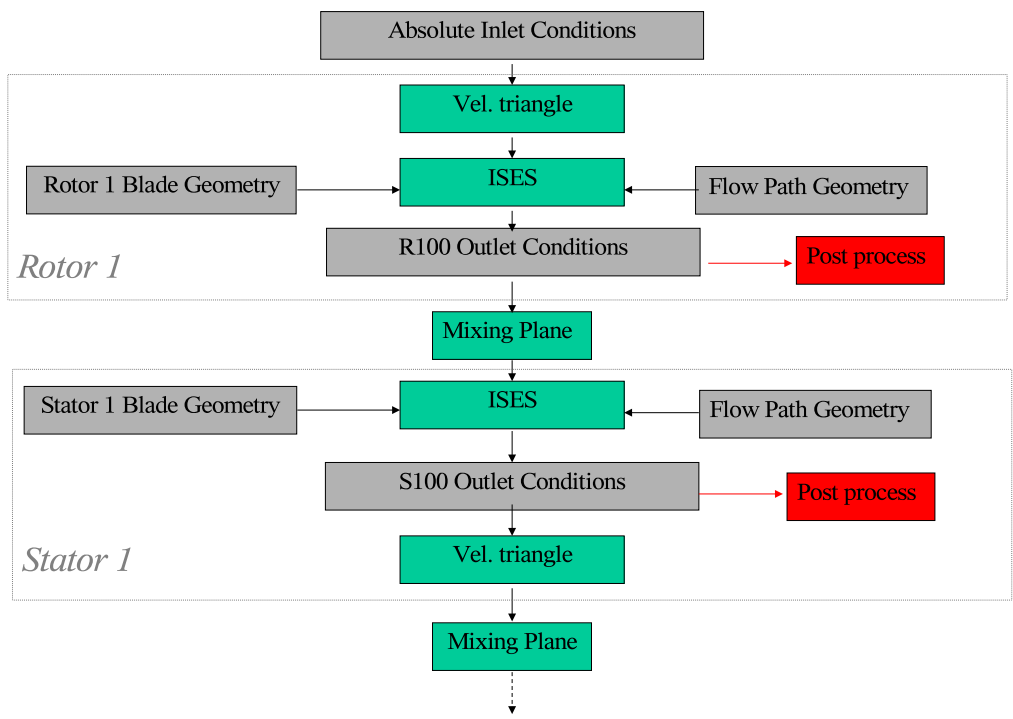


Figure A-3: Flowchart : First Stage Process

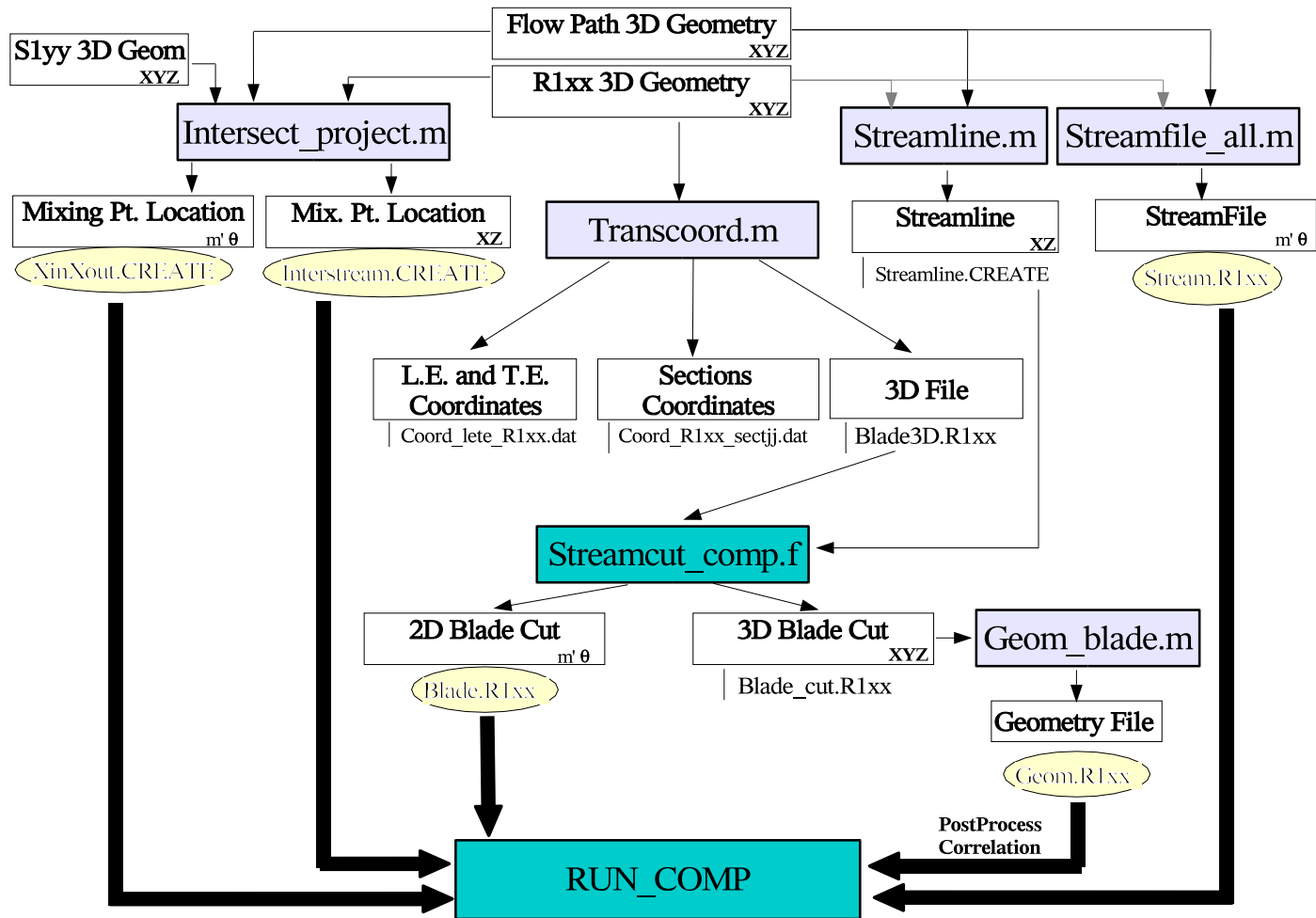


Figure A-4: Flowchart : Detailed First Row Geometry File Generation Process

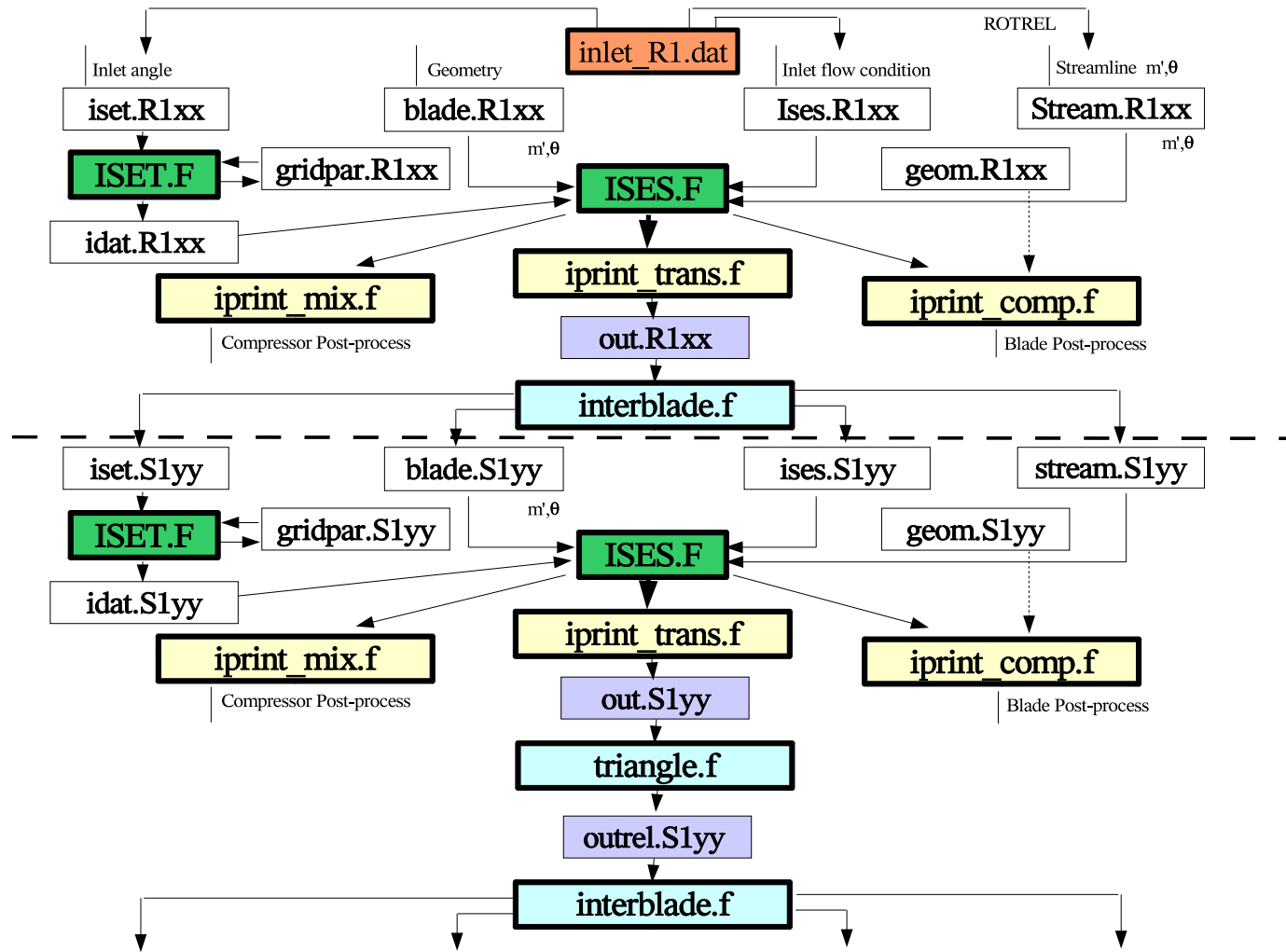


Figure A-5: Flowchart : Detailed First Row Process

A.6 Running the run_comp Interface

Certain rules have to be followed to be able to run the script **run_comp.sh**. First of all, all Fortran executable files and the **run_comp.sh** script must have a link in the /bin directory to enable the user to launch them from any directory.

With a compressor COMP and blade rows named ROTOR1,STATOR1..., the script has to be run in the directory COMP where the files **inlet_R1.dat**, **XinXout.COMP** and **inter-stream.COMP** are. The COMP directory must also contains 6 directories ROTOR1...STATOR3. Each of these 6 directory contains all the files necessary to run MISES locally : **ises.xxx**, **stream.xxx**, **blade.xxx**... The extension of the file must be the same as the directory name.

Some files are created for post-processing. In particular **mix.COMP** gives the *absolute-frame* dimensional quantities on the mixing planes. The **results.Stageii** file gives the local non-dimensional flow quantities concerning the stage *ii* : for instance inlet and outlet Mach and flow angles, pressure and enthalpy ratios...

Figure A-6 details the directories and file location. The files in black are necessary to run the script and the ones in light gray are created by MISES. The **out.xxx** and **outrel.xxx** files are created by MISES and are necessary for the run of the next row:

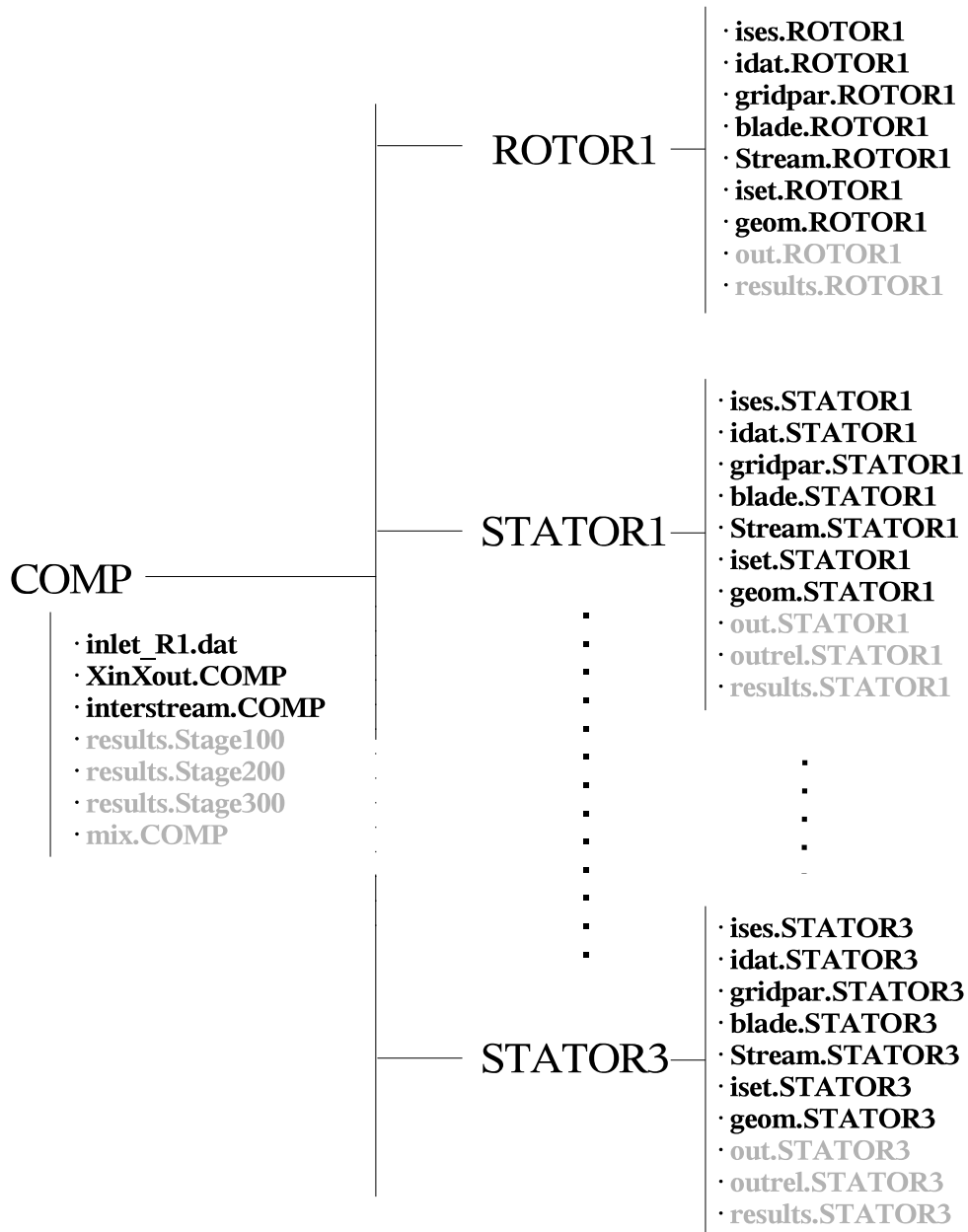


Figure A-6: Directory and Files Tree Pattern

Appendix B

The GE Correlations

B.1 The C_h at stall

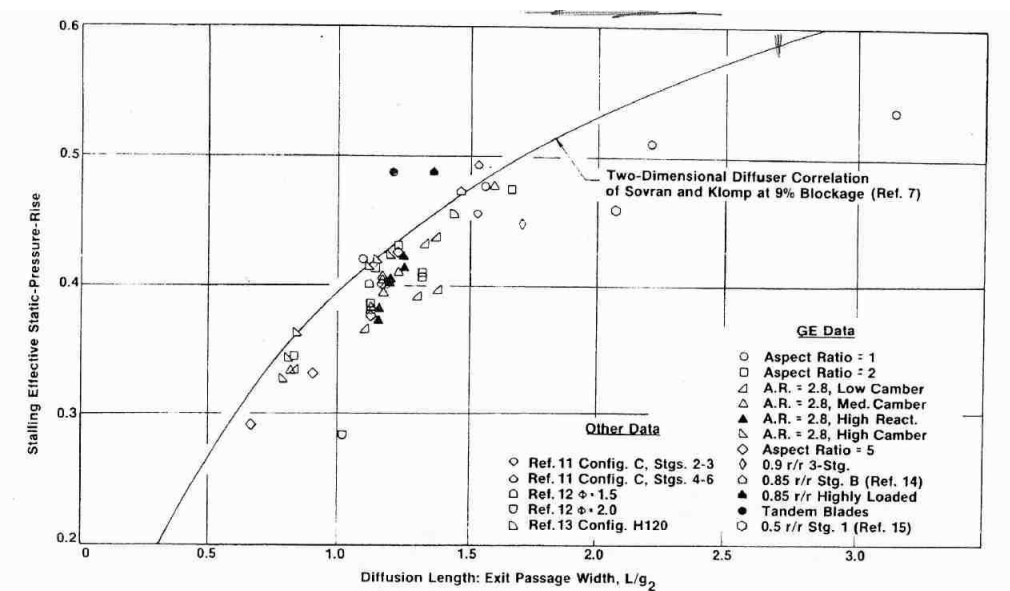


Figure B-1: Correlation of stalling effective static-pressure-rise coefficients

B.2 The Displacement Thickness Correlation

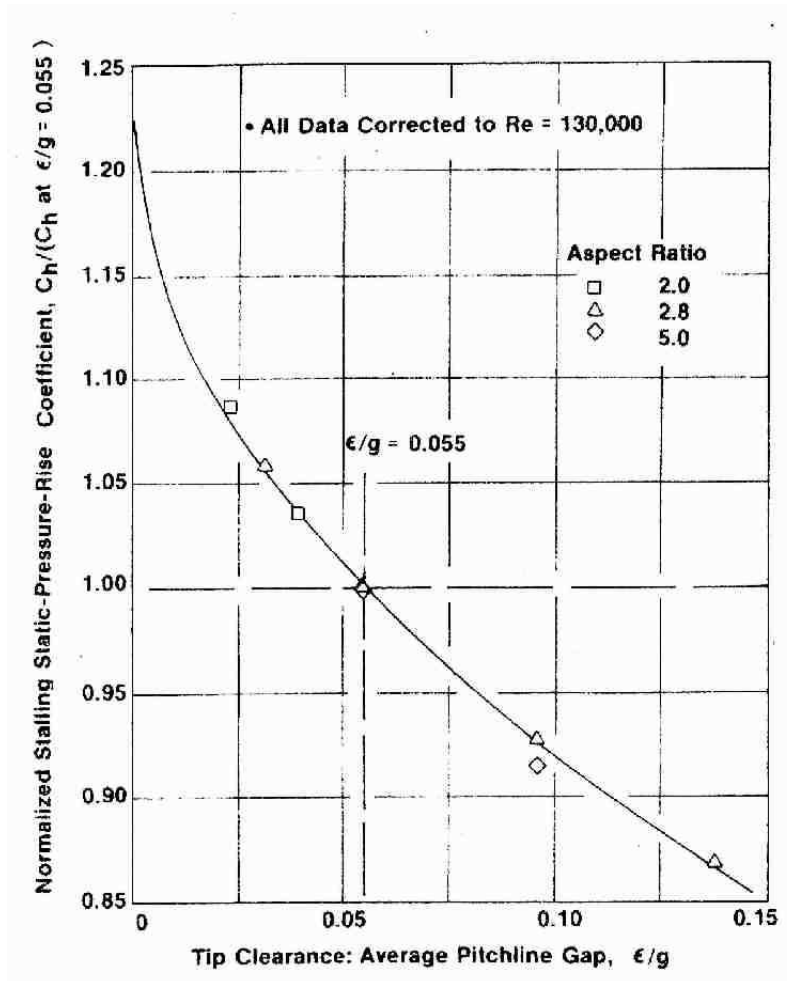


Figure B-2: Effect of tip clearance on stalling pressure rise coefficient

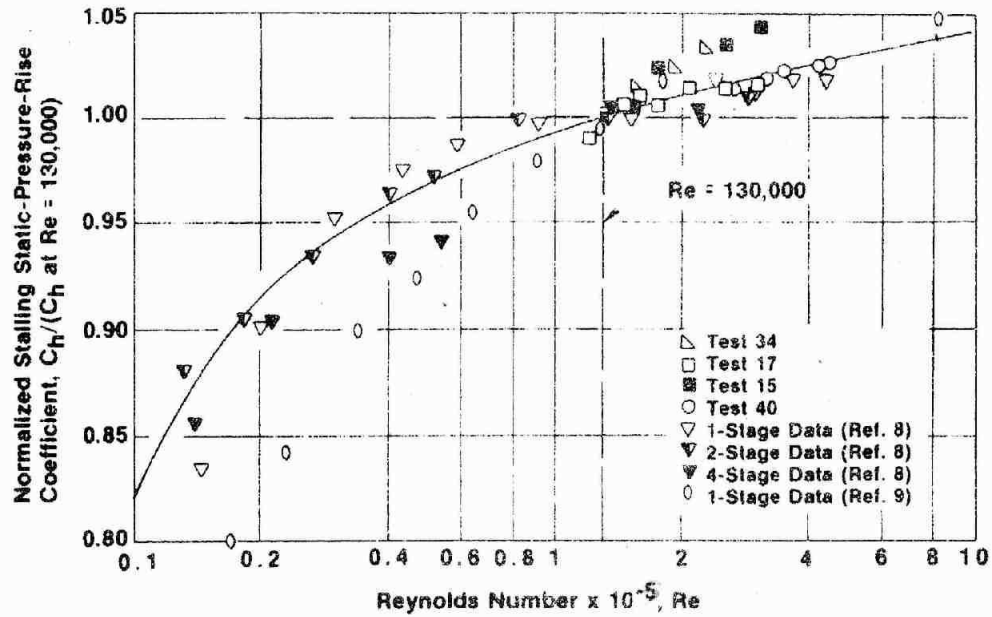


Figure B-3: Effect of Reynolds number on stalling pressure rise coefficient

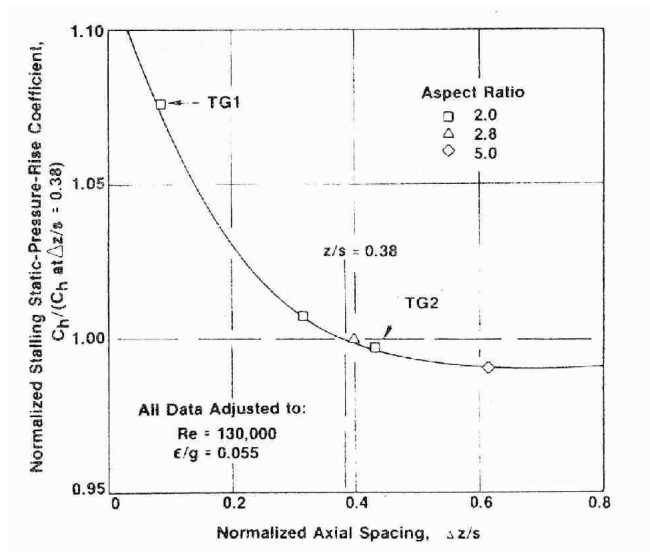


Figure B-4: Effect of axial spacing on stalling pressure rise coefficient

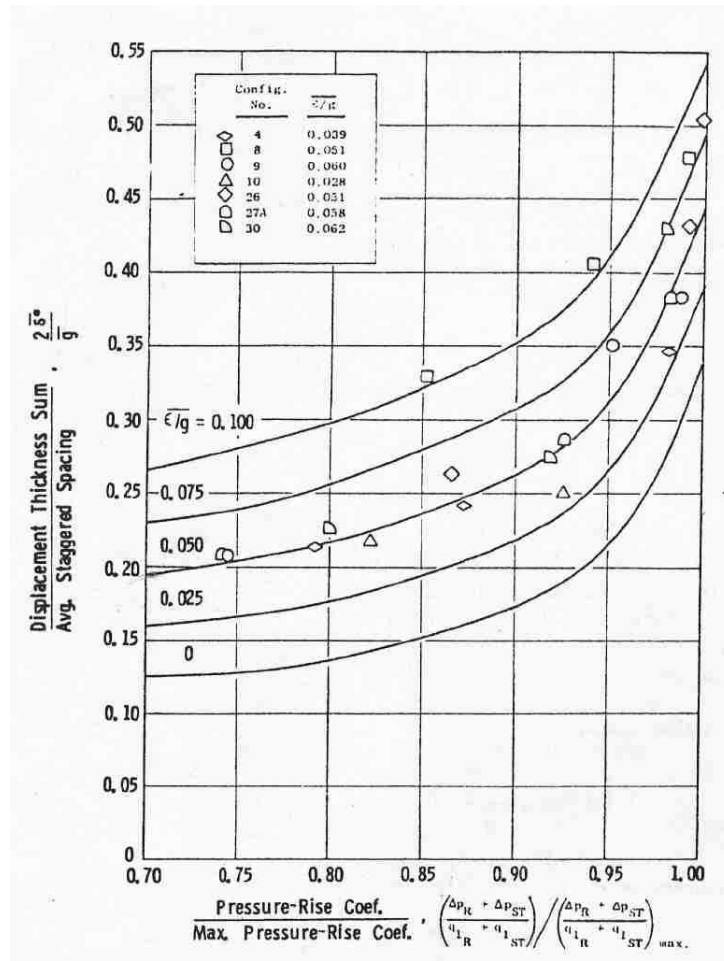


Figure B-5: Sum of hub and tip endwall axial velocity displacement thickness, from [10]

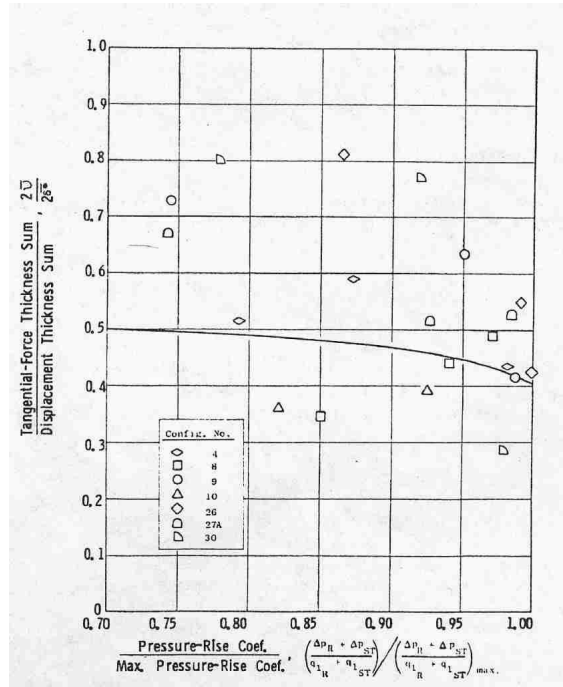


Figure B-6: Sum of hub and tip endwall tangential-force thickness, from [10]

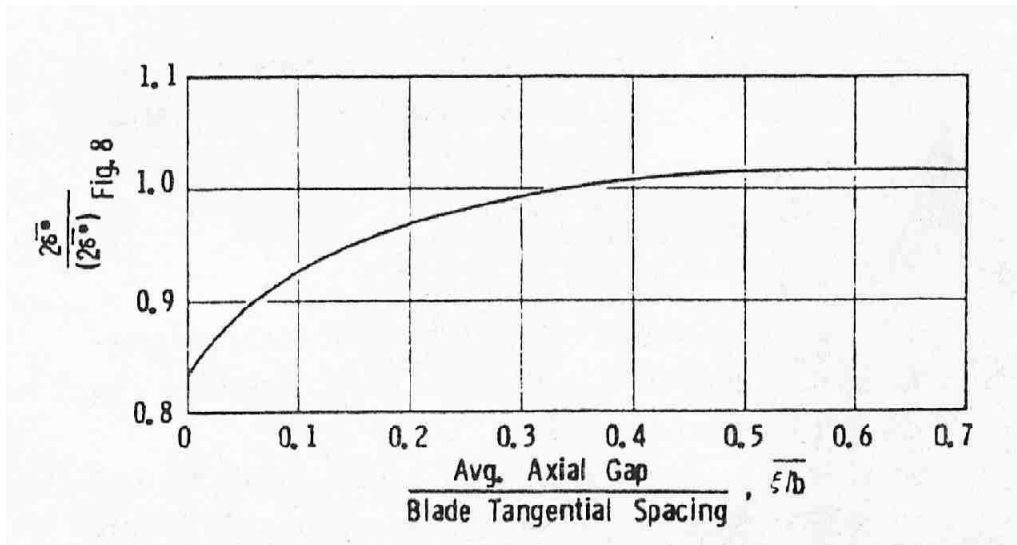


Figure B-7: Effect of axial spacing on endwall displacement thickness, from [10]

Appendix C

Implementation of the Correlations with Mises

The script to run the whole process is a MATLAB script named **run_stage3**. This script calls different programs using MATLAB and FORTRAN77. For the freestream run, the FORTRAN77 script **run_comp** is used. It is presented in Appendix A but was slightly modified to take inlet conditions at the inlet of the third stage. The calculation of displacement thicknesses and changes of the **stream.xxx** file with the new AVDR is done by a MATLAB code called **ite_AVDR.m**. Finally, the FORTRAN77 program **Corel_stage3** calculated the $\frac{Ch}{Ch_{max}}$ from the GE correlations as well as the actual final quantities (efficiency, absolute total pressure rise...).

The issue is that the AVDR is a function of the $\frac{Ch}{Ch_{max}}$ and that $\frac{Ch}{Ch_{max}}$ is also a function of the AVDR since the pressure rise of the freestream flow changes with AVDR (see Section 3.3.3). It is then necessary to make iterations. The flowchart on Figure C-1 details the process for a single run. Taking the inlet conditions to the third stage, first freestream flow calculation is run with no displacement thickness in order to have a rotor static pressure ratio. From this first run, and starting the iteration with $\frac{Ch}{Ch_{max}} = 1$, displacement thicknesses are calculated at the exit and at the mixing plane between rotor and stator. From this δ^* calculation, it is possible to run the freestream calculation with the new AVDR and get the Ch and rotor static pressure rise. Ch_{max} is then calculated, and from $\frac{Ch}{Ch_{max}}$ we can obtain the actual efficiency and absolute total pressure rise. The iteration "0" is then finished.

Then there is an iteration process using the convergence of $\frac{Ch}{Ch_{max}}$ as criteria. Starting from the

$\frac{Ch}{Ch_{max}}$ and ΔP_{rotor} of iteration "0", the new AVDR is calculated, a freestream calculation run, the new $\frac{Ch}{Ch_{max}}$ calculated and compared to the first one. this loop is done as long as the two $\frac{Ch}{Ch_{max}}$ are different. Finally, once the iteration process has converged, the actual exit conditions of the stage with the end-walls blockage and losses are known. Figure C-1 details the process.

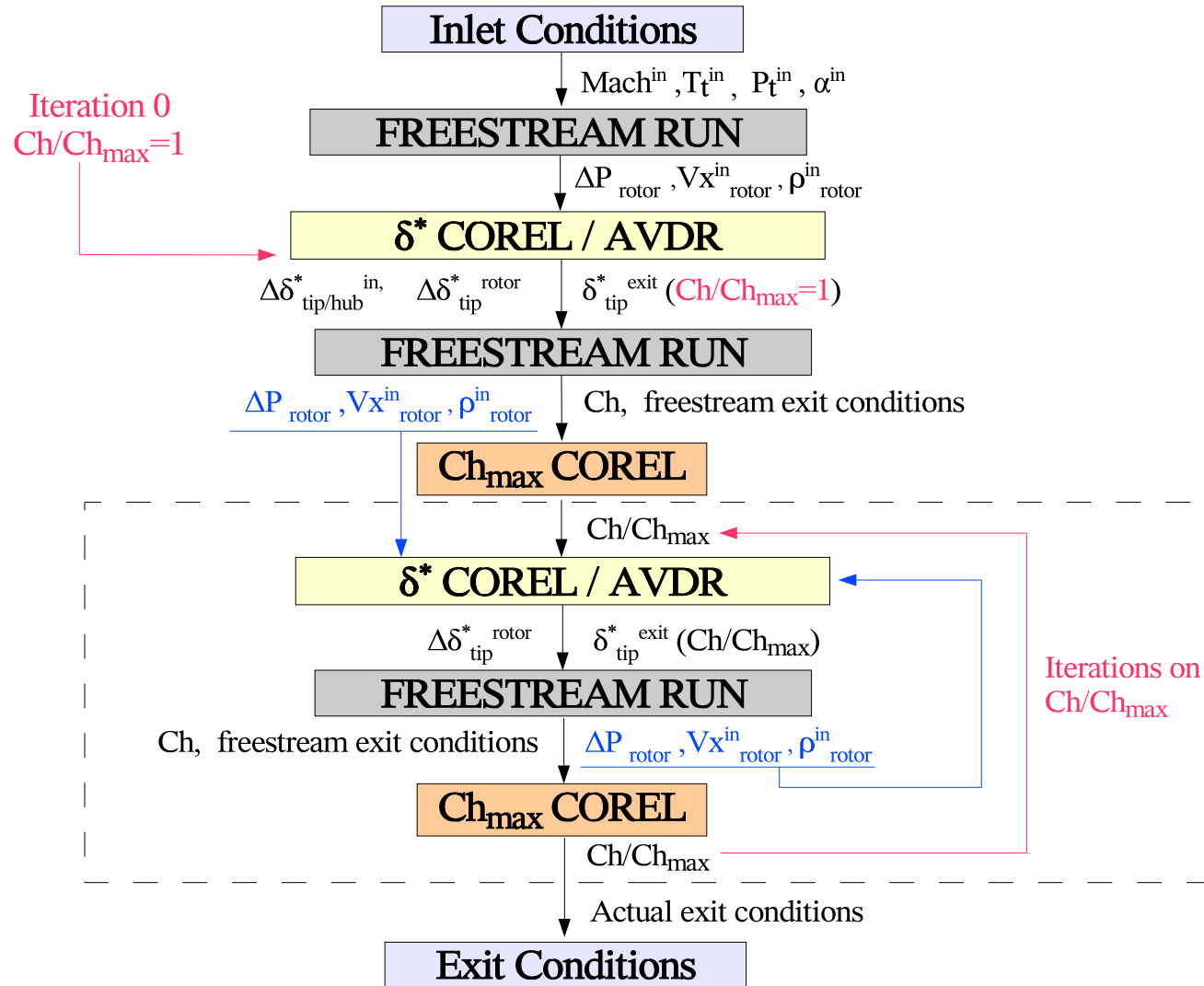


Figure C-1: Flowchart : Detailed Process of a Single Meanline Run using Correlations and Mises

Appendix D

How To Run NUMECA Fine Turbo on CREATE Compressor

D.1 Introduction

This appendix presents the methodology for running the 3D code. In fact, this NUMECA code was first used at MIT for this particular research, and it may be important for future use to present how I used it and how certain issues were solved. Some of them may be generic to all 3D codes and some of them more particular to the use of this code.

D.2 The meshing of the grid using IGG/Autogrid

D.2.1 The first cell distance to wall y_{wall}

A particular attention must be observed when meshing the grid close to the walls since the turbulence model chosen depends a lot on the distance of the first cell to the wall. When calculating turbulence quantities, it is important to place the first grid node off the wall within a certain range y_{wall} [20]. For this reason, it is necessary to calculate the relation between this distance and a local Reynolds number based on wall variables at the first node called Y_1^+ .

$$Y_1^+ = \frac{\rho \cdot u_\tau \cdot y_{wall}}{\mu} \tag{D.1}$$

where u_τ is the friction velocity.

$$u_\tau = \sqrt{\frac{\tau_{wall}}{\rho}} = \sqrt{\frac{1}{2} V_{ref}^2 C_f} \quad (D.2)$$

Two methods were used to approximate Y_1^+ . In both methods, the reference velocity V_{ref} was taken from an average axial velocity at the inlet and the reference length L_{ref} was based on a streamwise distance which in our case was the distance between the inlet plane and the first rotor leading edge. In our case, $V_{ref} \simeq 150\text{m/s}$, $L_{ref} \simeq 0.048\text{m}$ and $\nu = 1.466 \times 10^{-5} \text{m}^2/\text{s}$.

The first method to approximate y_{wall} is to apply the $1/7^{th}$ profile where the friction C_f for a flat plate is related to the Reynolds number:

$$C_f = \frac{0.027}{Re_x^{\frac{1}{7}}} \quad (D.3)$$

Using this method, the relation found was :

$$y_{wall_1} \simeq 2 \times 10^{-6} \cdot Y_1^+ \quad (D.4)$$

The second method is based on a truncated series solution of the Blasius equation :

$$y_{wall} = 6 \left(\frac{V_{ref}}{\nu} \right)^{-\frac{7}{8}} \left(\frac{L_{ref}}{2} \right)^{\frac{1}{8}} \dots \quad (D.5)$$

It appears that the relation found using this method give the same result than in equation D.4.

The value given to Y_1^+ depends on which turbulence model is wanted. A y_{wall} study has been conducted with the Baldwin-Lomax turbulence model setting Y_1^+ to 1,10 and 30. The criteria of selection was convergence of the code, speed of convergence, and the resolution of the flow in the clearance region. The grid setting y_{wall} with a Y_1^+ of 1 was giving the best results considering the criteria. In addition, the compressor map obtained with this y_{wall} appeared to be close to the SNECMA compressor map for the CREATE compressor (see fig.2-2 p.30). The k-epsilon turbulence model with an extended wall function was tested on one case but the computational additional costs and the reduced stability of the computation were such that it was decided to run the sensitivity analysis using the Baldwin-Lomax turbulence model.

In conclusion, the distance of the first cell was finally set to $y_{wall} = 2 \times 10^{-3} \text{mm}$ ($Y_1^+ = 1$) and

Balwin-Lomax turbulence model was chosen.

D.2.2 The tip clearance grid

For the nominal geometry that had a 0.5mm of tip/hub clearance, the number of points was always set to 17 in the spanwise direction and 13 in the azimuthal direction. It was decided to have a clustered mesh -in opposition to uniform- in order to keep the constraint of the first cell distance to the wall.

When the clearance was doubled to 1mm, the number of points in the spanwise direction in the clearance grid was brought to 21. The number of points in the clearance was not doubled because the total number of points of the whole passage would have been 30% higher and the computation would have been much more costly (the number of spanwise points for the whole passage was about 60 for each row). However, as the no-clearance region number of spanwise points is the difference between of the whole passage number of spanwise points and the clearance region number of spanwise points, 4 points were added to the total passage number of points in order to to keep the same grid in the no-clearance region, this, as an attempt to have results less grid dependent.

When the clearance was divided by two to 0.25mm, the number of points in the spanwise direction in the clearance grid was brought to 9. In this case, the whole passage number of spanwise points was reduced by 8 points for the same purpose that presented above.

Bibliography

- [1] C.C. Chamis. Probabilistic structural analysis methods for space propulsion system components. *Probabilistic Engineering Mechanics*, Vol. 2, No. 2, pp. 100-110, 1987.
- [2] A.J. Crook, E.M. Greitzer, C.S. Tan, J.J. Adamczyk. Numerical Simulation of Compressor Endwall and Casing Treatment Flow Phenomena, *ASME J. Turbomachinery*, Vol. 115, No. 3, pp. 501-512, July 1993.
- [3] N.A. Cumpsty. Annulus Wall Boundary-Layers Measurements in a Four-Stage Compressor. *ASME J. of Engineering Gas Turbine Power*, Vol. 108, pp. 2-6, October 1986.
- [4] M. Drela and H. Youngren. *A User's Guide to MISES 2.53*. MIT Fluid Dynamics Research Laboratory, 70 Vassar ST, Cambridge MA 02139, December 1998.
- [5] V.E. Garzon. *Probabilistic Aerothermal Design of Compressor Airfoils*. PhD Thesis, Massachusetts Institute of Technology, February 2003.
- [6] E.M. Greitzer and D.C. Wisler. Gas Turbine Compressor Technology: Status and Opportunities. Keynote Lecture at International Gas Turbine Congress, Kobe Japan, 1999.
- [7] J.H. Horlock and H.J. Perkins. Annulus Wall Boundary Layers in Turbomachines. *AGARDograph*, AG-185, 1974.
- [8] J.H. Horlock. The Determination of End-Wall Blockage in Axial Compressors : A Comparison Between Various Approaches. *ASME Journal of Engineering for Power*, Vol. 122, pp. 218-224, April 2000.

- [9] M.A. Howard, P.C. Ivey, J.P. Barton, and K.F. Young. Endwall Effects at Two Tip Clearances in a Multistage Axial-Flow Compressor With Controlled Diffusion Blading. *ASME J. of Turbomachinery*, Vol. 106, pp. 635-647, 1994.
- [10] C.C. Koch and L.H. Smith Jr. Loss Sources and Magnitudes in Axial Flow Compressors. *ASME J. of Engineering for Power*, Vol. 98, No. 3, July 1976.
- [11] C.C. Koch. Stalling Pressure Rise Capability of Axial Flow Compressor Stages. *ASME J. of Engineering for Power*, Vol. 103, October 1981.
- [12] C. Lykins, D.E. Thompson and C. Pomfret. The Air Force's Application of Probabilistics to Gas Turbine Engines. AIAA-94-1440-CP, AIAA, 1994.
- [13] R.H. Myers and D.C Montgomery. *Response Surface Methodology. Process and Product Optimization Using Designed Experiments*. Wiley Series In Probability and Statistics, 1995.
- [14] R.S. Ryan and J. S. Townsend. Application of probabilistic analysis/design methods in space programs : the approaches, the status, and the needs. AIAA-93-1381, 1993.
- [15] L.H. Smith Jr. Casing Boundary Layers in Multistage Axial-Flow Compressors. *Flow Research on Blading*, ed., L.S Dzung, Elsevier Publishing, Amsterdam, Netherlands, 1970.
- [16] F.M. White. *Viscous Fluid Flow*. Second Edition, McGraw-Hill, pp. 28-29, 1991.
- [17] D.E. Thompson and T.G. Fecke. Air Force perspective on probabilistic design. *Reliability Technology*, Vol. 28, 1992.
- [18] H. Youngren. Analysis and Design of Transonic Cascades with Splitter Vanes. MIT GTL Report#203, March 1991.
- [19] Fine User Manual. Version 5.2, NUMECA International, June 2001.
- [20] *How To ?... generate grids for turbulent flows*. Quick reference Card 1st edition, NUMECA International, June 15th 2001.